Development of a Green Parabolic Trough Collector

Sunvapor, Inc

Philip Gleckman and Nicolas R. Peralta

October 21, 2018

This page intentionally left blank

ABSTRACT

This report describes in detail a research project that assesses the potential of a parabolic trough solar collector with a lumber construction to meet ambitious performance, cost, and durability goals. Instead of exploring lumber as a general question for solar collectors, the project focuses on the design optimization, laboratory testing, outdoor testing, and economic modeling of a particular scale of parabolic trough, namely, the 6m aperture and 12m long module that has become the standard in the utility-scale power plant market. As will be appreciated in the report, it is also a scale that matches well the capabilities of lumber as a structural material and the commonly available cross sections. The design and its analysis extend far beyond traditional considerations for wooden structures in the built environment, and includes a computationally efficient coupled structural-optical simulation and the empirical characterization of joint stiffness at small deformations. Laboratory testing is used to characterize cyclic joint behavior, accelerated weathering, and to validate the simulation used as the basis for building a full-scale prototype. The construction and outdoor testing of this prototype is described. A total installed cost model of the collector is presented and the impact of the cost is seen in the context of a full plant techno-economic model. The results of this model in combination with the experience with the first prototype suggest that with improvements to the design and assembly process, this collector type has the potential to lower the levelized cost of heat for industrial solar steam plants used for process heating or cogeneration.

This page intentionally left blank

ACKNOWLEDGMENTS

This material is based upon work supported by the U.S. Department of Energy under Award Number DE-EE0007343

This page intentionally left blank

CONTENTS

ABSTRACT **3**

ACKNOWLEDGMENTS **5**

CONTENTS **7**

LIST OF TABLES **11**

LIST OF FIGURES **13**

1 EXECUTIVE SUMMARY **19**

1.1 Introduction **19**

1.2 Purpose **19**

1.3 Project objectives **19**

1.4 Project outcomes **20**

1.5 Project milestones **20**

1.6 Conclusions and recommendations **21**

2 INTRODUCTION **23**

2.1 Background **23**

2.2 Project objectives **24**

3 PROJECT OUTCOMES **25**

3.1 Economics **25**

3.1.1 Annual energy yield 25

3.1.2 Total installed collector cost model 26

3.1.3 Complete plant CAPEX model 27

3.1.4 Financial model 27

3.2 Collector Engineering **31**

3.2.1 Engineering analysis prior component testing 31

3.2.2 Test specification 33

3.2.3 Fatigue test results 38
3.2.4 Accelerated weathering 42
3.2.5 Optimization 44
3.2.6 Simulation of aged structure 48
3.2.7 Full-scale module prototype design 49
3.3 Laboratory model validation 54
3.3.1 Design requirements of the validation prototype 54
3.4 Collector assembly and construction 68
3.4.1 Component fabrication and painting 68
3.4.2 Civil and electrical work prior to collector assembly and installation 69
3.4.3 Collector spaceframe assembly 72
3.4.4 Collector spaceframe assembly time and motion studies 73
3.4.5 Support pylons assembly and installation 74
3.4.6 End plate attachment 74
3.4.7 Receiver mount alignment 75
3.4.8 Bracket attachment and mirror installation 76
3.4.9 Collector lifting 77
3.4.10 Collector tracking control system 79
3.4.11 Collector rotation test 80
3.5 Outdoor testing 81
3.5.1 Slope error 81
3.5.2 Intercept factor 83
3.5.3 Torsional stiffness assessment 93
3.6 Structure Health, Maintenance and repairs 111
3.6.1 End plates insufficient out-of-plane stiffness 111
3.6.2 Receiver mount deformation 113
3.6.3 Insufficiency of special detail for out-of-plane load bridging between torque resisting components 114
3.6.4 Time evolving gap on wood to wood assembly joints 116
3.6.5 Comments on structure health 117

4 PROJECT MILESTONES 119

5 CONCLUSIONS AND RECOMMENDATIONS.....123

REFERENCES.....125

This page intentionally left blank

LIST OF TABLES

Table 3-1 Plant design parameters 25

Table 3-2 Collector cost model 26

Table 3-3 Assumptions for IRR model 28

Table 3-4 Wind force cycles for Las Vegas site 32

Table 3-5. Comparison between preliminary and optimized design. Performance computed for worst case operating wind condition 48

Table 3-6. Loading configurations 62

Table 3-7. Slope error results 82

Table 3-8. Simulated Intercept for an array in worst case wind based on measured torsional stiffness 108

Table 4-1 First phase milestones 120

Table 4-2 Second phase milestones.....121

This page intentionally left blank

LIST OF FIGURES

Figure 3-1. Historical lumber price 29

Figure 3-2. Total installed collector cost frequency distribution (40,000 samples) 29

Figure 3-3. Composite NSRDB records for Las Vegas....30

Figure 3-4. IRR frequency distribution from a sample size of 1000 30

Figure 3-5. Wind speed frequencies for Las Vegas (2000-2016) [9] 32

Figure 3-6. Load history for diurnal gravity and wind forces 33

Figure 3-7. Photo and overall schematic of tensile testing machine with dimensions in inches. 34

Figure 3-8. DAQ UI showing example test data. 35

Figure 3-9. Test setup for fatigue and initial stiffness testing 36

Figure 3-10. Schematic representation of a force-vs-deformation relationship. Sub-indices “i” and “f” stand for initial and final respectively. 37

Figure 3-11. Force-vs-deformation relationship for 4 truss joints subjected to 3600 cycles....38

Figure 3-12. Evolution of truss joint stiffness when subjected to 3600 cycles 38

Figure 3-13. Photograph of diagonal member to truss joints using steel brackets 39

Figure 3-14. Force-vs-deformation relationship for a tie plate joint subjected to 3600 cycles....39

Figure 3-15. Evolution of stiffness of the tie plate joint....40

Figure 3-16. Diagonal members joined to trusses using wood to wood screws....40

Figure 3-17. Test setup for wood to wood joints....40

Figure 3-18. Force-vs-deformation relationship for a wood to wood joint 41

Figure 3-19. Evolution of truss joint stiffness of the wood to wood joint....41

Figure 3-20. Evolution of specimens weight (in grams) over time 42

Figure 3-21. Unfinished specimen....43

Figure 3-22. Truss connector plates with LATEX paint....43

Figure 3-23. Unfinished TimberLOK joints 44

Figure 3-24. TimberLOK joints with 2 coats of LATEX paint....44

Figure 3-20. Projected sunshape with circumsolar ratio of 5.0%....45

Figure 3-21. Incidence angle modifier....45
Figure 3-22. Structural model automatic generation....46
Figure 3-23. Structural design geometric cases....46
Figure 3-24. Structural design exploration....47
Figure 3-25. Monte Carlo simulation of aged structure....49
Figure 3-26. Isometric view [top], posterior view (from convex side) [left] and lateral view [right]....50
Figure 3-27. Pylon trusses design....50
Figure 3-28. Isometric view of drive pylon [left] and slew drive [right]....51
Figure 3-29. Splay resisting component....51
Figure 3-30. Joint "J2"....52
Figure 3-31. Joint "J4" [13]....52
Figure 3-32. Torsion resisting component....52
Figure 3-33. 3D representation of Joint "J4"....52
Figure 3-34. Details of joints of torsion resisting components and splay resisting components....53
Figure 3-35. Exterior mirror support sub-assembly....53
Figure 3-36. Interior mirror support sub-assembly....54
Figure 3-37. Position of mirror brackets....54
Figure 3-38. Validation prototype....55
Figure 3-39. Lateral view....55
Figure 3-40. Top view....56
Figure 3-41. Torque resisting elements....56
Figure 3-42. Available height and specimen's dimensions....56
Figure 3-43. Estimation of loading magnitude for 4mrad displacements....57
Figure 3-44. Location of loading points....57
Figure 3-45. Specimen support....60
Figure 3-46. Torque plate....60
Figure 3-47. Hardware for loading....60
Figure 3-48. Load measurement....60
Figure 3-49. Turn buckle for load application....60

Figure 3-50. Laser tracker....61
Figure 3-51. Retro-reflector....61
Figure 3-52. Three spheres (triads) making a kinematic mount for retro-reflector....61
Figure 3-53. Position measurements....61
Figure 3-54. Mirror slope measurement....62
Figure 3-55. “snake path”....62
Figure 3-56. Exagerated deformed shape from triad measurements....63
Figure 3-57. Slope error for interior segment relative to “ideal parabola” for load configuration B1....64
Figure 3-58. Slope error for exterior segment relative to “ideal parabola” for load configuration B1....64
Figure 3-59. Slope error for interior segment relative to “ideal parabola” for load configuration B2....65
Figure 3-60. Slope error for exterior segment relative to “ideal parabola” for load configuration B2....65
Figure 3-61. Exagerated deformed shape from structural modeling with parameters updated from triads information....66
Figure 3-62. Slope error prediction for configuration B1. Comparison between original model with uncertain parameters and revised model with measured parameters.....67
Figure 3-63. Slope error prediction for configuration B2. Comparison between original model with uncertain parameters and revised model with measured parameters.....67
Figure 3-64. Spaceframe parts....68
Figure 3-65. Spaceframe components prior to painting....69
Figure 3-66. Painted components....69
Figure 3-67. Permit header....70
Figure 3-68. Site preparation....70
Figure 3-69. Electrical layout....71
Figure 3-70. Electrical work....71
Figure 3-71. Concrete pad for pylons....72
Figure 3-72. Spaceframe assembly steps....73
Figure 3-73. Pylons assembly steps....74

Figure 3-74. End plate assembly 75
Figure 3-75. End plate on spaceframe 75
Figure 3-76. Receiver mount 75
Figure 3-77. Receiver mount alignment steps 76
Figure 3-80. Mirror installation 76
Figure 3-81. Structural idealization of lifting bar 77
Figure 3-82. Bending moment diagram for the bar 77
Figure 3-83. Axial load and bending moment interaction check 78
Figure 3-84. Collector lifting process 78
Figure 3-85. Lifting complete 79
Figure 3-86. Human-Machine Interface 79
Figure 3-87. Main Control Panel 79
Figure 3-88. Drive system 80
Figure 3-90. Collector first rotation test 80
Figure 3-90. Schematics of raytracing problem 81
Figure 3-91. Orientation of image plane of 20.653o 82
Figure 3-92. Insulated piping and flexible hose connected to collector 83
Figure 3-93. Thermal performance (June 1, 2018) 84
Figure 3-94. Efficiency (June 1, 2018) 84
Figure 3-95. Thermal performance (June 7, 2018) 85
Figure 3-96. Efficiency (June 7, 2018) 85
Figure 3-97. Receiver mount misalignment 86
Figure 3-98. Receiver deformed shape when subjected to constant temperature gradient. 86
Figure 3-99. Receiver profile 86
Figure 3-100. Reference system 86
Figure 3-101. Intercept factor as a function of receiver position. 87
Figure 3-102. Varying the collector inlet temperature on May 24, 2018 89
Figure 3-103. Raw difference in RTD readings 89
Figure 3-104. Glass temperature reading 90

Figure 3-105. Middle and east targets, with profile....91
Figure 3-106. Pictures of targets: From upper left, clockwise West, Middle, East from North, East from South....92
Figure 3-107. Profile data from pictures....93
Figure 3-108. Location of Torque tube and definition of reference system....94
Figure 3-109. Strain gauge installation....94
Figure 3-110. Local orientation of sensors within rosette....94
Figure 3-111. Strain contours due to the application of axial load (P) of 1kN....95
Figure 3-112. Strain contours due to the application of a shear force of 1kN in X-X direction....96
Figure 3-113. Strain contours due to the application of a shear force of 1kN in Y-Y direction....97
Figure 3-114. Strain contours due to the application of a moment of 1kNm about X-X axis....98
Figure 3-115. Strain contours due to the application of a moment of 1kNm about Y-Y axis....99
Figure 3-116. Strain contours due to the application of a moment of 1kNm about Z-Z axis....100
Figure 3-117. Schematics of strain sensors within a rectangular rosette....102
Figure 3-118. Torsional behavior of a collector array....104
Figure 3-119. Twist time history....106
Figure 3-120. Strain Gauges time history....106
Figure 3-121. Torque time history....106
Figure 3-122. Torque vs Twist....106
Figure 3-123. Torsional behavior of a collector array subjected to maximum torque....107
Figure 3-124. Intercept factor vs tracking error....108
Figure 3-125. Worst case Intercept factor vs wind speed....108
Figure 3-126. Three-month history of collector twist....109
Figure 3-127. Three-month history of 5-mins mean wind speed....110
Figure 3-128. Wind speed time history....110
Figure 3-129. Time history of twisting adjusted for SCA. (i.e. measured scaled with a factor of 36)....111

Figure 3-135. Exagerated deformed shape showing the effect of insufficient out-of-plane stiffness of the ends of spaceframe. 112
Figure 3-136. Eccentricity of bearing with respect to the spaceframe. 112
Figure 3-137. Hollow structural sections attached to end plates to provide additional out-of-plane stiffness. 112
Figure 3-138. Possible candidates causing receiver to zag....113
Figure 3-139. Stiffening of lower receiver mount 114
Figure 3-140. Forces acting out of the plane of SRC members (Figure 3-33) 115
Figure 3-141. Effect of forces leading to out-of-plane failure mode....115
Figure 3-142. Repair of damage due to insufficiency against antiplane shear forces on SRC 116
Figure 3-143. Gaps formed within assembly wood to wood joints....116

1 EXECUTIVE SUMMARY

1.1 INTRODUCTION

Zero-emissions steam generation with photovoltaic panels and an electric boiler is inefficient (~18% peak) and expensive (~$18-$23/MMBtu for commercial systems). Steam generated from natural gas can cost as low as $5-8/MMBtu in California including transportation and boiler efficiencies. We are developing a low-cost solar boiler to generate zero-emissions steam at a target levelized cost of steam competitive with natural gas. The achievement of such a low energy cost requires a breakthrough in the installed cost of the collector while maintaining the high thermal efficiency of a single-axis parabolic trough collector (73% peak and 50% annual). We identified the steel support structure as the highest cost component of the parabolic trough collector, and have proposed to replace steel with lumber as the structural material as a means of lowering the cost. Steel has been used for over a century for the trough structure. A trough based on a lumber spaceframe opens up a new design space for structural engineering, including the general geometry ("typology"), joint design and characterization, and assembly process to achieve the high level of accuracy needed for 80:1 concentration. This project takes the significant first step towards demonstrating the feasibility of achieving the low-cost and high performance of a lumber-based design through the systematic development of a full-scale prototype.

1.2 PURPOSE

The purpose of the project is to test the hypothesis that the industrial market requirements of a collector can be met with the GPTC with high confidence. Since the area of novelty is associated with the structure, we are concerned with optical requirements, namely an optical cost/performance ratio < 0.91 with a concentration ratio > 50 and a lifetime > 30 years. The cost/performance ratio is defined here as the ratio of total installed collector cost/m2 to the annual optical efficiency. This cost/performance target represents a disruptive reduction of 35% relative to the Energy Department SunShot 2020 target [1].

1.3 PROJECT OBJECTIVES

We aimed to raise the technology readiness level (TRL) of the GPTC from a concept (TRL2) to a prototype (TRL6) tested in a relevant environment. In the process, we sought to demonstrate

the potential of a significant cost reduction of the PTC. To reduce the degree of uncertainty in the cost, we took into account vendor quotations for material, and experience in assembly and installation of the prototype for the labor. We sought to achieve high confidence in meeting the performance by building and testing a prototype module in an operational outdoor environment. We aimed to gain confidence in the durability through accelerated testing of particular components combined with extended outdoor testing of the complete prototype.

1.4 PROJECT OUTCOMES

The key metric for the optical-structural performance is the intercept factor – the ratio of reflected light that intercepts the absorber tube. We measured a corrected intercept factor of 97% using a relative optical irradiance technique (Camera Target) near solar noon. A correction was applied due to non-straightness of the receiver tube. This intercept factor is very close to the predicted value (98%) based on the measured slope error over the collector, and supports the claim that the GPTC module can achieve the same level of performance as that of the state-of-the-art trough. The durability of performance over five months of testing is supported by the images taken of the targets over this period. A further indication of the evolution of performance over this period comes from monitoring torsional stiffness. There has been no indication of a reduction of torsional stiffness over the duration of the project. Nevertheless, we have seen local deterioration to the structure that did not manifest in the performance. We have diagnosed the causes for these local defects which indicate the need for a more detailed treatment in the design process in a second-generation collector, and it underscores the value in building a full-scale prototype. Due to the relatively short period of the project we also performed accelerated fatigue corresponding to thirty years of cycles, and weathering testing of joints to gain confidence in the lifetime. The results have not contradicted the compatibility of the GPTC with a long, e.g. thirty-year, lifetime. The process of building the first prototype has revealed areas for construction and assembly process improvements. If the improvements we have identified are implemented, we see a path to achieving the installed cost goal of $50/m2.

1.5 PROJECT MILESTONES

We defined a sequence of Milestones to measure our progress towards achieving our goals. The Milestones were designed using the methods of statistical hypothesis testing. Success for each Milestone meant that we could be meet the target Success Values with a confidence of 95%. A summary of all the Milestones is provide in the Report. The means of assessing the Milestones, and the assessment results are described in the Project Outcomes. Within this framework, all of the Milestone goals were met.

1.6 CONCLUSIONS AND RECOMMENDATIONS

We have shown that a 6m aperture parabolic trough with high concentration ratio (80:1) can feasibly achieve a very low installed cost, approaching $50/m2, while maintaining a high optical efficiency over a lifetime of several years with a lumber-based spaceframe construction. Outdoor full-scale module testing has revealed through structural health monitoring, local degradation mechanisms that have not manifested in a measurable reduction in optical performance. These observations, together with ideas for improved weatherability and efficiency of assembly, serve as the basis for an improved second-generation design. It is recommended that a full array of twelve second generation design modules is built to prove out assumptions of the improved process efficiencies and to validate the torsional behavior at actual scale. It is also recommended that the array is operated over a long-duration so that the degradation in optical performance and its maintenance costs can be assessed over a longer period of time.

This page intentionally left blank

2 INTRODUCTION

2.1 BACKGROUND

Nearly a quarter of all greenhouse gas emissions in California are attributed to the industrial sector [2]. A similar fraction can be found for nations as a whole. A large fraction of these emissions result from burning natural gas to generate steam for process heating and electricity generation with a turbine. A cost-effective alternative to natural gas for steam generation is needed to effect a major reduction on industrial emissions, and a solar thermal boiler is a promising candidate. However, conventional solar thermal power plants generate steam with a levelized cost of heat (LCOH) of ~ $10-15/MMBtu while steam generated from natural gas can cost as low as $5-8/MMBtu in California including transportation and boiler efficiencies. As most of the cost in a solar boiler is associated with the collector field, a major reduction in the installed cost is needed while maintaining a high thermal efficiency. The efficient generation of steam at industrial pressures ~ 11 bara (180°C) requires tracking concentrating collectors to maximize annual light collection and minimize heat losses proportional to receiver surface area. The conventional 6m aperture parabolic trough collector (PTC) achieves a peak thermal efficiency of ~73% at heat transfer fluid temperatures ~300°C high enough for the steam generator. The state-of-the-art PTC has a total collector installed cost of about $200/m2 and up to 84% of that cost is allocated to the steel structure that support the mirrors, and its foundation [3]. With so much cost concentrated in the structure, it invites alternatives, such as wood.
For the species and grade we have selected, wood costs only 15% of steel by weight, and it is widely available at lumberyards in the sizes of our choice across the USA Southwest. Wood has 5% of the embodied CO2e of steel [4]; little energy is used in the extraction, production, and transportation of wood, significantly reducing the environmental impact of structures made from this material. Wood is also well-understood as an engineering material that is effective for precision structures in terms of both stiffness and strength. Its stiffness-to-weight ratio (Young's modulus divided by density) is nearly identical to steel: 24.8 MPa/(kg/m3) for wood versus 24.5 MPa/(kg/m3) for steel. Therefore, wood provides essentially equivalent structural rigidity (response to wind and gravity loads) to steel with the same mass (in fact, nonlinear structural kinematics may require high strength and stiffer materials, such as steel, to use more mass than what it is required for strength and stiffness only to prevent buckling) – but wood is 15% of the cost/weight. While the use of wood is well-established as a cost-effective, environmentally sensitive, and high-performing option for large-scale structures such as buildings and bridges, it is unprecedented as the primary structural material in PTCs.

2.2 PROJECT OBJECTIVES

The focus of the innovation is the development of a new type of spaceframe for a parabolic collector of large aperture (6m). Our objectives have been defined to test the hypothesis that such a new collector type could meet market requirements. We have targeted an annual optical efficiency >55% with an installed cost of $50/m2, and a high concentration consistent with using 70mm absorber tubes), leading to a cost/performance ratio of <0.91. The achievement of this level of performance implies a high intercept factor (>90%) even in the presence of strong wind. It was therefore an objective to show through testing a single module that this intercept factor could be achieved at an array level. A further objective was to assess the long-term durability of the collector durability through a combination of months of outdoor exposure and accelerated testing of critical areas. Another key objective was to refine the cost model, using actual experience in assembly, and quotations on engineering drawings. By executing this systematic process, we will have raised the TRL of the collector from a concept (TRL2) to a prototype (TRL6) in a relevant environment and positioned the collector on a path to commercialization.

3 PROJECT OUTCOMES

3.1 ECONOMICS

We have built a techno-economic model of a solar boiler for an industrial plant to estimate the economic attractiveness of a plant consisting of a field of GPTC collectors performing at the simulated level, and reaching modeled installed cost. The financial model takes as input the annual energy and plant CAPEX and OPEX.

3.1.1 Annual energy yield

We determined the energy yield for a nominal 10 MW process steam plant using the modeled performance characteristics of the GPTC. The saturated steam pressure was chosen to be relevant to most industrial processing plants. The plant sizing and layout (number of SCAs and loops) was controlled by the design capacity and pressure drop constraints respectively. Table 3-1 summarizes the plant design parameters that are inputs to the annual simulation.

Table 3-1 Plant design parameters

Parameter	Value
SCA type	12 GPTC SCEs
SCE aperture area	72 m^2
Receiver type	Schott PTR 70
HTF	Duratherm 600
Number SCA per loop	2
Axis orientation	North-South, horizontal
Gap between SCA	1 m
Row spacing	12 m
Loop length	288 m
Number of loops	8
Design point DNI	900 W m^{-2}
Design point ambient temperature	20 °C
Thermal efficiency at design point	73.6% (calculated)
Design point heat rate	9.12 MW (calculated)

HTF inlet temperature	220 °C
HTF outlet temperature	280 °C
Saturated steam pressure	11.2 bara
Mass flow plant at design	57.4 kg s^{-1} (calculated)
Loop pressure drop	271 kPa (calculated)
Startup energy	2.1 MWh (calculated)

The reference site for the simulation is Las Vegas. The key result of the simulation is the annualized thermal efficiency ηtherm defined in Eq. (1):

$$\eta_{thermal,annual} = \frac{\sum_{8760} Q_{net}}{ApertureArea_{Solar\ Field} \sum_{8760} DNI} \qquad \text{Eq. (1)}$$

For this calculation the hourly DNI is taken from the TMY3 file for Las Vegas. Qnet is determined on an hourly basis and includes startup losses, hourly absorbed energy, and total heat losses from the receiver tubes and piping. The mass flow is controlled to keep the outlet HTF temperature constant. The simulation produced the result ηtherm = 52.5%. This result, which closely agrees with NREL's System Advisor Model calculations, along with the field aperture area and annual DNI determines the annual energy yield that is used later in the IRR calculations. For statistically based IRR calculations that may be used in project finance models we consider the historic variability of the DNI, not the TMY, in the determination of the variability in the annual energy yield as discussed below.

3.1.2 Total installed collector cost model

The following cost model is based on a complete bill of materials and vendor quotes. Each collector consumes approximately 1250 board feet (bf) of lumber. We buy lumber of random lengths and have them delivered to the project site for $0.35/bf. The wood is cut at the site to the right length and end angles according to the design. Cut members are then transported to the painting station. All surfaces are painted. Then, painted members are mated together using pre-setup table jigs to enforce the critical dimensions and to speed up the process. Nail-plates are pressed using portable presses. The following tables show our updated cost estimate.

Table 3-2 Collector cost model

Item	$/m2
Lumber	$6.82
Spaceframe hardware	$5.74
Pylons hardware	$2.16
Foundation	$4.60
Mirrors	$16.50
Drive assembly, equipment and instruments	$3.24

Lumber components fabrication and painting	$4.60
Spaceframe assembly	$5.12
Total	**$48.50**

3.1.3 Complete plant CAPEX model

A complete cost model of the plant was constructed including CAPEX and soft costs. CAPEX is divided into equipment and materials, shipping, installation, and commissioning. The soft costs include engineering and project management, permitting, and banking fees. We report the costs without contingency added. The cost is based on the same design corresponding to that used in the energy yield model. The major Balance of Plant (BOP) equipment includes heat exchanger (Kettle boiler), expansion vessel, and HTF pump. We specified all of the above-mentioned equipment (and the weather station) and received quotations for each of them. Their installation costs were estimated by an EPC professional. EPC estimates were made for the minor equipment including electrical and instruments (e.g. control valves, cables), local control boxes, UPS, and rented civil equipment. Major material costs include HTF, piping, fittings, valves, and insulation. The HTF price per gallon was given in a quotation, and we estimated the inventory needed. Piping related costs were estimated by an EPC professional based on a preliminary piping layout. Civil costs were estimated by an EPC professional on the basis of acreage. Commissioning and soft costs were estimated based on EPC experience.

3.1.4 Financial model

We built a Monte Carlo-based statistical model in Python for the plant IRR by extending a single-valued deterministic IRR calculation to include statistical distributions in cost and energy yield. The yearly variation of DNI has been used in previous statistical studies of CSP energy yield [5], and the uncertainty of energy yield has been carried further into economic outcomes such as levelized energy cost [6]. The present work goes a step further by including variations in cost - specifically taking into account the historical price of the primary collector construction material - and by computing IRR. The Monte Carlo method is implemented by producing a large statistical sample of IRRs. Each IRR in the sample is determined by calling an IRR function with an array of DNI values and a single CAPEX. The length of the array of DNI values corresponds to the number of years of plant operation, so that in every year of operation a new DNI is used as the basis for the yearly energy yield. The DNI values and the CAPEX are generated from probability distributions. The IRR function solves for the discount rate such that the net present value of the total project costs and discounted cash flow is zero. The discounted cash flow is calculated from the after-tax cash flow from steam sales. The various assumptions included in this calculation are given in Table 3-3.

Table 3-3 Assumptions for IRR model

Parameter	Value	Notes
Commercial operation date (COD)	2020	Determines applicable ITC and bonus depreciation rates
Inflation rate	2.5%	Assumed
Thermal efficiency	52.5%	From annual energy yield calculations
Plant aperture area	13,824 m^2	Plant sizing to meet steam capacity
Annual energy degradation rate	1.5%	Assumed
Soft costs	$423,000	EPC estimate
First year OPEX/CAPEX	1%	Assumed
First year steam price	$7/MMBtu	Corresponds to $6.3/MMBtu natural gas price for 90% boiler efficiency.
Energy price escalation rate	3.5%	Assumed
Federal income tax rate	35%	Assumed
State income tax rate	0%	Nevada
Salvage value	$ 0	Assumed
Years of operation	20	Assumed heat purchase agreement terms acceptable for market
CAPEX	Random variable	Function of random lumber price
DNI	Random variable	Distributed according to historical record

To include a measure of variability of the CAPEX, we focus on the main subject matter of the project, i.e. the collector. One of the main areas of novelty of the collector is its use of a forestry product for the structural material. The baseline material is kiln dried Douglas Fir. We take as an assumption that the probability distribution of the future lumber price can be projected from the price history. We found two sources for historical prices, a report published by the USDA [7] and data from a leading industry website [8], forming a complete record from 1971 to the present. The composite price data for the unit of thousand board feet (mbf) is plotted in Figure 3-1. The main price drivers have been housing starts and federal land management policy. The frequency distribution (probability distribution) of the total installed collector cost, shown in Figure 3-2, is determined from the collector cost model which includes the random lumber price. (The lumber price is selected by choosing the year from the historical record with uniform probability). Finally, the CAPEX probability distribution arises from the collector cost component of the CAPEX model.

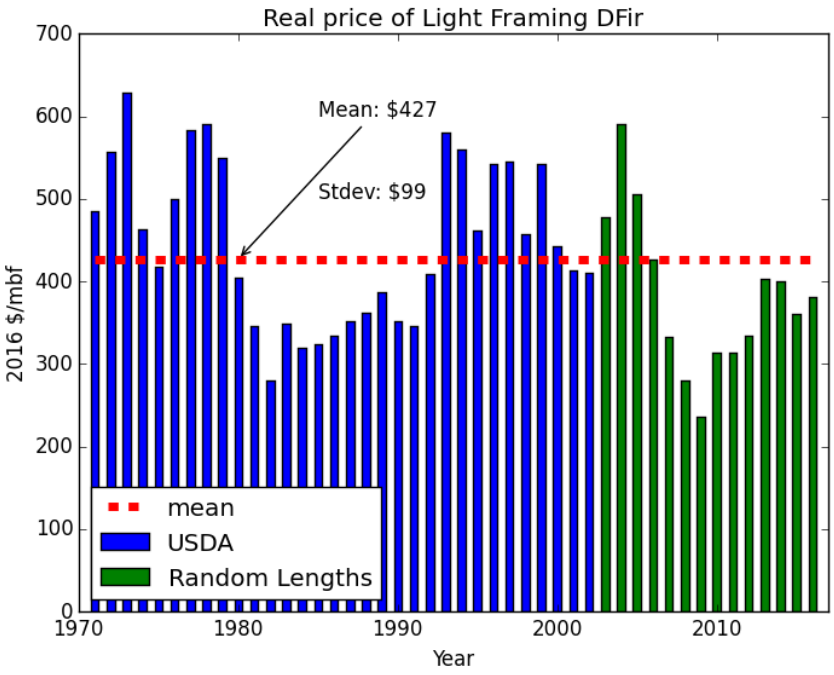

Figure 3-1. Historical lumber price

As with the historical lumber price, we use the historical DNI record at the reference site to serve as the basis for the probability distribution of DNI. The National Solar Radiation Database (NSRDB) published two databases, a first from 1961-1991, followed by a second from 1991-2011. We use the composite data shown in Figure 3-3 from both records to determine the DNI probability distribution.

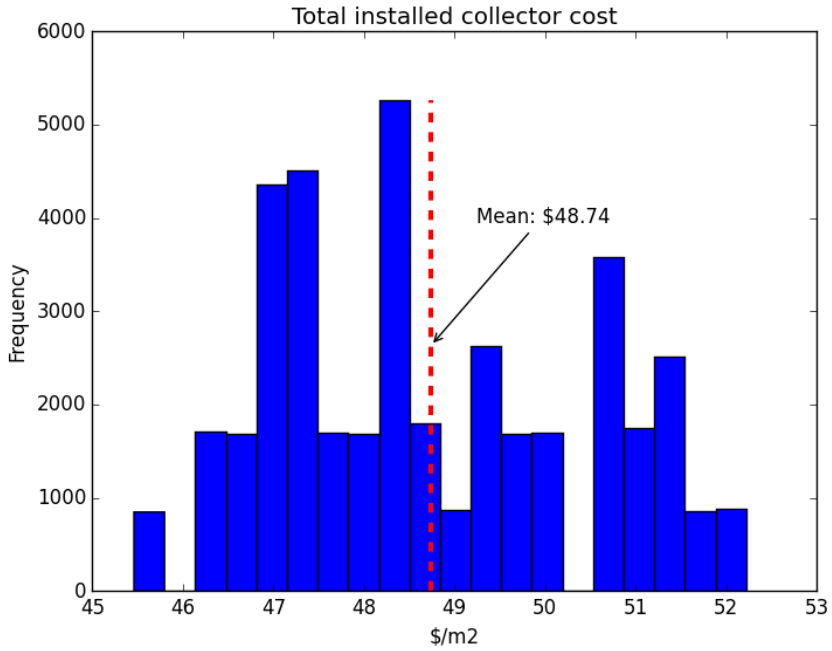

Figure 3-2. Total installed collector cost frequency distribution (40,000 samples)

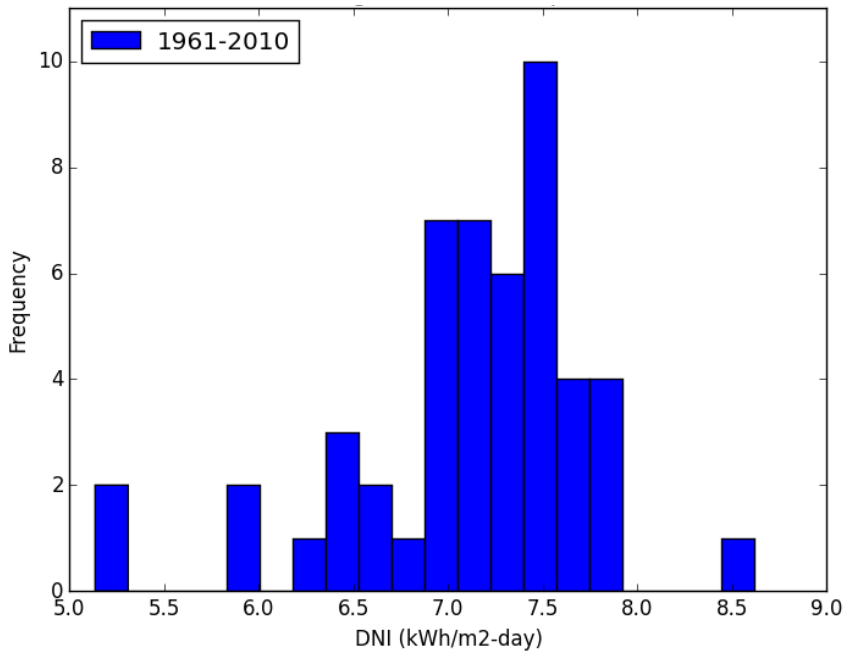

Figure 3-3. Composite NSRDB records for Las Vegas

The plant IRR function is calculated n times to produce a statistical sample of size n. Each IRR in the sample uses a random CAPEX drawn from the probability distribution and a series of random DNI corresponding to the years of operation. The Monte Carlo result is shown in Figure 3-4 for the case n = 1000.

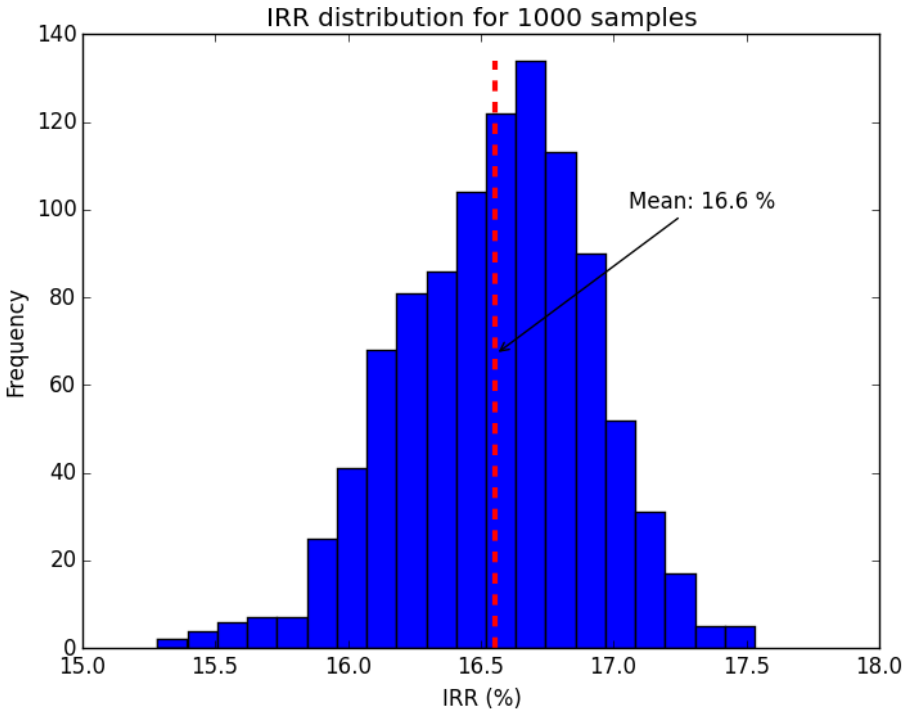

Figure 3-4. IRR frequency distribution from a sample size of 1000

Figure 3-4 illustrates that the investor can expect a market-competitive return under the assumptions presented, selling steam to customers who would contract to pay a price equivalent to $6.3/MMBtu for natural gas.

3.2 COLLECTOR ENGINEERING

The collector engineering was divided in three stages. Stage 1 consisted of preliminary structural engineering analysis and simulation for the determination of specifications for component testing. Stage 2 consisted of investigation of the mechanical behavior of the main components. Stage 3 consisted of mechanical and structural engineering of the collector as a whole.

3.2.1 Engineering analysis prior component testing

Wood is a common structural material for a variety of applications. Thus, the mechanical strength of many wood species and joint types are well-known. However little data exists on the stiffness and fatigue behavior of wood joints, in particular nail-plates and various screwed joints. From structural-optical simulation of the collector, together with historical data of wind events at Las Vegas, we developed a test protocol for accelerated fatigue tests of wood members and joints.

3.2.1.1 Effects of gravity diurnal cycles

The collector rotates to follow the trajectory of the sun. This rotation leads to load cycles with a one-day period. The amplitude of the cycles can be estimated from the structural simulation by tracking the stress magnitude at a particular location for different collector's elevation angle. The number of cycles is equal to the number of days of the collector is expected to serve (i.e. 30 years). The internal force history for the identified most critical element (the element subjected to high loading cycles was a diagonal member close to the drive) is shown in Figure 3-6 (lower curve shown for diurnal gravity forces). Results suggest the application of 11,000 cycles (i.e. approximate number of days in 30 years) of the load pattern shown in Figure 3-6. Note that since all joints rely also on contact between members when subjected to compression, tensile forces are expected to be more critical.

3.2.1.2 Effects of wind forces

Components will be subjected to cycles not only due to the change in orientation of the collector while tracking the position of the sun, but also, we identify important load cycles due to wind speed history.

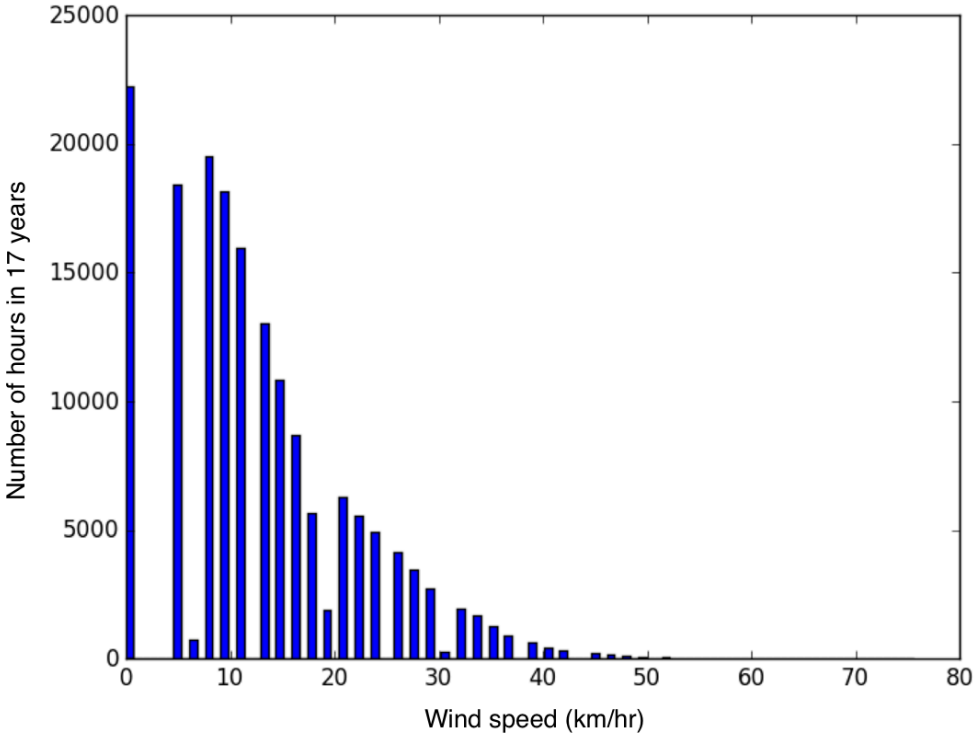

Figure 3-5. Wind speed frequencies for Las Vegas (2000-2016) [9]

The most critical element's (the one with highest tensile stresses) internal axial force could be as high as 12,000 N (for wind speed of 56km/hr according to empirical relations between wind speed and pressure obtained by [12] for the collector with elevation angle of 60° and yaw angle of 0°). Note that Figure 3-5 shows only the number of hours that a particular wind speed was recorded. We followed the standard Rainflow algorithm [10] to identify the number of load cycles versus the load amplitude range. This algorithm is a counting method that is widely used in fatigue analysis (in conjunction with Miner's rule) and for test protocol specification in physical simulations. The input for this algorithm is the loading time history. For a conservative estimate of the load cycles, it is assumed that the collector is at 60° elevation and yaw (i.e. the angle between collector axis and wind direction) angle of 0° every time. The following table summarizes the results for Las Vegas.

Table 3-4 Wind force cycles for Las Vegas site

Range (Newton)	Cycle Count	Average Amplitude (Newton)	Mean (Newton)
12664 to 14071	1.76	7035	1.15E+04
11257 to 12664	2.65	5904	1.04E+04
9850 to 11257	1.76	5343	9445
8442 to 9850	13.24	4367	8945
7035 to 8443	12.35	3807	8544
5628 to 7035	49.41	3114	8318
4221 to 5628	80.29	2409	7398

2814 to 4221	**501.18**	**1655**	**6703**
2111 to 2814	**716.47**	**1208**	**6409**
1407 to 2111	**2164.41**	**837.5**	**6006**
704 to 1407	7685.29	491.7	5576
352 to 704	14430.00	245.5	4980
0 to 352	56006.47	78.43	4475

From preliminary fatigue test results, we expect the joints to be relatively insensitive to number of cycles with amplitude lower than 1500N. On the other hand, we neglect those cycles that occur fewer than 100 times in 30 years. Cells shaded with green correspond to those cycles of interest. Based on that information, we applied the load cycles represented in Figure 3-6.

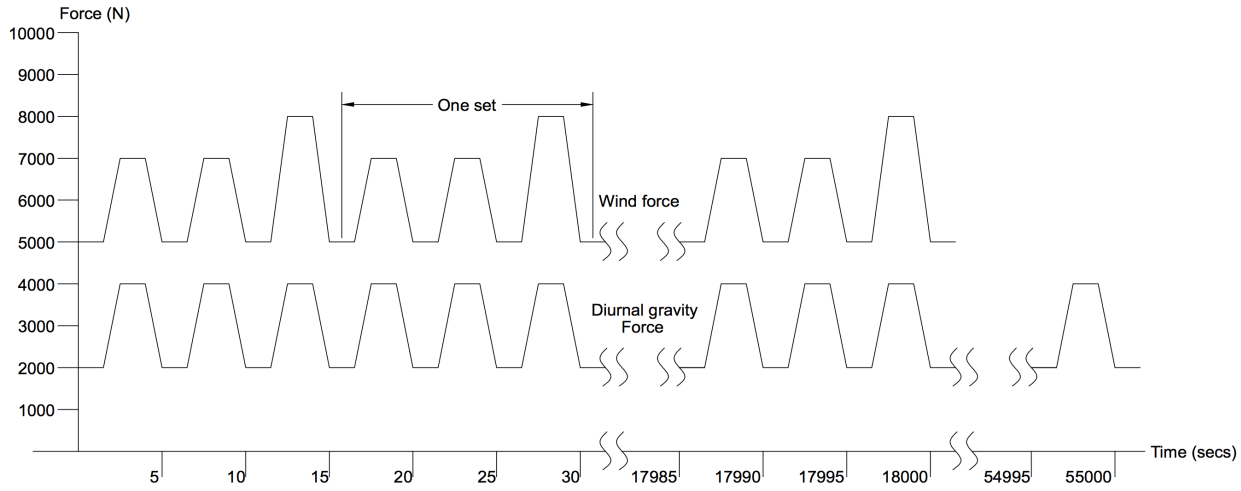

Figure 3-6. Load history for diurnal gravity and wind forces

3.2.2 Test specification

Given that diurnal gravity forces consist of cyclic forces with a much lower range value, (being the mean force only half of that of the wind force cycles) we expect the mechanical behavior of the joints to be more sensitive to the wind force pattern. From the cycle information shaded with green in Table 3-4, we define a test protocol consisting of 1200 sets (with a typical set is indicated in Figure 3-6) for a total of 3600 cycles. Thus, each specimen will be subjected to 2400 cycles of 1000N amplitude with mean of 6000N and 1200 cycles of 1500N amplitude with mean of 6500N. This is worse than the loading conditions shaded in Table 3-4.

3.2.2.1 In-house testing equipment for fatigue tests

Our tensile tester consists of a linear actuator mounted in an aluminum frame which is supported on a sturdy steel table. The aluminum frame flexes approximately ½" at full load, allowing the actuator to move through a substantial portion of its stroke and avoid wearing out the teeth at a single spot on its internal gear train. The actuator connects through a hole in the table to the top

of the wood specimen. The lower end of the specimen is bolted securely to the concrete floor. Clevis pin clamps are tightened with 1-inch bolts at the top and bottom of the specimen to provide a rigid connection. Figure 3-7 shows the overall arrangement of the device.

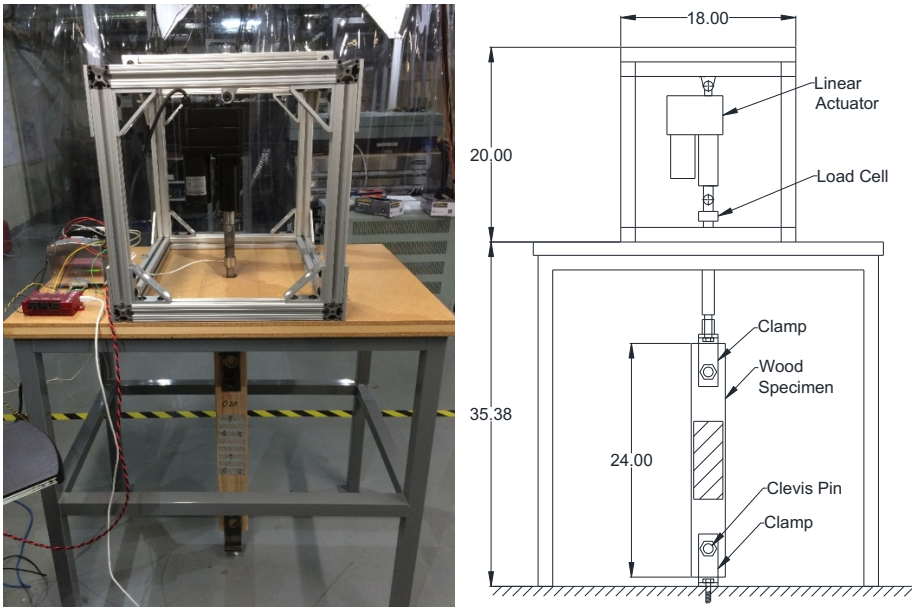

Figure 3-7. Photo and overall schematic of tensile testing machine with dimensions in inches.

The tensile testing machine utilizes a data acquisition (DAQ) system and sensors that control the device and record data from the test:

a. A load cell mounted in line with the actuator and the specimen measures the tensile load.

b. Two displacement sensors (potentiometers) measure the displacement of the joint. They are typically mounted on each side of the joint and the average of the two is used to measure the displacement to compensate for rotation. This setup allows the measurement of the joint stiffness (load vs. displacement) in real-time during the test. The potentiometers are mounted on a sliding aluminum extrusion mechanism that allows rapid adjustment for different gauge length specimens and can be quickly tightened to secure the sensors in place. To assemble the sensors the user first assembles the potentiometers and pushrods loosely. Then the locking screw is loosened and the position of the push rod is fine-tuned to the desired position. Finally, the locking screw is tightened in place.

c. A DAQ box records the data at a typical frequency of 4 Hz. The DAQ software scales the input signals to record the data in the desired units.

d. A small microcontroller board operates the actuator with a routine that allows repeated application of a desired load for a given duration. The control program monitors the load on the load cell and retracts the actuator until the desired load is reached. It pauses for the desired duration. It lowers the load by extending the actuator until the desired load is

reached, then pauses. This basic cycle is repeated the desired number of times. Utility programs allow small retract or extend movements to facilitate actuator motion during specimen set up.

e. Two SPDT (single pole dual throw) relays are used to achieve a DPDT (dual pole dual throw) motor control set-up and enable bi-directional operation of the actuator.

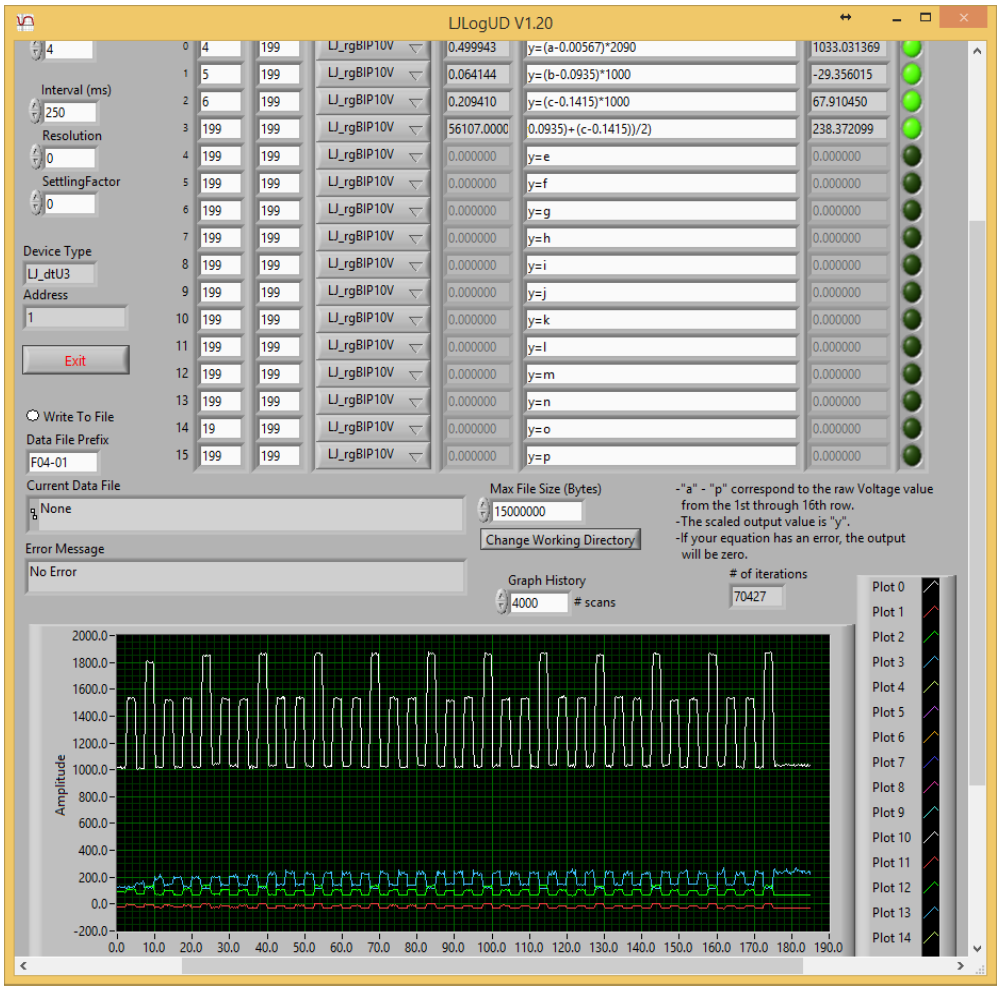

Figure 3-8. DAQ UI showing example test data.

Figure 3-8 shows an image from the DAQ user interface (UI) after a brief fatigue test. The data trace shows load in lbs. (white), left and right displacement channels in microns (red and green), and calculated stiffness in kN/mm (blue).

3.2.2.2 Fatigue test setup and measurements

We focused our attention on the preferred joint types: Truss joints (using Mitek M-20 3”x8” nail plates with forces acting parallel to the nail plates and the wood grains) and two types of

diagonal member joints: 1) using wood to wood screws and 2) using metal plates with slight oversize holes for Simpson's PC screws as shown in Figure 3-9

a) Truss joints setup

b) Diagonal member wood to wood screws

c) Diagonal member joints using metal tie plates

Figure 3-9. Test setup for fatigue and initial stiffness testing

The setup is designed so that tensile forces is applied through the clevis ends and local deformation is measured using potentiometers. In the case of the truss joints, the potentiometers measure deformation over a gauge length of 9 inches (i.e. 1-inch offset from the joints). For diagonal member joints, we are simply interested in the gap between the two members that are joined together by wood to wood screws. Two sensors reading are averaged to compensate for imposed rotations due to eccentric loading conditions and/or due to the nonsymmetrical nature of the resisting forces at the joints. The stiffness parameter we are interested in is the ratio of the applied force to the total deformation (Ks in Figure 3-10). We call this parameter the secant stiffness, as it is the slope of a chord that connects the origin to the load reference point in the force vs displacement curve (see Figure 3-10). We use 8000 Newtons as a load reference for stiffness characterization. The sensors are set to zero at a load level of about 800 Newtons. All deformations that accumulate due to mechanical fatigue are considered when determining the evolution of the stiffness. In the actual collector structure, all deformations that accumulate after mirror alignment contribute to performance loss. Note that tangent stiffness (Kt in Figure 3-10) may not degrade as fast as the secant stiffness.

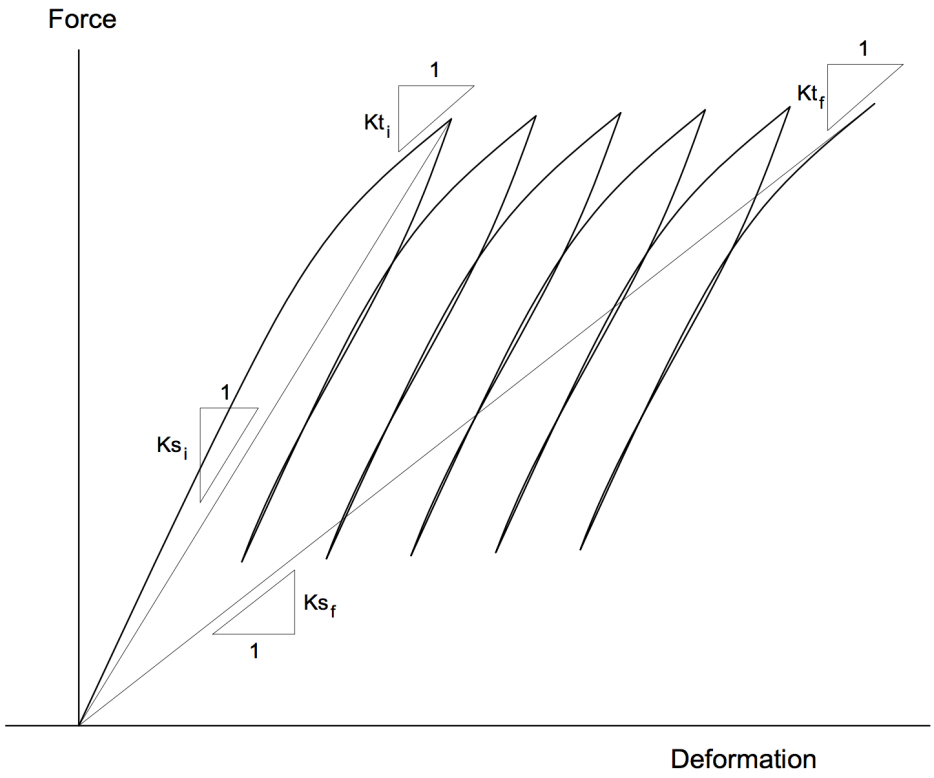

Figure 3-10. Schematic representation of a force-vs-deformation relationship. Sub-indices "i" and "f" stand for initial and final respectively.

3.2.2.3 Structural modeling assumption regarding the behavior of joints

For simplicity, structural components are modeled as linear elastic materials. Thus, the model will not account for complicated hysteresis nor any nonlinearity in material response. Since we require the model to accommodate the deformations each component experiences after fatigue, the stiffness parameter we use to characterize the model is the secant stiffness (Ktf in Figure 3-10). Modeling components as linear elastic requires us to make sure no traces in experimentally measured force vs deformation fall below a straight line that passes through (0,0) (i.e. zero force and zero deformation) with a slope equals to Ktf, to avoid underestimation of the deformation. Since the collector was designed for a minimum performance of 90% intercept in high wind considering all joint stiffness equals to 9kN/mm, we take this as the minimum for acceptable performance. In force-vs-deformation relationships, a straight line intercepting the origin with a slope of 9kN/mm divide the force-deformation space in two regions: 1) Acceptable performance where force to deformation ratio is equal or greater than 9kN/mm and 2) poor performance where force to deformation ratio is lower than 9kN/mm.

3.2.3 Fatigue test results

The allowable stiffness of 9kN/mm is plotted together with the experimental results of the joints to assess their performance. We now present the results for each joint type.

- Truss joints

Figure 3-11 and Figure 3-12 show the behavior of the truss joint design when subjected to 3600 cycles. Specimen F01-02 was actually subjected to 14000 cycles with higher amplitude (as seen in Figure 3-11) and no significant degradation was observed. Figure 3-11 and Figure 3-12 show acceptable performance for truss joints. The average aged stiffness (i.e. the force to deformation ratio after cycling) of the four joints tested was 81.8 kN/mm and the standard deviation was 23.7 kN/mm. This corresponds to a degradation of 12% of the initial stiffness.

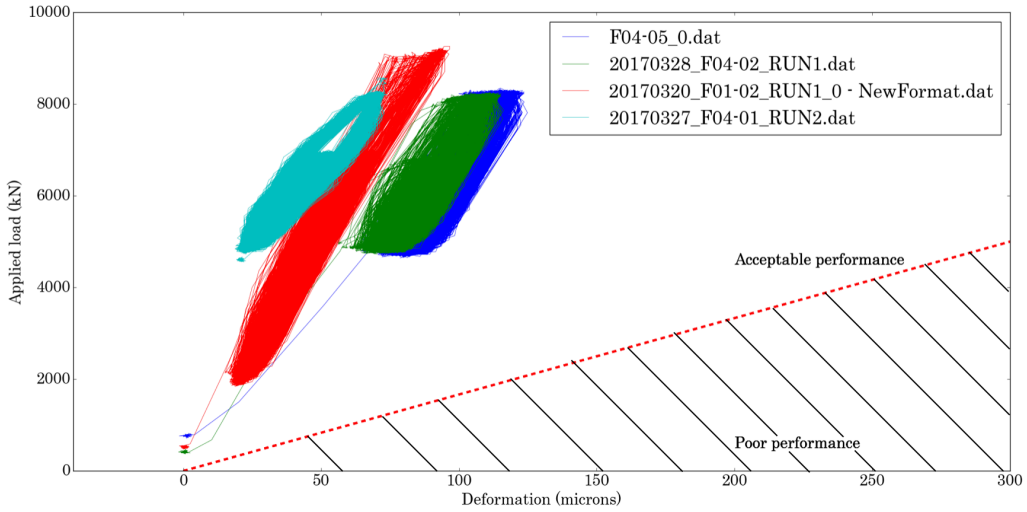

Figure 3-11. Force-vs-deformation relationship for 4 truss joints subjected to 3600 cycles.

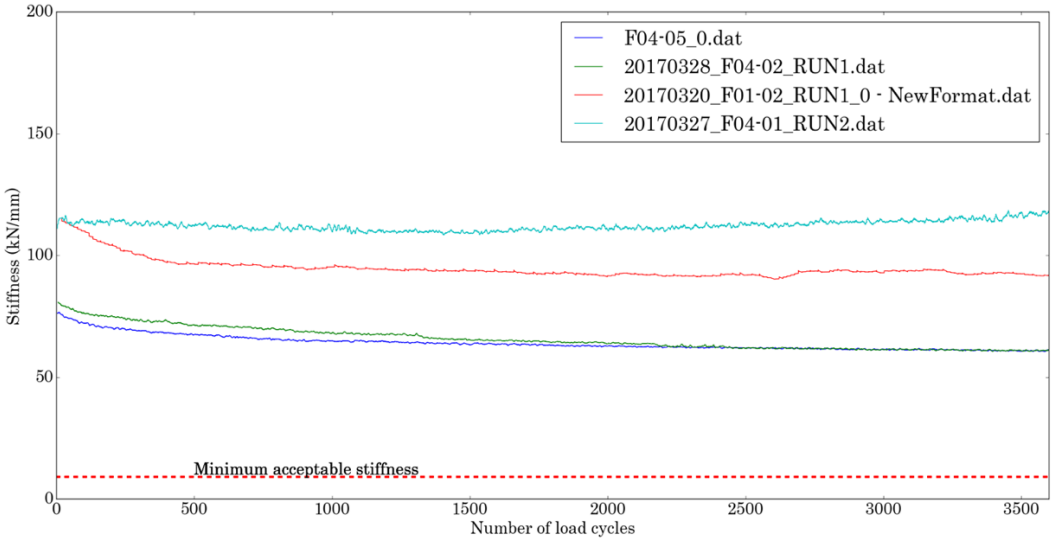

Figure 3-12. Evolution of truss joint stiffness when subjected to 3600 cycles

- Diagonal member joints
  - Metal tie plate with wood screws

Diagonal members could be attached to trusses via steel brackets with holes for wood screws as shown in Figure 3-13

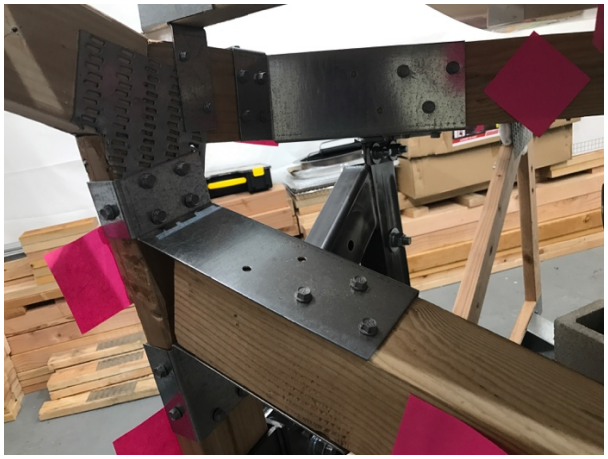

Figure 3-13. Photograph of diagonal member to truss joints using steel brackets

This joint configuration relies on screws in shear as well as in tension. A characterization of the stiffness of this joint from first principles requires the understanding of the behavior of a joint consisting of a tie plate with screws acting in shear as shown in Figure 3-14 and Figure 3-15. Very few tests were conducted on this type of joints since we discovered it would not perform as required.

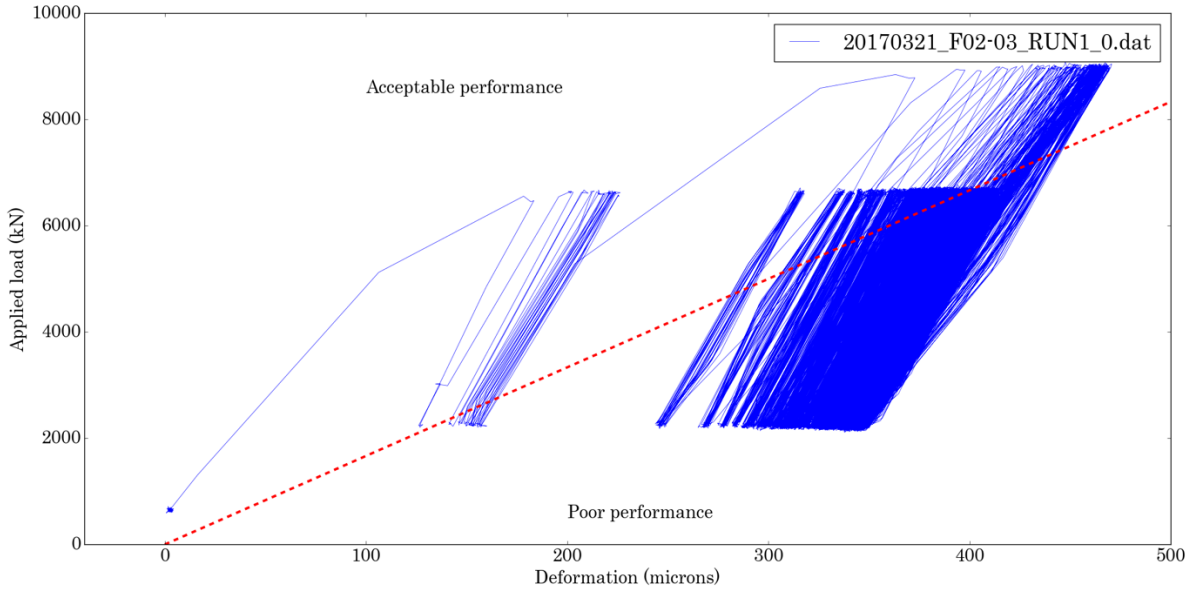

Figure 3-14. Force-vs-deformation relationship for a tie plate joint subjected to 3600 cycles.

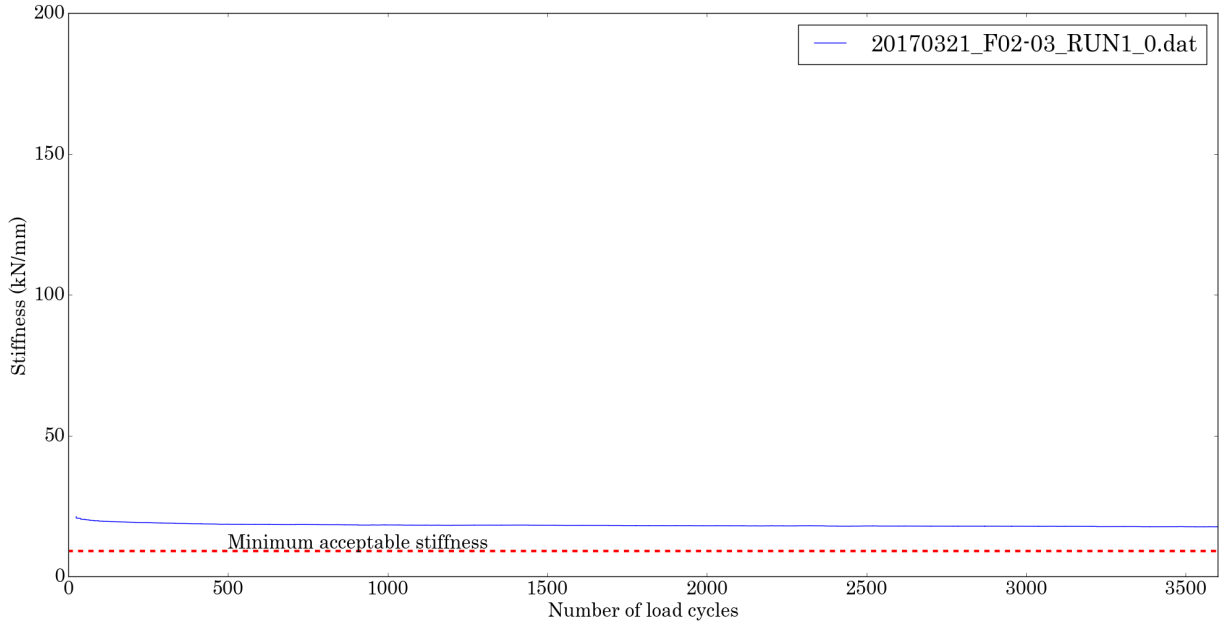

Figure 3-15. Evolution of stiffness of the tie plate joint

Note that for high loads, the force vs deformation traces stay above the threshold (i.e. the straight line with a slope of 9kN/mm). However, after fatigue, many traces fall to the poor performance region. This suggested the development of the actual preferred joining technique as described in the next section.

- Wood to wood joints

A design using wood to wood screws was considered as an alternative of using brackets with wood screws. The design is depicted in Figure 3-16.

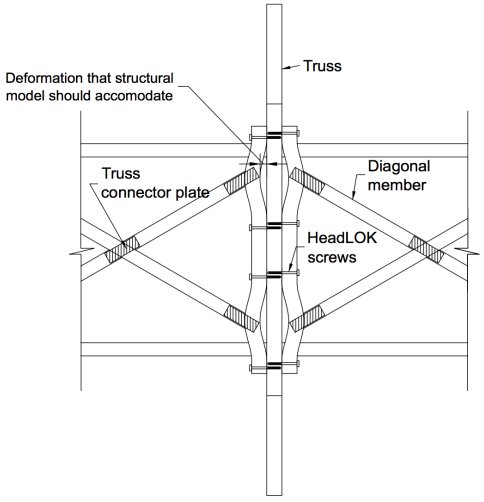

Figure 3-16. Diagonal members joined to trusses using wood to wood screws

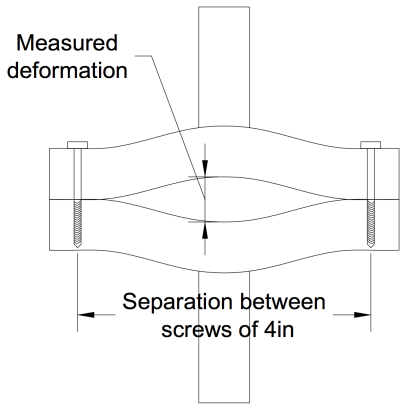

Figure 3-17. Test setup for wood to wood joints

Note that the diagonal member subassembly includes an additional wood member parallel to the trusses to accommodate the wood-to-wood screws. The cost model account for that design and it was shown to be more economical, leading to a reduction of about $0.50/m2. In this design, there are no steel brackets at all. To study the mechanical behavior of such joints, a test setup was designed as indicated in Figure 3-17. The force vs deformation relationship and the evolution of the stiffness are shown in Figure 3-18 and Figure 3-19.

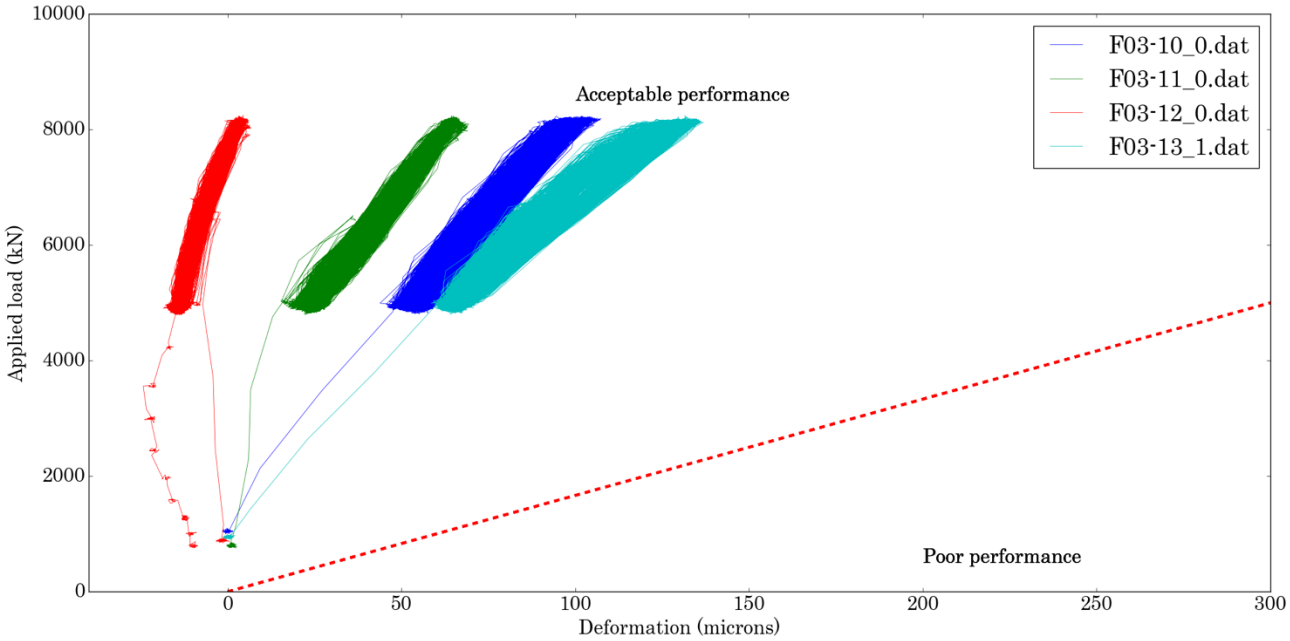

Figure 3-18. Force-vs-deformation relationship for a wood to wood joint

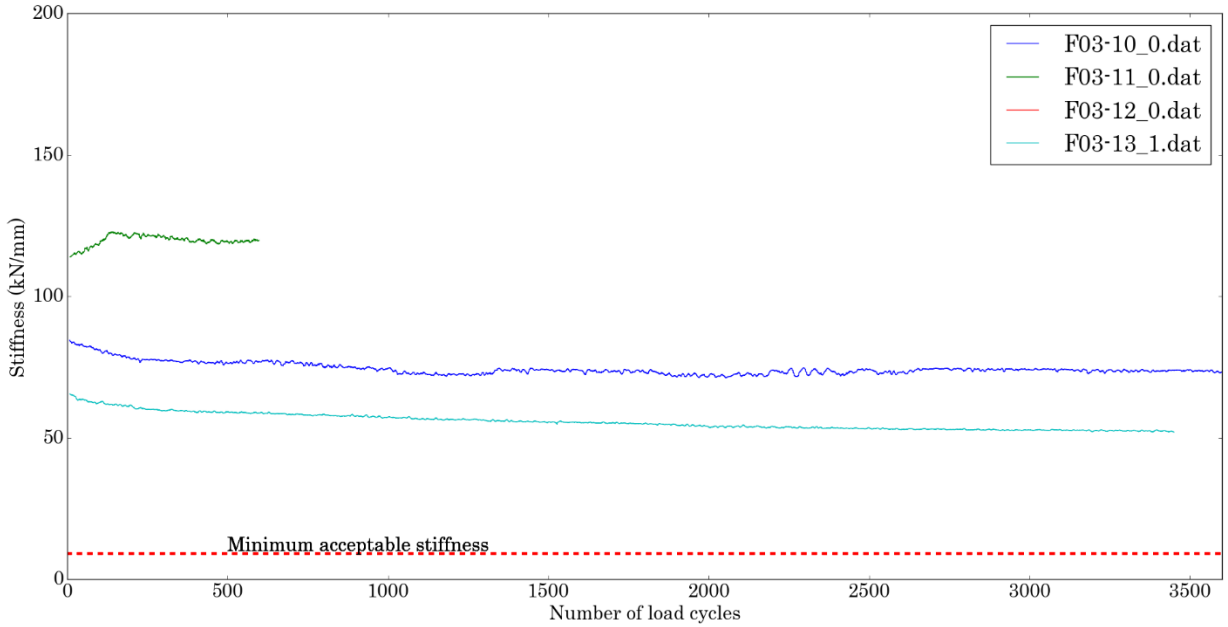

Figure 3-19. Evolution of truss joint stiffness of the wood to wood joint

Note that all traces stay on the acceptable performance region. Wood-to-wood joints showed a higher stiffness than the required for acceptable performance after mechanical fatigue. Specimen F03-12 experienced a stiffness higher than 200kN/mm, thus, it is not shown in Figure 3-19. The average stiffness of the aged joint is 81.67 kN/mm and the standard deviation is 28.32 kN/mm.

3.2.4 Accelerated weathering

We carried out accelerated weathering tests on different joints to test the effectiveness of different coating products in preventing degradation of the stiffness. The motivation of these tests is to find a solution for joints that resist severe weather conditions. The test cycle consists of 3.5 hrs of soak, followed by 1 hr of freezing, and then approximately 19 hours of drying. We assume that for each rain event, the specimens undergo freezing and full drying (i.e. removal of all moisture gain during rain), each cycle correspond to a rain event. This is, of course, a very conservative assumption. We identified around 21 rain events in a typical year in Las Vegas. We established that 21 cycles of testing equal 1 year of outdoor exposure in Las Vegas. Three different paint types were tested (*viz.* latex based, oil based, and neoprene) and all of them have been shown to sufficiently protect the wood for the first 78 moisture cycles. Specimens are weighed before soaking and before drying. In Figure 3-20, the weight of each specimen is plotted versus time for unfinished samples and for samples coated with latex paint.

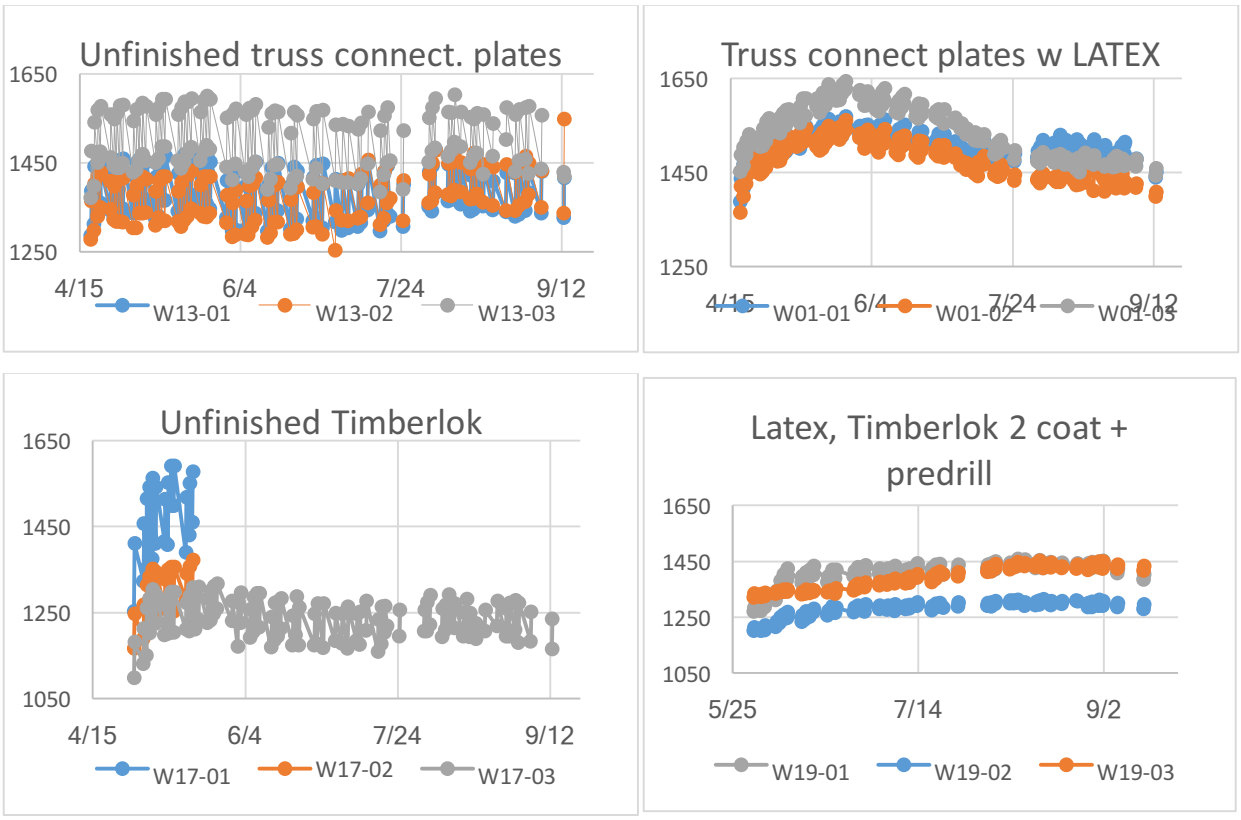

Figure 3-20. Evolution of specimen weight (in grams) over time

Figure 3-20 shows that painted specimens experience much lower moisture cycle amplitude. It suggests that for painted specimens, the number of high amplitude moisture cycles per year could be significantly lower than the number of rain events.

- Qualitative comparison between specimens in their initial state and after the application of 78 moisture cycles

Figures 34 to 37 show a comparison between specimens before and after applying moisture cycles. Unfinished joints experience visible back out and/or splitting. In painted specimens, paint color has changed but the specimens have experienced no back out and very small cracks.

Initial state

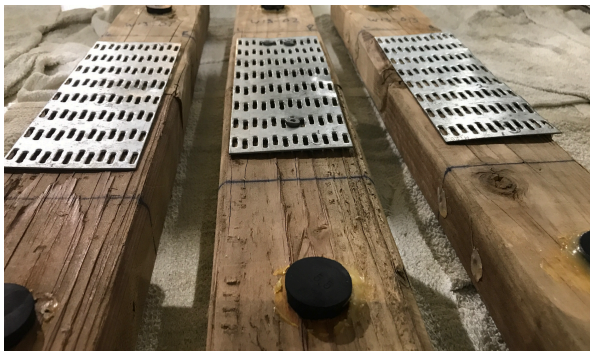

After 78 cycles

Figure 3-21. Unfinished specimen

Initial state

After 78 cycles

Figure 3-22. Truss connector plates with LATEX paint

Initial state

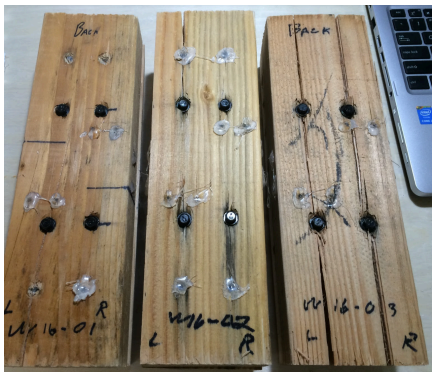

After 5 cycles

Figure 3-23. Unfinished TimberLOK joints

Initial state After 53 cycles

Figure 3-24. TimberLOK joints with 2 coats of LATEX paint

- Stiffness measurement

The stiffness has been measured for some of the specimens to track their evolution with moisture cycles. Stiffness testing has indicated that truss connector plates degrade with moisture cycles (up to 60% degradation after 60 cycles for unpainted specimens) but still are able to provide the minimum required stiffness to meet the required optical performance. For TimberLOK and ScrewLOK joints it was observed that splitting needs to be prevented. Stiffness falls below acceptable values for specimens having fully opened cracks (such as the ones shown in Figure 3-23). As soon as a macro crack initiates, the stiffness of these joints degrades. Several strategies were discovered via experimentation to minimize cracks. We tested many strategies separately and *no splitting was observed*. We state with confidence that, as it is in the current design, the combination of all these strategies will lead to a joint with high resistance to weathering. Based on the available information so far, we conclude that for a project site with about 15 rain events (note that they should occur sufficiently apart from each other to allow wood to develop a moisture cycle), we expect no degradation in optical performance during the first five years of life. Bio-attack is mitigated by choosing protection techniques and special coatings resistant to moisture, as well as means to control the moisture content through structural design and wood treatments known in the industry.

3.2.5 Optimization

3.2.5.1 Calculation of the intercept factor γ

The intercept factor is defined as the fraction of reflected light that strikes the cylindrical absorber tube and is the measure of optical quality for the trough. We calculate γ through fast two-dimensional raytracing using an algorithm incorporated within the structural optimization framework so that the energetically relevant performance metric is used is in the objective. The validity of the 2D approach is a result of the extruded trough geometry, as long as the vector analysis is performed by projecting onto the plane normal to the extrusion axis. The interface between the perturbed structural geometry and the optical analysis is implemented through arrays

of normal vector errors (rotations to the normal), with each array representing a different longitudinal slice of the trough. Rays are sampled uniformly in space across the aperture and non-uniformly in direction across the sunshape. To construct the proper non-uniform directional sampling in the transverse direction $\boldsymbol{\theta_r}$ we integrate the radial brightness in the longitudinal direction $\boldsymbol{\theta_l}$, using a radial brightness model validated by measurements of the disk and aureole A useful feature of this model is the parametrization of the aureole by the circumsolar ratio. The final result for the projected directional distribution is given by

$$B(\theta_r) = \int_0^{\sqrt{a^2-{\theta_r}^2}} d\theta_l \, \frac{\cos\left(c_1 \sqrt{{\theta_r}^2 + {\theta_l}^2}\right)}{\cos\left(c_2 \sqrt{{\theta_r}^2 + {\theta_l}^2}\right)} + \int_{\sqrt{a^2-{\theta_r}^2}}^{\sqrt{b^2-{\theta_r}^2}} d\theta_l \, e^{\kappa} \, ({\theta_r}^2 + {\theta_l}^2)^{\frac{\gamma}{2}} \qquad (1)$$

Where a and b are the angular radii of the disk and aureole (4.65 and 43.6 mrad), and $\mathbf{c_1}$, $\mathbf{c_2}$,γ, and κ are parameters defined in [11]. Equation (1) is plotted in Figure 3-25 for a clear day (circumsolar ratio of 5%).

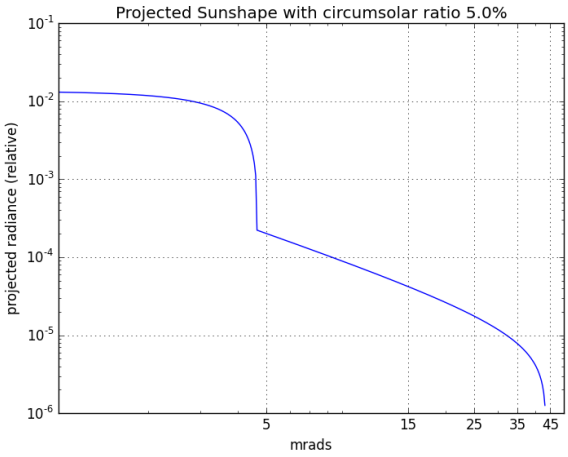

Figure 3-25. Projected sunshape with circumsolar ratio of 5.0%

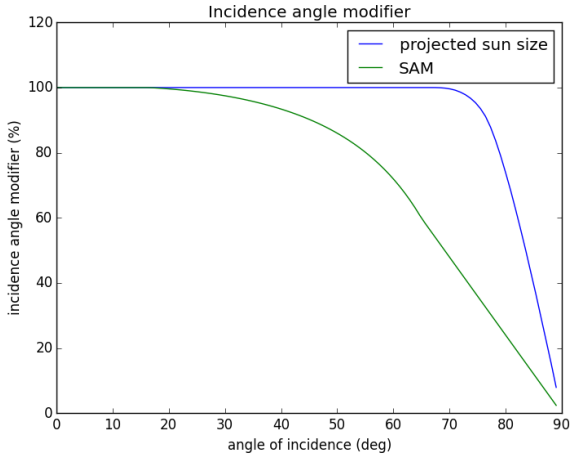

Figure 3-26. Incidence angle modifier

3.2.5.2 γ and the IAM

It should be noted that the sunsize parameters a, b are those corresponding to an angle of incidence of zero (AOI). For other AOI the apparent sunsize is larger, and gives rise to a reduction of intercept factor for very large AOI. This effect is actually a component of the IAM function, so the non-normal γ is not treated separately and we instead use the empirically determined IAM as used in the System Advisor Model. The System Advisor Model ("Model") is software developed by the National Renewable Energy Laboratory ("NREL"), which includes other energy losses. The IAM is plotted in Figure 3-26. We found from outdoor testing that the IAM of the GPTC closely followed the SAM IAM function.

3.2.5.3 *Algorithm for automatic generation of structural model and intercept factor computation*

To maximize computational efficiency of an optical performance-based structural design of the collector, an automated collector structural model generator was developed. A structural model for the collector is generated by specifying a set of parameters shown in blue color in Figure 3-27

	B	C	D	E	F	G	H	I	J	K	L
2	Collector structural design										
3	Model automatic generation										
4	Geometric case		3	(See figures)		for case 3, use only 32 mirror elements in F9					
5	Collector aperture		5.774	m			Collector angle	90	deg	INTERCEPTF	87.09464591
6	Collector Focal distance		1.71	m			Collector wind loads:				
7	Collector Length		12	m			x-x direction	48.5917	N/m2	Define resolution of	
8							z-z direction	-37.1583	N/m2	Slope error per element	
9	Mirror mesh resolution (# of elements 1D)				32	(16 or 32)	y-y direction	0	N/m2	Resolution	10
10	Number of longitudinal elements				8	(8 or 4)	Mirror segments along length			6	
11	Truss geometric characteristics										Ang error
12	Structure on the front		No	Eliminate nodes 11 and 12?			Yes				
13	A	2.888	m	Open Sap		Build SCE		Intercept Factor		Angle Error	0.005387025
14	B	1.444	m							Balance	
15	C	0.61004	m	Close SAP			Build SCA				
16	D	3.51018	m						Unbalance Moment		-7.48282201
17									Vertical Reaction		44630.22067

Figure 3-27. Structural model automatic generation

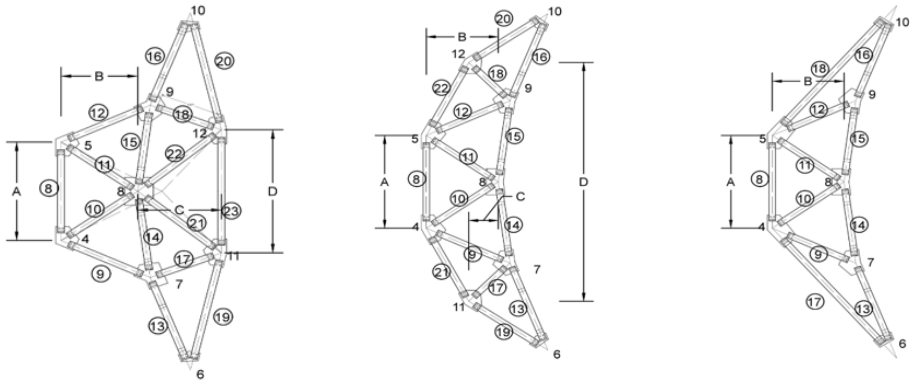

a) Case 1 b) Case 2 c) Case 3

Figure 3-28. Structural design geometric cases

Depending on the geometric case chosen in cell D4, a different structural typology is generated. For each typology, Figure 3-28 shows the geometrical meaning of the design parameters A, B, C and D. Note that Case 1 includes structural elements in the concave side of the mirror. This was the typology presented in the original proposal. Case 3 is the simplest (fewest members and connections) and potentially the most optically efficient (no shading) we therefore hypothesize that it is the preferred configuration. However, we need to demonstrate that it has the required optical quality (intercept factor) and robustness to material and geometric variability. Case 2 is less aggressive than Case 3 and it was included to provide additional degrees of freedom in the design space exploration. Our proprietary Excel program calls the structural analysis software (SAP2000) API functions to generate and run the structural model and then the program imports

results of nodal displacements of mirror surface and space-frame member axial stresses. Our program then uses the deviation of the normal vector to compute the intercept factor as discussed previously and it is reported in cell L5.

3.2.5.4 Search for the most optimum structural truss design

The program tested over one thousand different set of parameters to minimize the weight of the structure while maintaining high optical performance using a gradient based global (random multi-start point) optimization algorithm. Different objective functions and starting points were used. The variables used during each trial were summarized in a table that looks like one shown in Figure 3-29

	A	B	C	D	E	F	G	H	I	J	K	L	M	N	O	P
1	All dimmensions are in meters						Truss		Long		Torque					
2	Trial #	A	B	C	D	GeomCase	Base	Height	Base	Height	Base	Height	Total Weight	Slope RMS	Intercept	IF/Weight
3	1	1.6	1.64	0.5	4	2	0.05	0.1	0.05	0.1	0.05	0.1	2080.845237	0.004087937	98.5981	0.047383661
4	2	1.6	1.64	0.5	4	2	0.05	0.1	0.05	0.1	0.05	0.1	2080.845237	0.004087937	98.5981	0.047383661
5	3	1.6	1.64	0.5	4	2	0.05	0.1	0.05	0.1	0.05	0.1	2080.845237	0.004087937	98.5981	0.047383661
6	4	1.6	1.64	0.5	4	2	0.05	0.1	0.05	0.1	0.05	0.1	2080.845237	0.004087937	98.5981	0.047383661
7	5	1.6	1.64	0.5	4	2	0.05	0.1	0.05	0.1	0.05	0.1	2080.845237	0.004087937	98.5981	0.047383661
8	6	1.6	1.64	0.5	4	2	0.05	0.1	0.05	0.1	0.05	0.1	2080.845237	0.004087937	98.5981	0.047383661
9	7	1.6	1.64	0.5	4	2	0.05	0.1	0.05	0.1	0.05	0.1	2080.845237	0.004087937	98.5981	0.047383661
10	8	1.6	1.558	0.475	3.8	2	0.0475	0.095	0.0475	0.095	0.0475	0.095	2080.845466	0.004087937	98.5981	0.047383655
11	9	1.6	1.476	0.45	3.6	2	0.045	0.09	0.045	0.09	0.045	0.09	2009.788234	0.004135541	98.2938	0.048907561
12	10	1.6	1.312	0.4	3.2	2	0.04	0.08	0.04	0.08	0.04	0.08	1936.854361	0.004205725	97.7658	0.050476598
13	11	1.6	0.984	0.3	2.4	2	0.03	0.06	0.03	0.06	0.03	0.06	1809.919915	0.004448648	95.9504	0.053013605
14	12	1.6	1.29018	0.39335	3.14678	2	0.03933	0.07867	0.03933	0.07867	0.03933	0.07867	1604.538899	0.006201522	81.6646	0.050895985
15	13	1.6	1.312	0.4	3.2	2	0.04	0.08	0.04	0.08	0.04	0.08	1775.951755	0.005786714	82.7829	0.04661325
16	14	1.6	1.312	0.4	3.2	2	0.04	0.08	0.04	0.08	0.04	0.08	1801.57585	0.004507661	95.2342	0.052861605
17	15	1.6	1.312	0.4	3.2	2	0.04	0.08	0.04	0.08	0.04	0.08	1801.57585	0.004507661	95.2342	0.052861605
18	16	1.6	1.312	0.4	3.2	2	0.04	0.08	0.04	0.08	0.04	0.08	1802.504232	0.004495803	95.3829	0.052916858
19	17	1.6203	1.394	0.425	3.4	2	0.0425	0.085	0.0425	0.085	0.0425	0.085	1802.505289	0.004495803	95.3829	0.052916827
20	18	1.61015	1.353	0.4125	3.3	2	0.04125	0.0825	0.04125	0.0825	0.04125	0.0825	1860.485249	0.004349452	96.4552	0.051844094
21	19	1.60254	1.32225	0.40312	3.225	2	0.04031	0.08063	0.04031	0.08063	0.04031	0.08063	1834.912316	0.004386078	96.3365	0.052501944
22	20	1.60032	1.31328	0.40039	3.20312	2	0.04004	0.08008	0.04004	0.08008	0.04004	0.08008	1811.256016	0.004456444	95.7681	0.052873878
23	21	1.60002	1.31208	0.40002	3.2002	2	0.04	0.08	0.04	0.08	0.04	0.08	1803.635142	0.004487877	95.4641	0.05292872

Figure 3-29. Structural design exploration

3.2.5.5 Worst-case wind load estimation

Hosoya, N., et al. [12] performed wind tunnel tests of parabolic through solar collectors. They reported wind pressure coefficients for wind loads acting at different directions and for different collector elevations. The coefficients reflect an amplification factor of wind pressure of a reference flat (i.e. non-concave) surface. For each loading conditions, they report mean as well as maximum and minimum pressure coefficient. For the design optimization, we consider mean values for pressure coefficients. According to the reported coefficients and structural simulation of a solar collector array (consisting of 12 solar collector elements), the most critical wind load scenario is when the collector is pointing 60° from the horizontal axis.

3.2.5.6 Sun model used for intercept factor

For the purpose of performing design exploration in which we are interested in comparison between optical performance of different structural typologies, a simplified sunshape (uniform radial brightness up to disk edge) was used to speed up computation. However, for the performance analysis, we used a the more complex sun model discussed earlier that gives a more accurate prediction of intercept factor.

3.2.5.7 Preliminary vs optimized design

During the design exploration, structural configurations that included members in the concave side of mirror surface were observed to be heavier, and in general, they did not provide improved optical performance. For the most critical wind loading condition, torsional deformation is what led to the greatest reduction in optical performance. The torsional resistance is achieved using elements that are always on the convex side of the mirror surface. As more structure is disposed to provide torsional stiffness there is diminishing structural benefit to disposing members to the concave side. Case 1 was therefore determined to be inferior to Case 3 on grounds of lower annual optical performance (shading) and higher cost (extra material and connections). The following table shows a comparison of the intercept factor of the structural typology of our preliminary design and that of the most optimal structural system that only include structures on the convex side.

Table 3-5. Comparison between preliminary and optimized design. Performance computed for worst case operating wind condition

Model	Preliminary design	Optimized design
Parameter A	1.6	2.8
Parameter B	1.11	1.4
Parameter C	1,2	-
Parameter D	2	-
Geometric case	1	3
Truss element dimensions	2” x 4”	2” x 4”
Longitudinal elements dim	2” x 8”	2” x 6”
Torque element dim	2” x 8”	4”x4”
Total Weight (per SCE)	1937kg	1796kg
Slope error RMS	7mrad	4mrad
Intercept Factor	69%	94%

3.2.6 Simulation of aged structure

The aged structure is simulated with the measured values of joint stiffness after cycling. For statistical significance, a Monte Carlo simulation was performed considering a new set of parameters based on our measurements of the stiffness after mechanical fatigue. Each parameter is modeled as standard normally distributed random variable characterized by their mean and standard deviation. The simulation also accounts for random errors in tracking, collector alignment, receiver position and mirror fabrication. Each of the errors is considered a random variable with standard deviation equal to half the tolerance limits for each of them. Monte Carlo simulation leads to the distribution for collector performance in terms of simulated intercept factor shown in Figure 3-30. The Z statistics are 29.83, which is > -1.645. It was observed that at certain level of joint performance (joint stiffness greater than about 30 kN/mm) the optical performance becomes less sensitive to the joint stiffness.

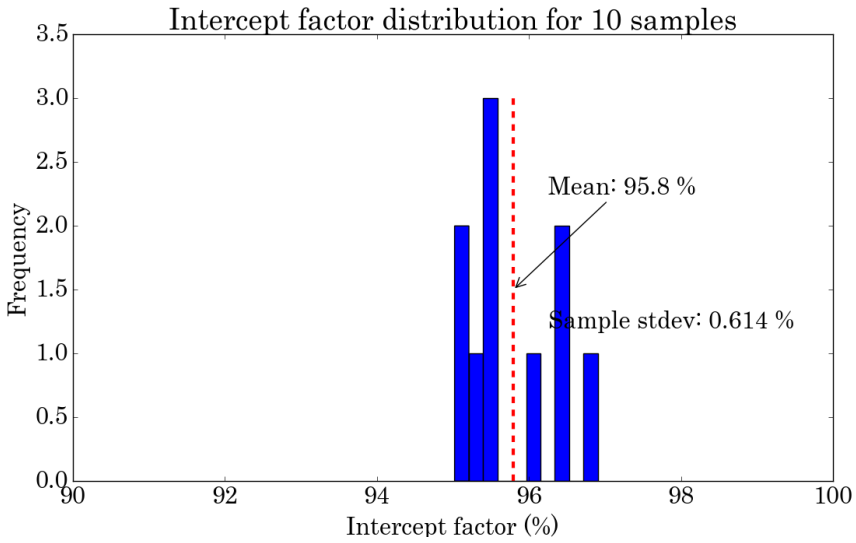

Figure 3-30. Monte Carlo simulation of aged structure

3.2.7 Full-scale module prototype design

The opto-structural design of large parabolic trough collectors should address three distinct design requirements: resistance to splay deformation, resistance to torsional deformation, and a means of precisely attaching the mirror panels to form the overall optical surface. While means have been found that satisfy these requirements for steel structures, novel solutions were needed for a lumber-based structure. We are presenting the design features necessitated by the use of lumber that satisfy the structural performance requirements for Splay Resisting Components (SRC), Torsion Resisting Components (TRC), and Mirror Support Elements (MSE) in a way that is easy to manufacture and is durable in the presence of environmental stresses such as wind and moisture. Figure 3-31 shows the different views of the collector.

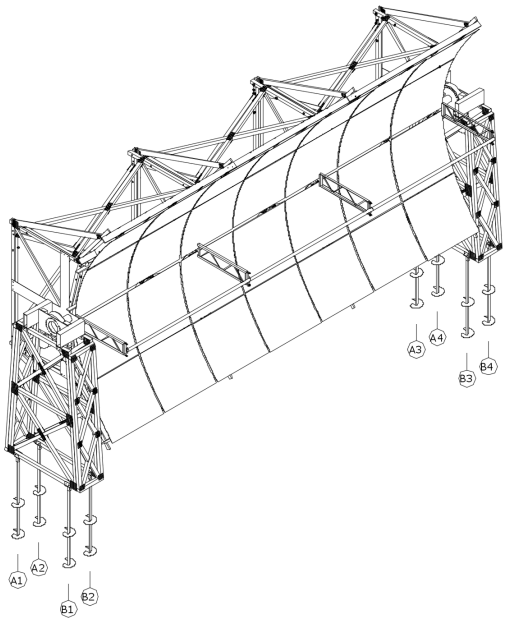

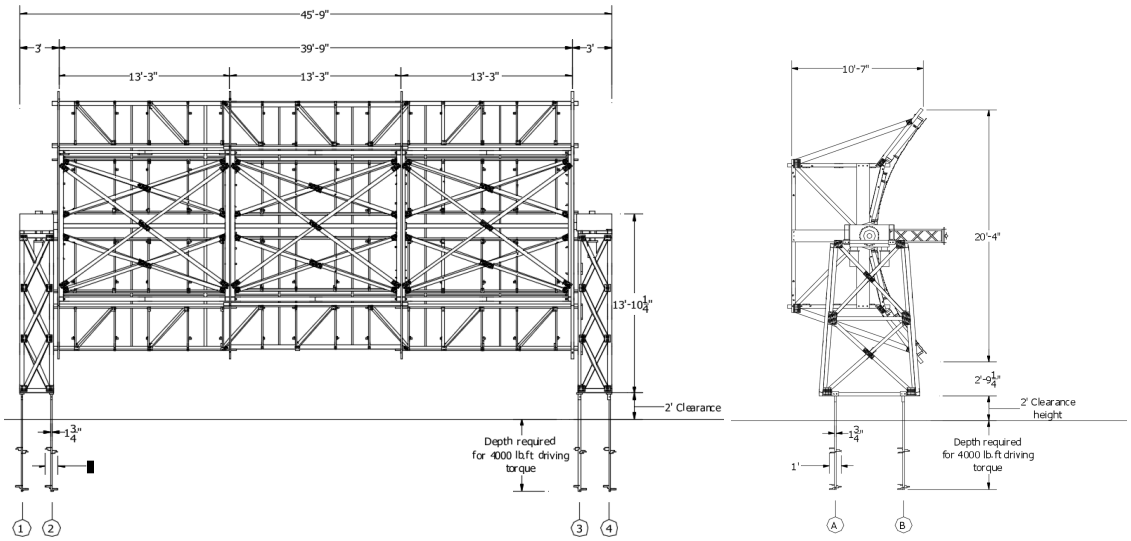

Figure 3-31. Isometric view [top], posterior view (from convex side) [left] and lateral view [right]

The prototype to be built consists of a collector module of about 46ft long and 20ft aperture width. It is attached to the ground by helical piles that are driven up to a torque of at least 4000 lb-ft. The helical piles should allow for an offset between the collector and the ground of about 2ft. This offset is needed for protection of the wood from soil contact. The piles interface with the pylons via a component that consists of a clamp at the pylon end and a pin connection at piles. The pylons consist of four trusses of two types as shown in Figure 3-32.

Lateral force resisting truss Longitudinal force resisting truss

Figure 3-32. Pylon trusses design

The lateral force resisting trusses need to resist forces acting perpendicular to mirrors. They are required to provide stiffness so that the spaceframe does not experience significant rigid body rotation. The longitudinal force resisting truss provide stiffness in the collector's longitudinal direction. No significant amount of force is expected to be acting in that direction. These trusses are assembled using conventional roof truss manufacturing technique. Truss connector plates were used to join 4x4 wood components. The four trusses are assembled together using lag

screws. A slewing drive rotates the collector to track the sun. The slewing drive interfaces with the spaceframe and drive pylon via flange connection. Figure 3-33 shows an isometric view of the drive pylon and the slew drive.

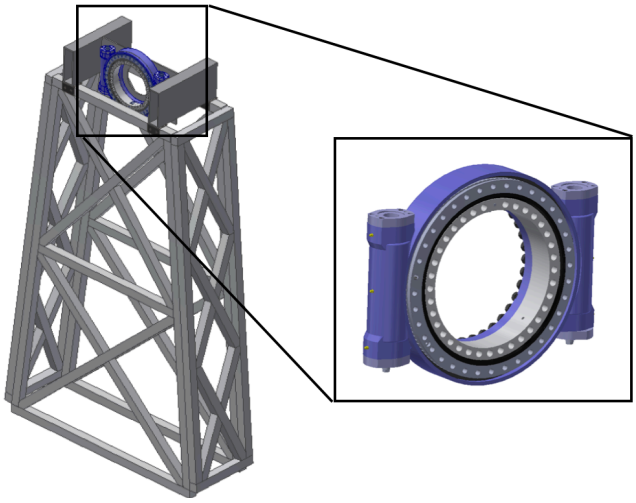

Figure 3-33. Isometric view of drive pylon [left] and slew drive [right]

Both the drive pylons and the slew drive were designed to provide a combined torsional stiffness that is at least twice the torsional stiffness of one collector module. Doubling the stiffness of one frame ensures that the drive assembly is at least 12 time stiffer than the array, then, localized deformations within the drive assembly is expected to be small compared to that of the frame. The spaceframe components are also fabricated using conventional roof truss manufacturing technique. The components are discussed in detail in the following paragraphs.

- Splay resisting components

The splay resistance of the spaceframe is provided by trusses that consist of nine 2x4s (members b, c, d, e and f) and two 2x6 members (members "a") joined together using truss connector plates. The joints are designed to maximize connector plate engagement with wood members. Figure 3-34 shows the elevation view of the truss design. The member "b" in joint "J1" was extended to prevent splitting due to screw insertion near the end of the member when attaching the mirror support elements to it. The geometry of Joint "J2" (Figure 3-10) allows for exterior mirror support element to be easily installed without position measurement. The connector plate in joint J4 is offset from the bottom of the collector to allow screw bolt fasteners to be attached as shown in Figure 3-36.

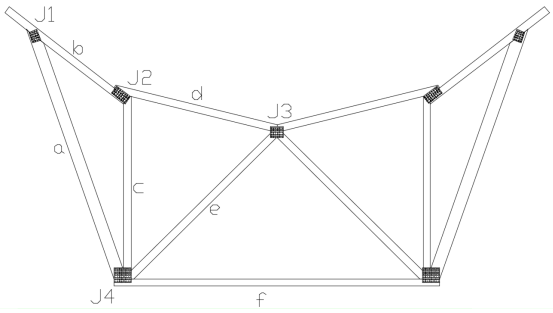

Figure 3-34. Splay resisting component

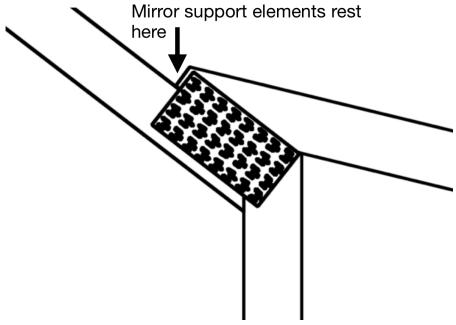

Figure 3-35. Joint "J2"

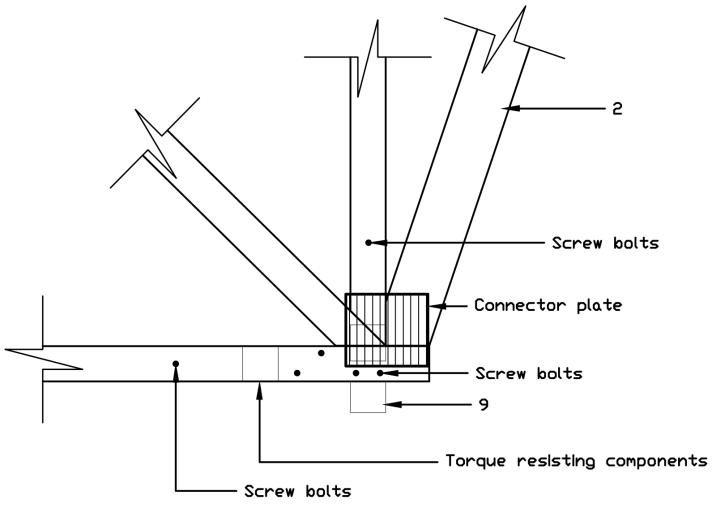

Figure 3-36. Joint "J4" [13]

- Torsion resisting components

Torsion is resisted by assemblies that consist of diagonal crosses as the one shown in Figure 3-27

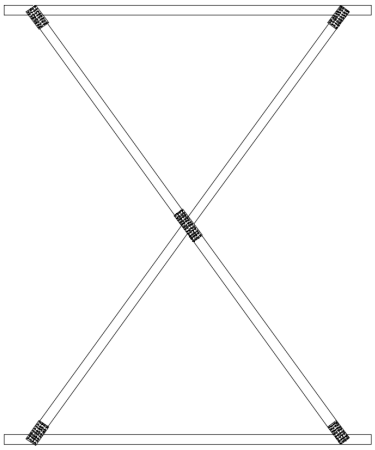

Figure 3-37. Torsion resisting component

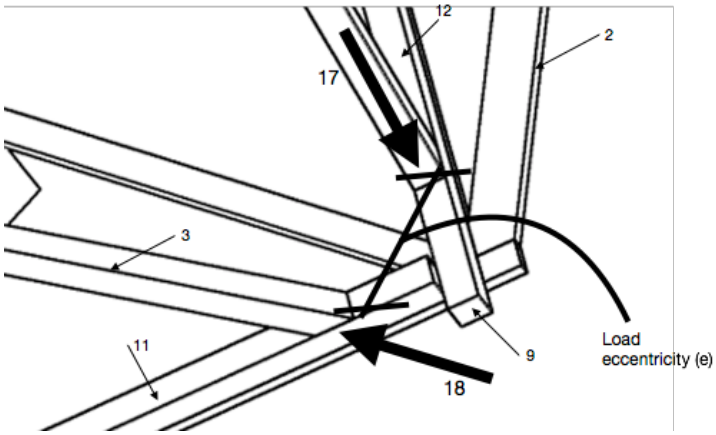

Figure 3-38. 3D representation of Joint "J4"

4x4 members are joined together using truss connector plates. The horizontal members (called interfacing members) in Figure 3-37 are designed to mate the splay resisting components to allow the use of wood-to-wood fasteners. Note that an interfacing member was annotated with number 9 in Figure 3-38 and with a number 2 in Figure 3-39. A 3D representation of the joint "J4" is shown in Figure 3-38. The interfacing members are often extended to provide out-of-plane strength and stiffness to splay resisting components. This out-of-plane resistance is required to successfully bridge the eccentric forces (shown in Figure 3-38 annotated with number 18) that come from two adjacent torsion resisting components.

The torsion resisting components are attached to splay resisting components via screw bolts in a way that two interfacing members sandwich a splay resisting component so that the three components are joined together by a single fastener. Wood lag screw can be added for additional strength if needed. In Figure 3-39, a splay resisting component (annotated with number 2) is sandwiched by two interfacing elements (annotated with number 11).

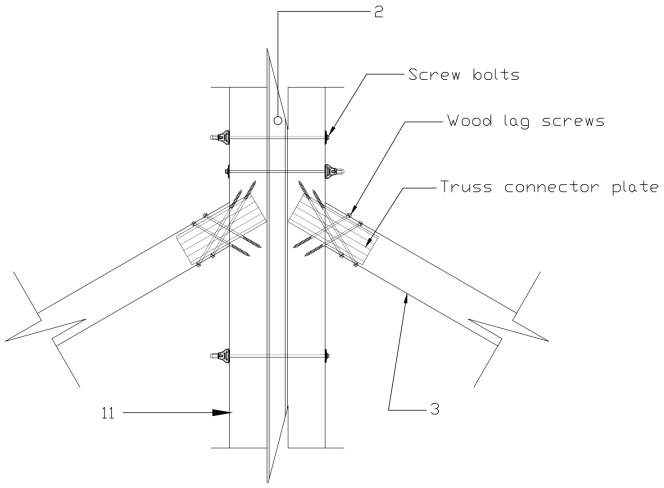

Figure 3-39. Details of joints of torsion resisting components and splay resisting components

- Mirror support sub-assembly

To support the mirrors, a subassembly with the form of a ladder was designed to directly interface with the mirror support brackets. Figure 3-40 shows the assembly for exterior mirrors, wherein 2x6 lumber was used to provide sufficient out-of-plane stiffness. Diagonal bracing is used to provide in-plane stiffness to the assembly to avoiding sagging of the assembly during rotation of the collector. Figure 3-41 shows the assembly for interior mirrors. Lumber of size 2x4 is used instead of 2x6, and no bracing was needed since the subassembly for interior mirrors is attached to torsion resisting components.

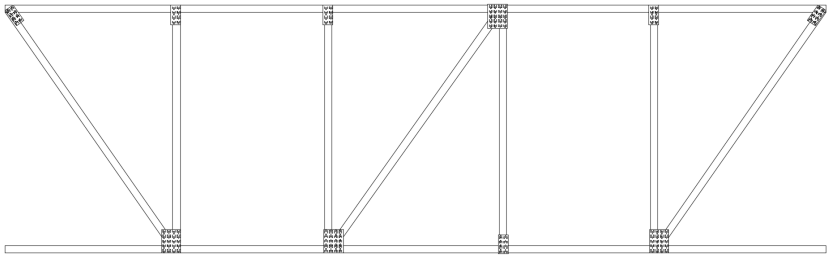

Figure 3-40. Exterior mirror support sub-assembly

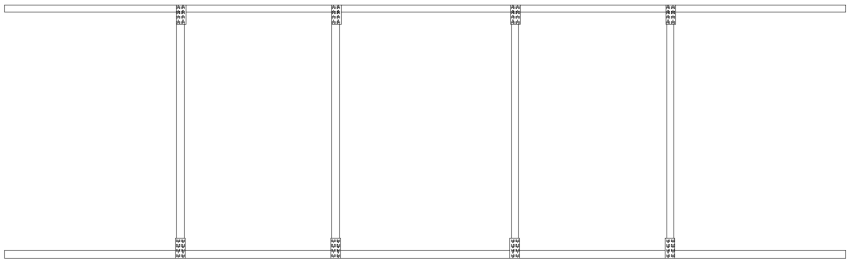

Figure 3-41. Interior mirror support sub-assembly

The mirror support subassemblies provide a plane available for mirror brackets alignment as shown in Figure 3-42.

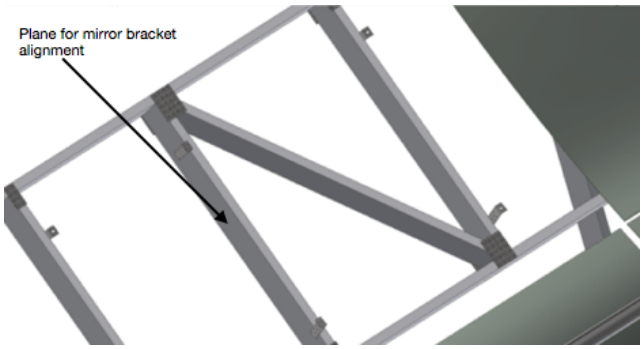

Figure 3-42. Position of mirror brackets

3.3 LABORATORY MODEL VALIDATION

We validated the structural computer model using a physical model. Due to time and space limitations, this physical model is somewhat different from the actual collector. However, the physical model was designed so that it contains all relevant components (including the mirrors) of the actual prototype in full scale.

The idea is to obtain the necessary parameters to characterize our developed model and assess its ability in predicting the slope deviation of the mirror surface. We characterize the state of deformation of the structure and the mirrors before and after a load increment. Measurements on the mirrors are processed to obtain slope deviations while measurements (with an independent loading configuration) on the structure are processed to determine the material parameters.

3.3.1 Design requirements of the validation prototype

The structural design of high precision structures requires a reliable computational model. We validated the predictability of the model. For that purpose, a physical experiment is proposed in which a collector's unit cell is built and tested under different loading configurations so that measured results are compared to analytical estimations. This unit cell is the smallest portion of the collector structure that includes all the components. With prior characterization of each component, a good structural model should predict the observed behavior of the physical model. In this document, we present the design requirements of the physical model.

3.3.1.1 Introduction

In general, structures that support optical devices have strong requirements in terms of their stiffness over the lifetime. Minimal structural deformations can completely destroy the optical performance. Thus, it is important to accurately characterize the mechanical behavior of those structures. For the development of the Green Parabolic Through Collector (GPTC), a sophisticated structural-optical numerical model was developed such that the optical performance is simulated for different loading scenarios. This model account for the measured stiffness of each structural member and connection to estimate the deformed shape of the optical surface. Several component tests were performed on components (including nail plated joints, screw joints, wood members etc.). The data obtained from these experiments were used in Monte Carlo simulation of the collector. However, the accuracy of the structural model needs to be validated. We are interested in assessing the ability of the structural model in predicting the response given that the component behavior is known.

With the current state of the art in structural engineering, experimental methods provide the most reliable mean for analytical model validations. With a validation prototype that consists of a portion of the collector that contains every single component, we build more confidence on our structural simulation. This section outlines the structural and mechanical design requirements of such validation prototype.

3.3.1.2 Concept design

The validation prototype consists of a small portion of the full-scale prototype. The most important design requirement is that it contains all the structural and mechanical components of the full-scale prototype. On the other hand, our purpose is to load the prototype in a way that represent the typical modes of deformations the collector is expected to experience. Thus, it is desirable that the validation prototype resembles the structural topology of the GPTC. Typically, in lab environments, resources (especially time and space) constraints impose limitations on the size of the specimen to be tested. However, the spatially periodic nature of the collector allowed us to build a full-scale unit cell that contains every single component of the collector. Figure 3-43 shows a three-dimensional view of the validation prototype.

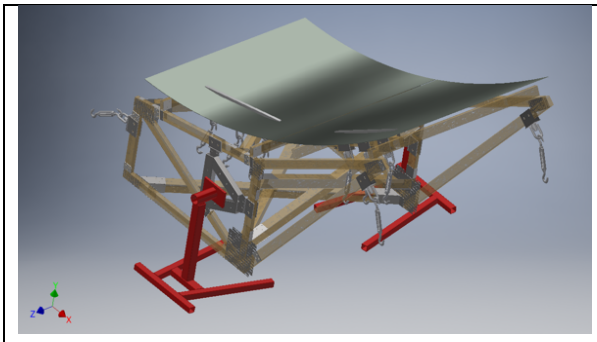

Figure 3-43. Validation prototype

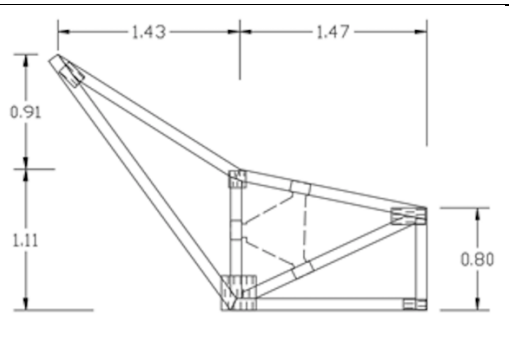

Figure 3-44. Lateral view

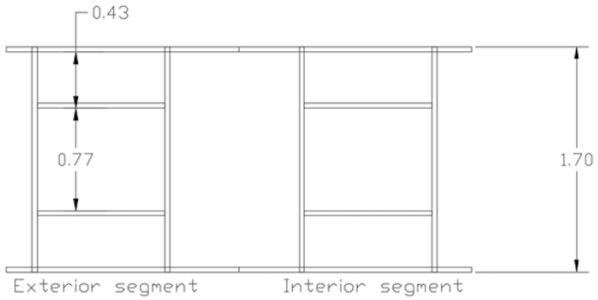

Figure 3-45. Top view

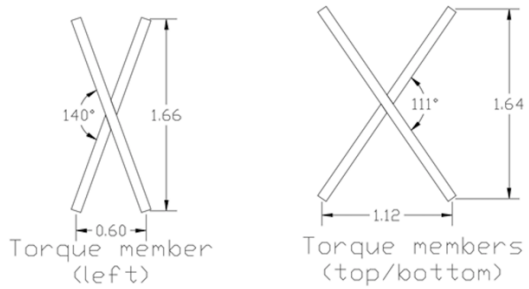

Figure 3-46. Torque resisting elements

The prototype consists of two full-scale half trusses, connected together using the same diagonal (or torque) members used in the actual prototype (as shown in Figure 3-46) to provide torsional stiffness. Mirrors are supported by subassemblies (as shown in Figure 3-45) that sit on top of the trusses. Note that the depth of the torque box is reduced from 1.40 to 0.80m with respect to the actual prototype due to space constraints at Sunvapor's product design testing facility.

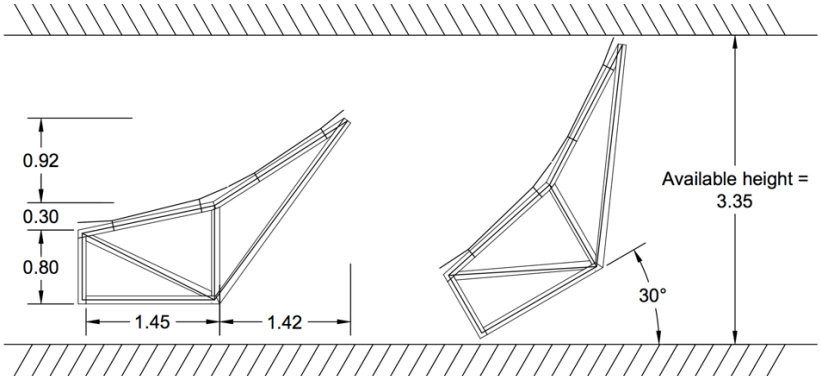

Figure 3-47. Available height and specimen's dimensions

The available height allows for a 30^{o} rotation. On the other hand, enough space is required for assembly work and mirror's measurements. All other dimensions, including members cross section remains the same as the actual prototype. This allows for a straightforward correlation between this validation physical model and the actual prototype.

3.3.1.3 Loading requirements

The loads are to be slowly applied monotonically increasing from a reference configuration (low loads) to the load level specified in Table 3-6. The loading configurations are such that the torque reaction at the supporting pylons is minimized. To achieve that, the system was loaded via displacement control of the loading points. Typically, one side of the structure was restrained while vertical displacement was imposed at the other side. We defined loading scenarios based on two main modes of deformation: Splay and torsional modes. We consider that these modes are sufficiently independent and the most relevant (based on the simulated behavior of the collector structure) ones for the purpose of validating the structural model. Loading points are

classified respect to the purpose of loading (parameter determination marked with a square and actual experiment marked with circle). The specific locations of loading points are shown in the following figure. The magnitude of the applied load was estimated after an initial loading test. The basis for the estimation was the required force capable of producing a Root Mean Square norm (RMS) of mirror surface slope deviations of at least 4mrad respect to a reference (i.e. unloaded) configuration. The following figures show the results of a preliminary simulation of the structure for the load magnitude determination. These results are obtained with an initial set of members and joints stiffness parameters based of previous tests conducted at Sunvapor laboratory and published values in literature. Those parameters were used in the structural-optical analysis and design of the actual prototype.

Splay mode	Torsional mode
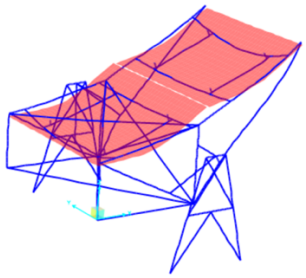	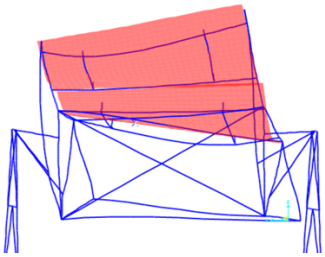
Forces of 0.3kN applied in locations 4 and 8 while restraining 1 and 4 (see Figure 3-49)	Forces of 0.4kN applied in location 8 and restraining of displacements at location 1 (see Figure 3-49)
RMS error = 4.1mrad	RMS error = 4.3mrad

Figure 3-48. Estimation of loading magnitude for 4mrad displacements

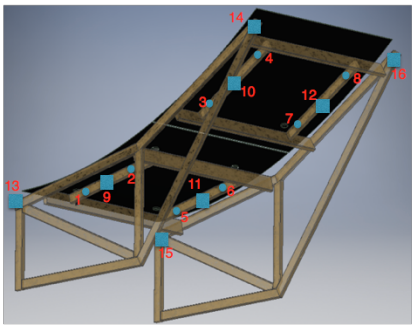

Figure 3-49. Location of loading points

Preliminary analysis suggest that we must be able to impose at least 2kN of loads at each loading points. On the other hand, the support structure needs to be able to withstand a total vertical superimposed force of about 10kN (a very conservative estimate considering 4 loading points subjected to 2.5kN). This imposes a requirement to the minimum load capacity supporting pylons of 5kN. Furthermore, results suggested that no members nor joints should experience failure due to the loads we intend to apply. We considered those estimates to design the necessary hardware for supporting and loading the physical model.

3.3.1.4 Specimen's assembly, mirror alignment and installation

The next photographs summarize the specimen's assembly.

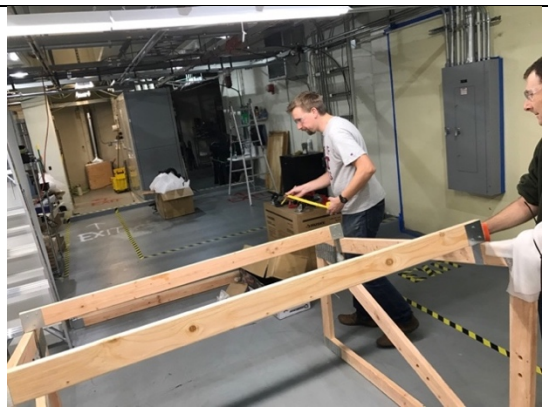	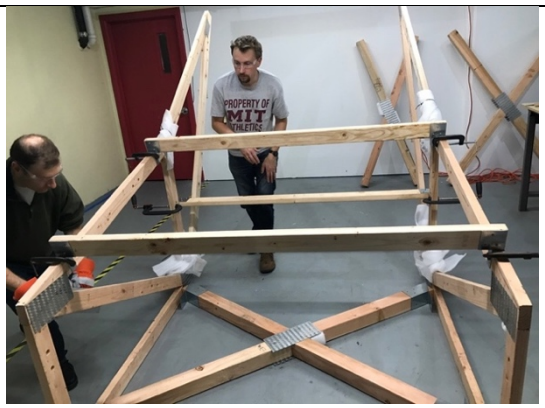
Use of longitudinal rafters to setup truss separation	Placement of lower diagonal cross members

	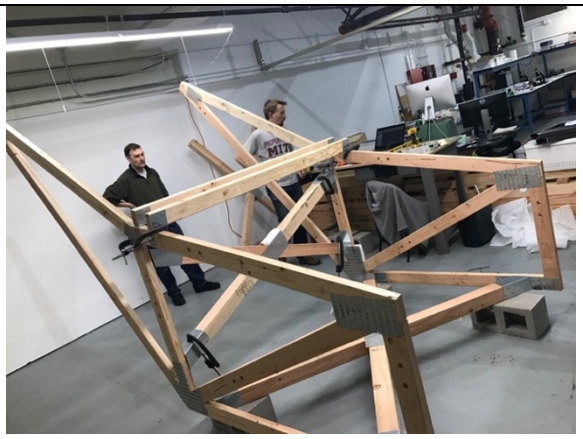
Installation of diagonal members to trusses brackets	Lifting of the specimen to insert screws underneath trusses. Installation of lateral diagonal cross members
	
Installation of top diagonal members	Assembly of mirror mount subassembly.

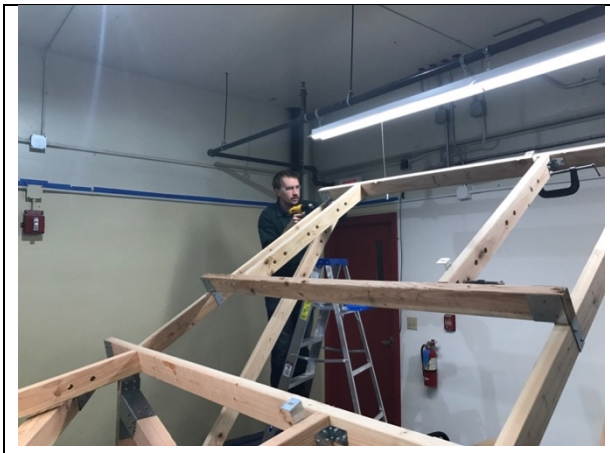	
Installation of mirror mount subassembly	Photograph of the spaceframe

	
Clamping of mirror bracket for adjustments	Alignment of mirror brackets using an alignment rod and laser tracker
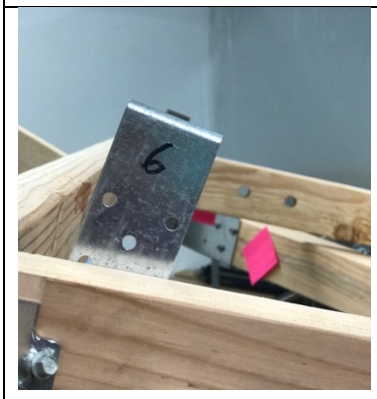	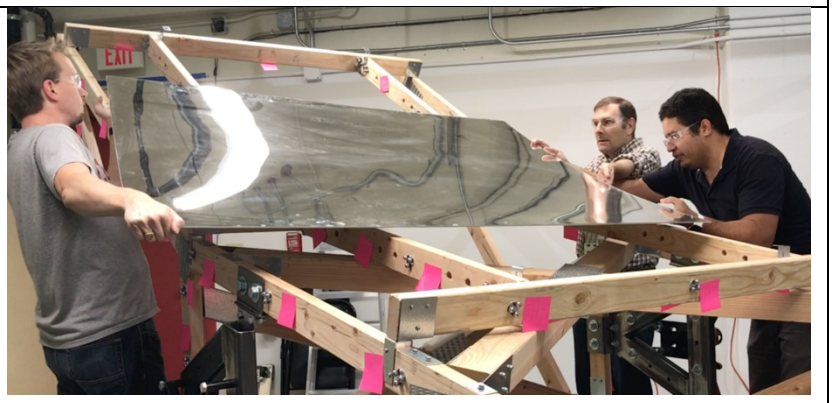
Brackets are attached at their final position	Mirror installation.

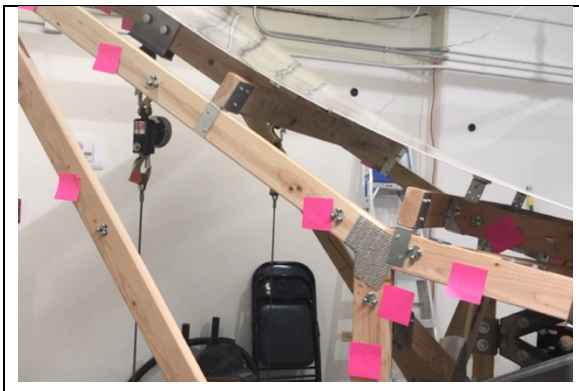

Quality of mirror alignment

Photograph of the specimen

3.3.1.5 Specimen's loading, support and measurements

- *Specimen support*

Figure 3-50. Specimen support

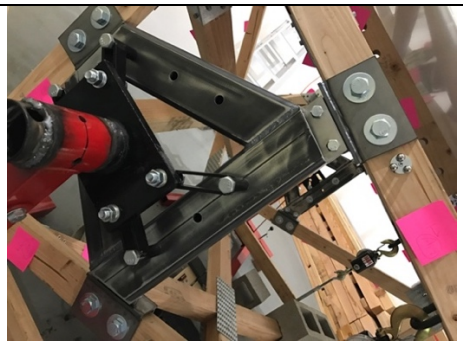

Figure 3-51. Torque plate

- *Force measurements*

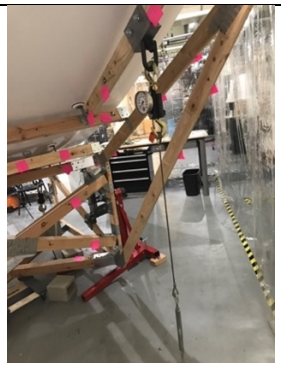

Figure 3-52. Hardware for loading

Figure 3-53. Load measurement

Figure 3-54. Turn buckle for load application

- *Position measurements*

The coordinates of a particular point in the physical model was accurately measured with a laser tracker (Figure 3-55). The tracker obtains the location of the center of a retro-reflector that is held against the object for which position is of our interest (as observed in Figure 3-58).

Figure 3-55. Laser tracker

Figure 3-56. Retro-reflector

Figure 3-57. Three spheres (triads) making a kinematic mount for retro-reflector

Figure 3-58. Position measurements

Kinematic mounts consisting on three spheres (Figure 3-57) were installed in 58 locations throughout the structure to monitor their position before and after the application of a load increment. Each position was measured twice to ensure repeatability of the results. The RMS error for position measurements was always below 30 micrometers.

- *Measurements of mirror slope deviations*

The laser tracker was also used to measure the change in slope of mirror surface. The retro-reflector slides over the mirror surface following a snake-type path. The tracker records the position of a point in the surface every 10mm. Each point is the average of at least six readings providing RMS errors of no more than 200 micrometers. A point cloud is obtained and it is used to determine the orientation of the normal vectors. This is compared to a reference "ideal" configuration consisting of a parabolic shape with the ideal focal distance of RP3. The process is repeated after the application of a load increment. This procedure was observed to provide repeatable and reproducible results (i.e. repeatability and reproducibility less than ~0.1mrad).

Figure 3-59. Mirror slope measurement

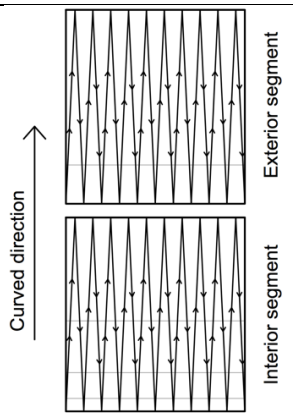

Figure 3-60. "snake path"

3.3.1.6 Physical testing results

Table 3-6 shows the distinct loading configurations applied to the system. There were two main types: Configurations type A and B. Configurations type A serve as the basis for model parameter estimation. Configurations type B are used for model validation. Under each configuration type, two categories are defined: 1 for loads inducing a splay mode of deformation and 2 for loads inducing twisting mode of deformation. For each loading category, we load the system at different load levels (i.e. I, II and III). Significant rigid body rotation was observed for load A1I and A1II. Since the loading was applied by displacement control, we proceeded to enforce displacements at some points (instead of enforcing force conditions) to induce structural deformation (i.e. nonzero energy modes) to the system. Points where displacement was restrained are shaded in Table 3-6. For all analysis, a load level is picked as reference configuration. Table 3-6 indicates the load level selected for reference configuration.

Table 3-6. Loading configurations

Load loc	Loads [kN] Configurations type A (for component characterization)						Load loc	Loads [kN] Configurations type B (for testing)			
	1			2				1		2	
	I	II[b]	III	I[b]	II	III		I[b]	II	I[b]	II
9	0.45	3.6	3.0[a]	0	0	0	1	0	0	0.62[a]	1.25[a]
10	0.45	0.90	0.67	0	0	0	2	0	0	0	
11	0.45	3.6	3.29[a]	0	0	0	3	0	0	0	
12	0.45	0.90	0.67	0	0	0	4	0.53	0.86	0.45	0.80
13	0	0	0	0	0	0	5	0.53[a]	1.25[a]	0.80[a]	1.51[a]
14	0	0	0	0.90	1.80	1.34	6	0	0	0	
15	0	0	0	1.2[a]	2.50[a]	1.87[a]	7	0	0	0	
16	0	0	0	0	0	0	8	0	0	0.45	0.80

[a] shading to indicate that the system was restrained at those locations.

[b] Those conditions are considered reference configurations

After the application of each loading condition, the position of the triads was recorded following the procedure described in the previous section.

Table 3-6 and position measurements of triads suggest that the system had linear elastic behavior for those load magnitudes. The change in position of the triads was used to define displacement vectors at their location. We used finite element interpolation between the position of the triads to obtain a deformed shape of the structure for the two main loading categories. A practical approach to do that was to take a totally unconstrained version of the structural model we developed, and impose the displacement values measured at the location of the triads. This is shown in Figure 3-61.

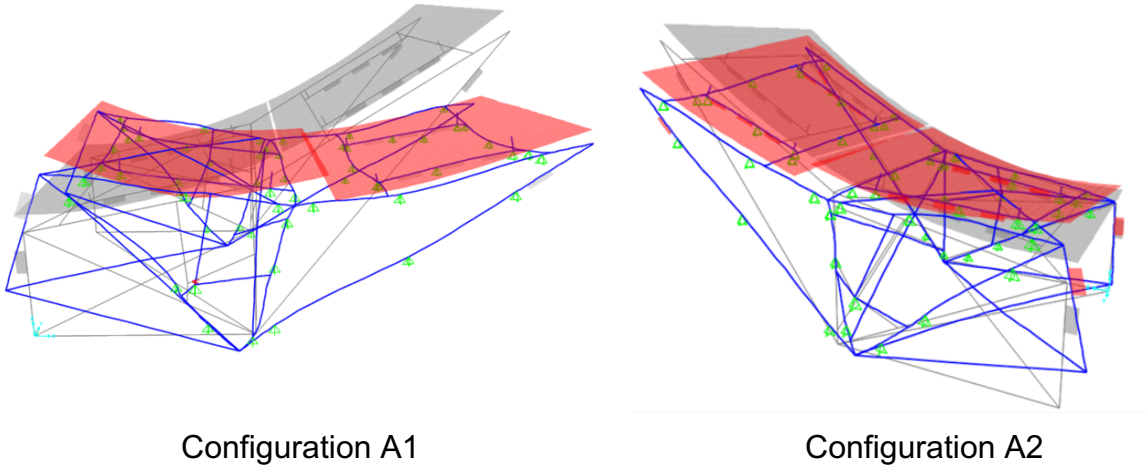

Figure 3-61. Exaggerated deformed shape from triad measurements

Configuration A1 consisted of a combination of rigid body rotation and splay mode of deformation. The flexibility of the mirror support subassembly allowed the rest of the structure to rotate without significant deformation. This basically means that bending stiffness of the mirror mount subassembly was significantly less than the overall stiffness of the frame to splay mode. Configuration A2 consisted of an almost pure torsional mode. Figure 3-61 shows that the triad measurements agree with the qualitative expectation of the deformed configuration of the system.

The rest of the experimental work consisted of loading the system and measuring the change in mirror shape. To measure the mirror surface, we followed the procedure described in previous section. Results of those tests are shown in Figures 3- 36 to 39.

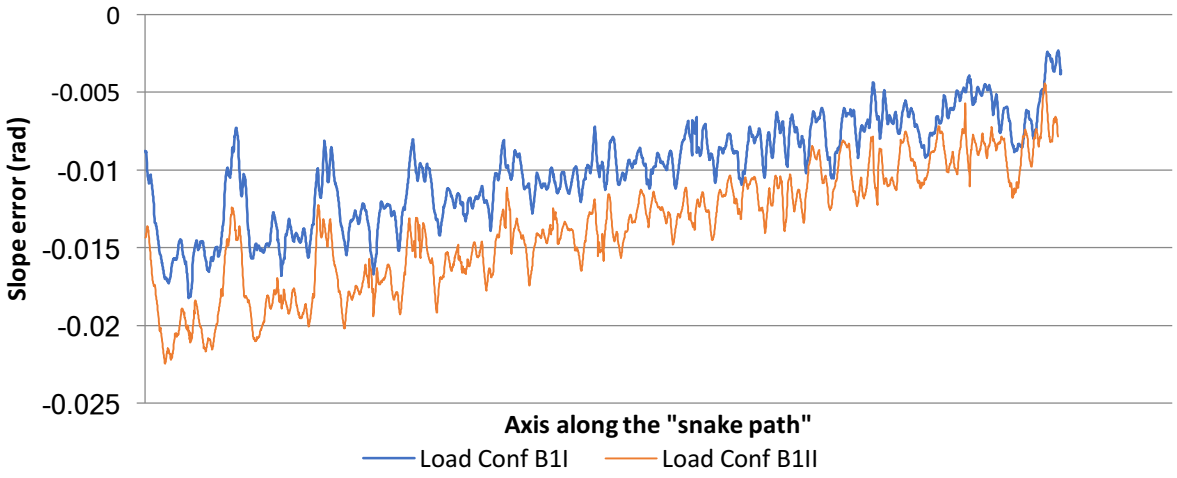

Figure 3-62. Slope error for interior segment relative to "ideal parabola" for load configuration B1

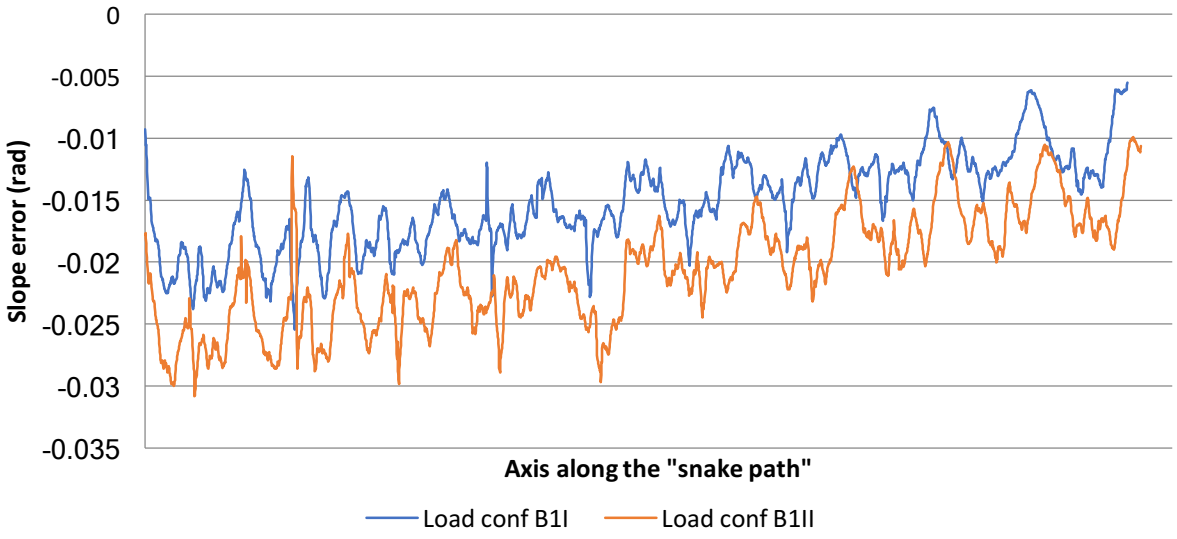

Figure 3-63. Slope error for exterior segment relative to "ideal parabola" for load configuration B1

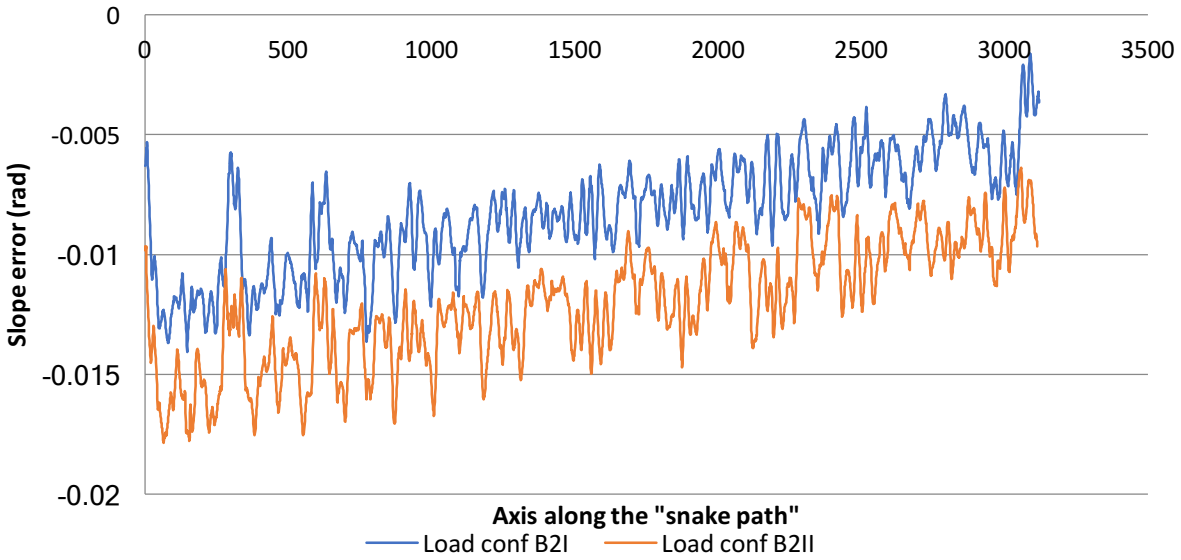

Figure 3-64. Slope error for interior segment relative to "ideal parabola" for load configuration B2

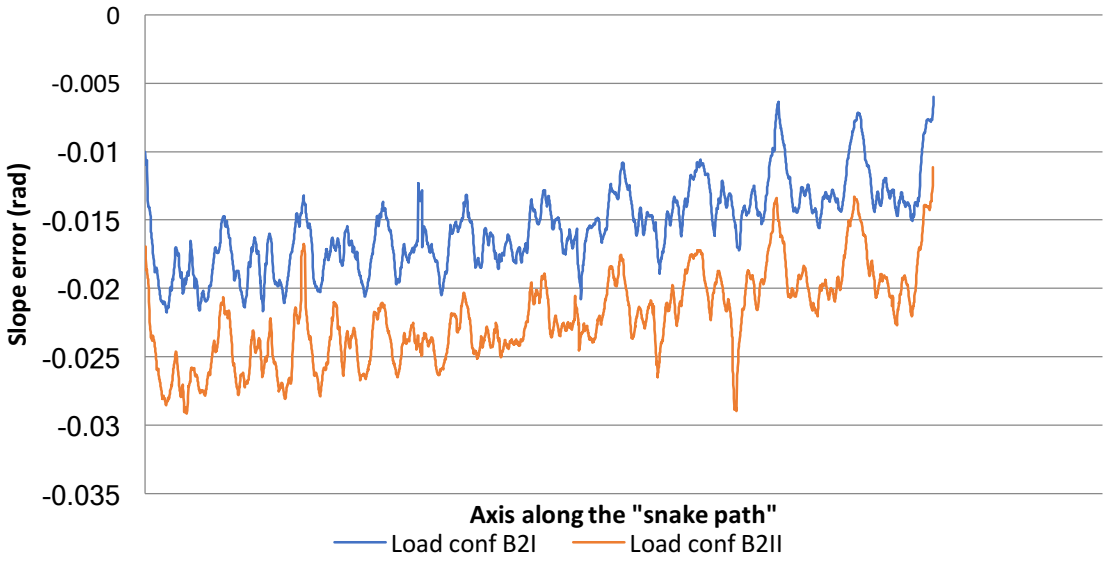

Figure 3-65. Slope error for exterior segment relative to "ideal parabola" for load configuration B2

The slope deviation is characterized by the difference between root mean square (RMS) error of the load level 2 and 1. Two differences are obtained (one for each mirror segment) and the average value is reported as the slope deviation. For load configuration B1 the slope deviation was 0.0046mrad while for load configuration B2 the slope deviation was 0.0051.

Analysis results

Parameters of the structural model were adjusted so that the error in the prediction of the displacements of the triads is less than 1 millimeter. Sensitivity analysis suggested that not all parameters are needed for a confident estimate of the slope deviation of the system. According to the analysis, the parameters needed to reduce the variability of the prediction to less than 0.3mrad standard deviation are limited to the stiffness parameters of the mirror mount sub-assembly (Young's modulus of the members and stiffness of the joints). We calibrate those parameters from the triads measurement. We also measured the Young's modulus of the long truss members. The major change in material parameters was observed for the longer truss members, where the young's modulus was 40% less (i.e. 6GPa instead of 10GPa). The other parameters were within 30% of reported or measured mean values. The deformed shape from the calibrated model is shown in Figure 3-66.

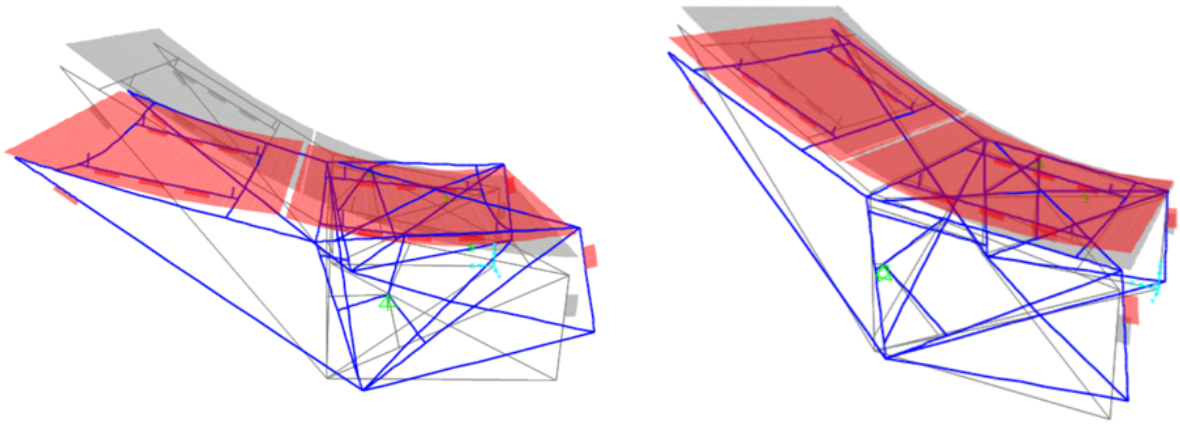

Configuration A1 Configuration A2

Figure 3-66. Exaggerated deformed shape from structural modeling with parameters updated from triads information

Monte Carlo simulations were performed assuming uncertainties of the parameters that are not measured. These simulations are compared with the original Monte Carlo that considered all parameters to be uncertain. The results are shown as frequency distribution of the slope deviation. Figure 3-67 and Figure 3-68 show the comparison of the two simulations and the measured slope error. The error in the predicted value of the slope deviation is shown to be less than 1mrad in all simulations. Furthermore, it is observed that the error is decreased for the simulations with adjusted parameters based on the triad information. In the case of the splay mode, the uncertainty is considerably reduced as the behavior depend of less non-characterized parameters (i.e. basically depends mostly of truss behavior).

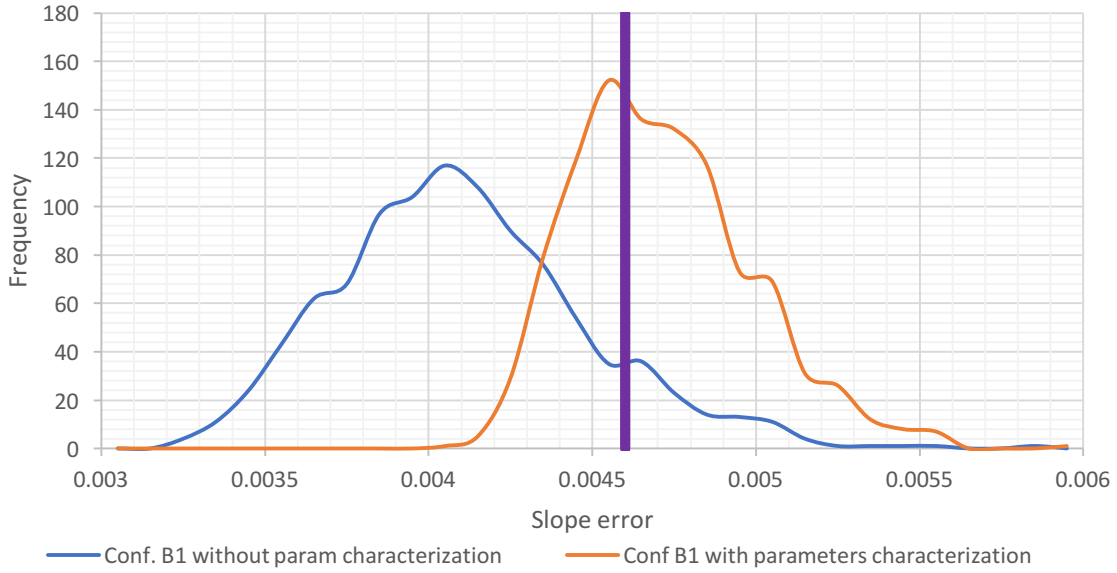

Figure 3-67. Slope error prediction for configuration B1. Comparison between original model with uncertain parameters and revised model with measured parameters.

Figure 3-68. Slope error prediction for configuration B2. Comparison between original model with uncertain parameters and revised model with measured parameters.

3.4 COLLECTOR ASSEMBLY AND CONSTRUCTION

3.4.1 Component fabrication and painting

Components for spaceframe assembly were ordered for fabrication at a truss manufacturing facility off- site. The following figure summarizes all components we received for one spaceframe. The spaceframe consists of the assembly of three type of components: Splay resisting components (SRC), Torsion resisting component (TRC) and Mirror mount elements.

Cpt #	Description	image	Quantity
1	Bottom support and spacer for collector assembly	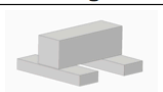	8
2	SRC		4
3	Bottom TRC		3
4	Side TRC		6
5	Top TRC		6
6	Exterior Mirror mount element A		4
7	Exterior Mirror mount element B		2
8	Interior Mirror mount element A	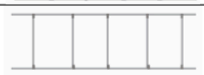	4
9	Interior Mirror mount element B		2
10	ThruLOK screws 9.5”		48
11	ThruLOK screws 6”		44
12	TimberLOK screws 6”		54
13	TimberLOK screws 2”		16

Figure 3-69. Spaceframe parts

Components were delivered to the site and laid out for painting. Figure 3-70 shows spaceframe components prior to painting. Exterior latex paint was applied to the components with a roller for the prototype. In mass production, the components would be assembled from spray painted members to improve painting quality (i.e. by ensuring end grains are properly painted) and labor efficiency. The painted parts are shown prior to assembly in Figure 3-71.

SRC on the ground prior to painting	Mirror mount elements prior to painting
	

Figure 3-70. Spaceframe components prior to painting

SRC in foreground. Mirror mount elements in background	Stacks of painted SRC and mirror mount elements	Painted TRC
		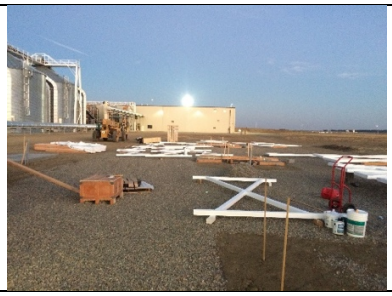

Figure 3-71. Painted components

3.4.2 Civil and electrical work prior to collector assembly and installation

3.4.2.1 Permitting

We obtained a permit from Fresno County to install the solar collector at Horizon Nut in Firebaugh, CA (see Figure 3-72). The permit authorizes Sunvapor to install and operate the collector and related equipment to provide heated air for pistachio drying. The equipment

supplies 174,000 Btu/hour of solar-heated air at a temperature conducive to drying in silos (~ 100°F) and replaces a previously installed propane heater, thereby eliminating its NOx and CO2 emissions.

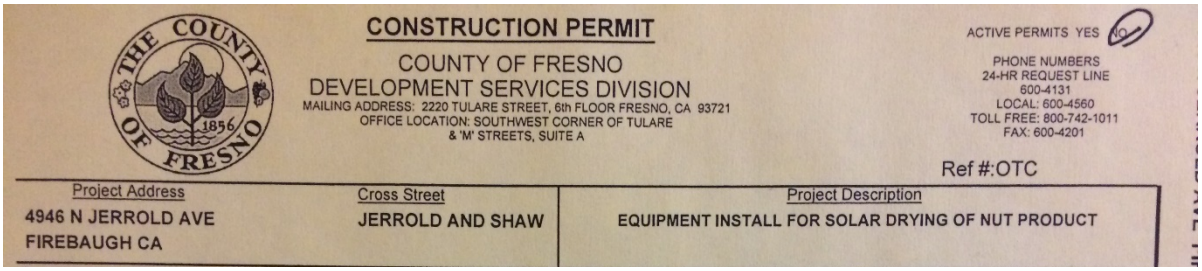

CONSTRUCTION PERMIT

COUNTY OF FRESNO
DEVELOPMENT SERVICES DIVISION
MAILING ADDRESS: 2220 TULARE STREET, 6th FLOOR FRESNO, CA 93721
OFFICE LOCATION: SOUTHWEST CORNER OF TULARE & 'M' STREETS, SUITE A

ACTIVE PERMITS YES

PHONE NUMBERS
24-HR REQUEST LINE
600-4131
LOCAL: 600-4560
TOLL FREE: 800-742-1011
FAX: 600-4201

Ref #:OTC

Project Address	Cross Street	Project Description
4946 N JERROLD AVE FIREBAUGH CA	JERROLD AND SHAW	EQUIPMENT INSTALL FOR SOLAR DRYING OF NUT PRODUCT

Figure 3-72. Permit header

3.4.2.2 Site preparation

The test site is located just south of the row of silos at Horizon Nut. Slight grading was performed to manage water runoff, and gravel was spread on the soil to improved mobility conditions. Trenches for electrical conduit burial per electrical code were dug with machine followed by manual shoveling. These actions are illustrated in Figure 3-73.

Grading	Gravel	Trenching
		

Figure 3-73. Site preparation

3.4.2.3 Electrical work

Electrical service from the on-site 480V distribution panel is being provided to the electrical loads for the project, *viz.* trailer, weather and solar radiation station, main control panel, pumping skid control panel, and slew drive tracking motors. A standby generator with transfer switch is provided so that in case there is an interruption of power resulting in loss of coolant flow, the tracker is able to remove the light from the receiver. The electrical layout is shown in Figure 3-74. Figure 3-75 shows some of the electrical work.

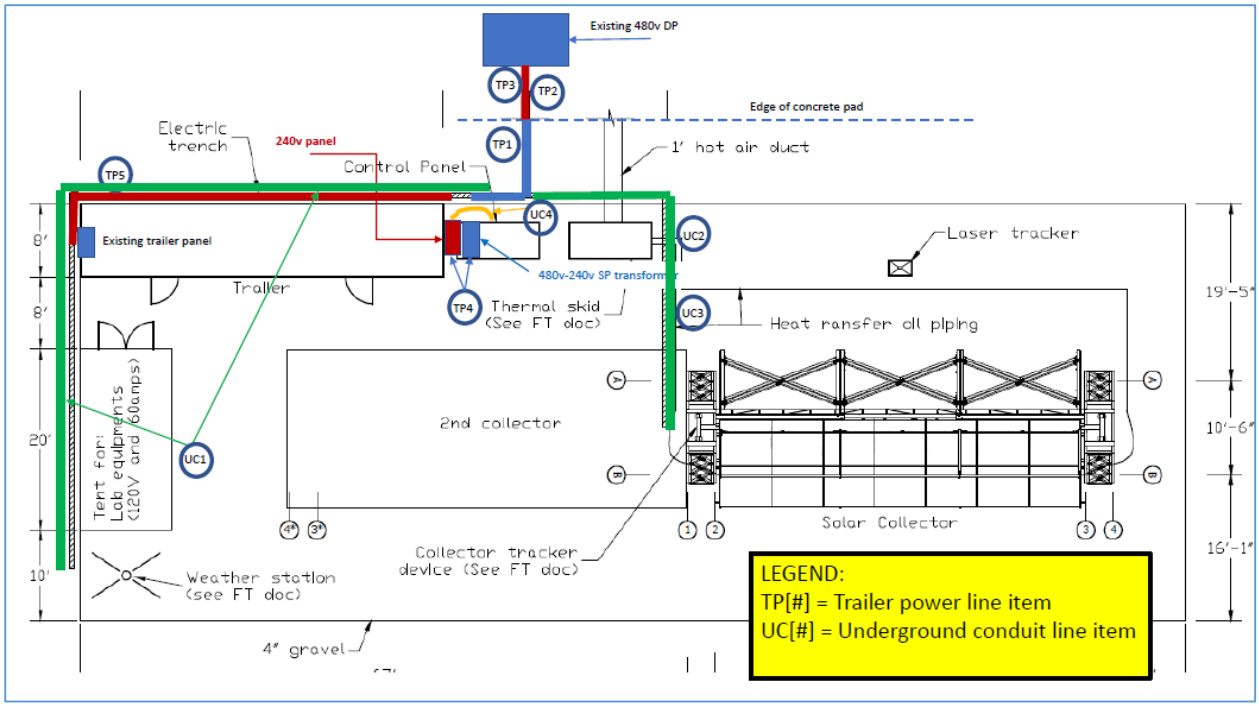

Figure 3-74. Electrical layout

Electric trench	Junction box	Filling trench after electrical work
		

Figure 3-75. Electrical work

3.4.2.4 Foundations

Concrete pads were poured for mounting the 240V transformer, the pumping skid, and the pylons. Originally, we had planned to have a hybrid pile/concrete foundation. Piles without concrete do not provide the (~ 1/8") position accuracy between the large pylon truss pairs that is

required for assembly (Pile position tolerances exceed 1”). Horizontal and vertical pile orientation tolerances are also incompatible with pylon support bracket orientation. The addition of concrete provides a solution to meet the position and orientation requirements for the brackets. We found that for only one collector, it was significantly more cost effective to forego the pile installation altogether and simply pour concrete into a deeper excavation. The freshly poured foundation showing our template for bracket placement is shown in Figure 3-76

Figure 3-76. Concrete pad for pylons

3.4.3 Collector spaceframe assembly

The spaceframe assembly steps were completed as shown in sequence in Figure 3-77. While the first-time assembly process proceeded smoothly, the exercise indicated some minor design and process changes that would speed up the process.

(1) Layout lower diagonals and setting up trusses

(3) Installing top diagonals

(2) Installing side diagonals

(4) Installing mirror mount components

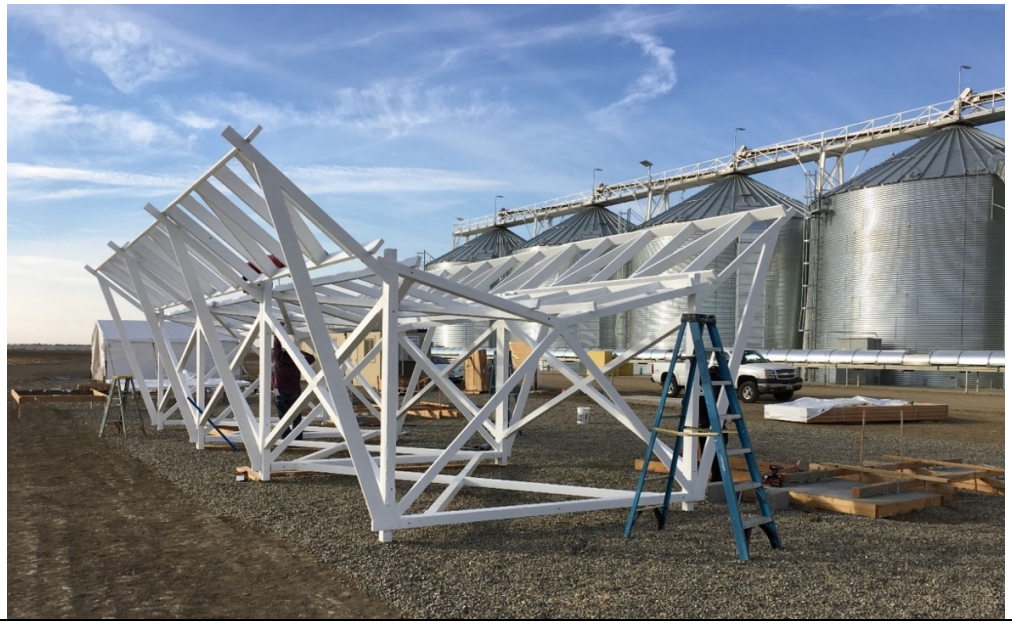

(5) Completed assembly

Figure 3-77. Spaceframe assembly steps

3.4.4 Collector spaceframe assembly time and motion studies

3.4.4.1 Spaceframe components painting

We analyzed the painting process from video recordings. The process was performed with a roller since the paint was being applied to pre-manufactured components as a way to minimize waste. We established a baseline for time to paint by roller, and then applied two productivity improvement factors: (1) using spraying instead of rolling and (2) applying the paint to arrays of cut members instead of subassemblies. It takes 10.7 hrs. for a single person to roller paint all the components of the SCE. An efficiency factor of 3x has been claimed both by our paint contractor and other references, leading to 3.55 hrs. for a single person to spray-paint the SCE. From a worker motion analysis, we estimate a further time savings of a 1/3 by painting an arrangement of individual members (like a deck) instead of subassemblies, with a final labor time of 2.4 hrs./SCE. Assuming a labor rate of \$15/hr., this translates to \$35.7/SCE or \$0.51/m^2.

3.4.4.2 Spaceframe assembly

We analyzed video of the spaceframe assembly and discussed potential efficiency improvements with the contractor. The contractor had never built any spaceframe before and was only given assembly diagrams. They completed the assembly in less than a day that included some rework on a lumber part, re-painting, discussion, and rest breaks. They brought a crew of three with a supervisor who interpreted the diagrams. We recorded that they took one hour to assemble the parts that did not require measuring (*i.e.* all diagonals). They spent some time figuring out how to locate the side diagonals, and how to orient the mirror mount element, and other details that were ambiguous from the drawings. Based on our analysis of the video and discussions of efficiency improvements with the contractor, we assert a likely labor estimate for SCE assembly being even lower than our initial estimates, leading to an assembly cost of as low as $\$1.8/m^2$. (wood spaceframe only)

3.4.5 Support pylons assembly and installation

The pylons assembly and installation take place at the same time as they are assembled in their final location. The following figure shows the three steps.

		
Step 1. Bracket alignment and positioning	Step 2. Pylons front frames are attached to brackets	Step 3. Bracing frames are attached to front frames.

Figure 3-78. Pylons assembly steps

The pylons were enforced to be parallel and also at the right separation by traditional civil construction means. The exact orientation of the pylons relative to east-west was measured so that we account for that for tracking.

3.4.6 End plate attachment

The end plate consists of three rectangular plates joined together by a master plate. The end plate was assembled on the ground as shown in Figure 3-79. Then, the assembly is installed on the spaceframe using bolts and nuts. As it is seen in Figure **3-80**, the end plate assembly is attached ensuring that the assembly is centered with respect to the spaceframe. No tight tolerances are required for this process.

Figure 3-79. End plate assembly

Figure 3-80. End plate on spaceframe

3.4.7 Receiver mount alignment

The receiver mount is divided into two parts. The lower receiver mount is attached to the spaceframe with no tight tolerance. The upper receiver mount is attached to the lower receiver mount using a slotted plate that allow for adjustments to align the receive.

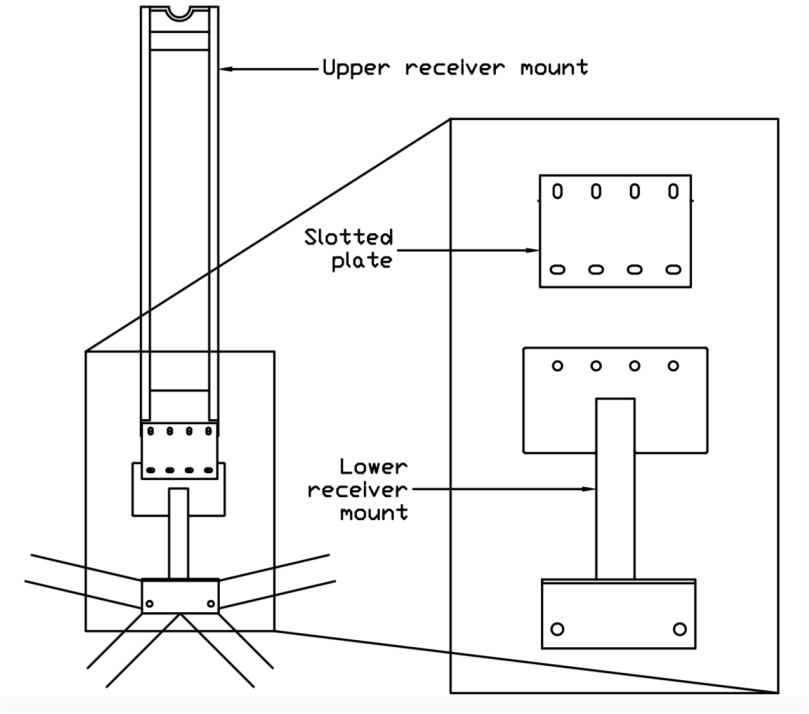

Figure 3-81. Receiver mount

		
Step 1. We used laser tracker to position receiver mounts at each end	Step 2. We connected a feature between the two receiver mounts at each end with a string	Step 3. Use the string to guide the installation of intermediate mounts

Figure 3-82. Receiver mount alignment steps

3.4.8 Bracket attachment and mirror installation

Brackets supporting the mirrors were aligned and fastened to the spaceframe. Mirrors were then installed on the brackets. There are five degrees of freedom that needed to be resolved for each mirror panel. (Translation along axis does not impact optical performance). These degrees of freedom were resolved with bracket alignment and fastening prior to installing the mirrors onto the brackets. Our proprietary bracket alignment process ensures that optical performance will not depend on the quality of spaceframe assembly. This allow us to use traditional framing construction labor to build the spaceframe at a low cost.

	
Raising mirrors into place	Installing mirrors onto brackets

Figure 3-83. Mirror installation

Mirrors are lifted on to the brackets and fastened with four machine screws to mounts in the back. This was carried out primary by three workers with the spaceframe on the ground.

3.4.9 Collector lifting

The collector has been lifted by a crane onto the pylons to enable rotation. The lift was accomplished with a custom spreader bar we engineered from a 14m I-beam. The lifting bar was engineered to lift a total weight of 20 kip which is twice the weight of the collector. The following figure shows the structural idealization used for the analysis and the design of the beam

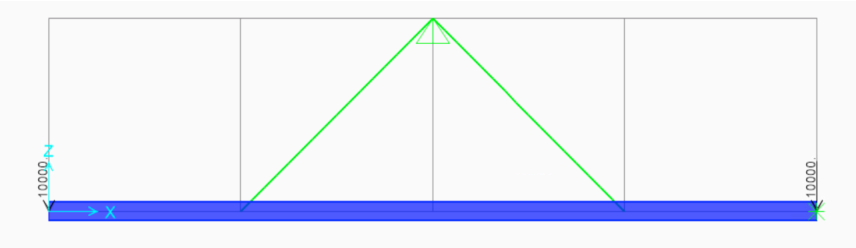

Figure 3-84. Structural idealization of lifting bar

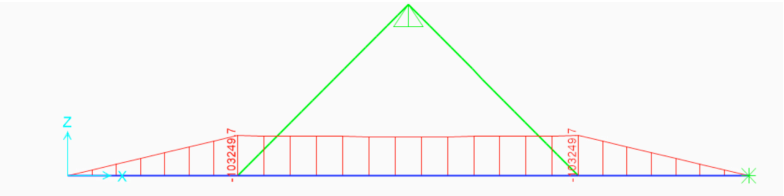

Figure 3-85. Bending moment diagram for the bar

The beam was assumed to be supported by two straps oriented at 45 degrees and that point loads of 10 kips were concentrated at each end. The service moment diagram is shown in Figure 3-85.

The beam was designed so that the axial load and moment interaction (P-M interaction) is such that

$$\frac{P}{P_{cr}} + \left(\frac{M}{M_{cr}}\right)^2 < 1$$

for every material point. The critical values of axial force P_{cr} and bending moment M_{cr} are a function of the material and cross section of the beam. For a W12x65, the maximum demand to capacity ratio was 0.628 as shown in Figure 3-86.

```
STRESS CHECK FORCES & MOMENTS (Combo DSTL1)
    Location          Pu         Mu33        Mu22        Vu2         Vu3         Tu
    10.000       -15836.647 -144549.518       0.000    -909.903       0.000       0.000

PMM DEMAND/CAPACITY RATIO   (H1.3b,H1-2)
    D/C Ratio:   0.628 = 0.093 + 0.535 + 0.000
                       = (Pr/Pc) + (Mr33/Mc33)^2 + (Mr22/Mc22)

AXIAL FORCE & BIAXIAL MOMENT DESIGN   (H1.3b,H1-2)
    Factor              L          K1          K2          B1          B2          Cm
    Major Bending     0.500       1.000       1.000       1.000       1.000       1.000
    Minor Bending     1.000       1.000       1.000       1.000       1.000       1.000

                       Lltb        Kltb          Cb
    LTB               1.000       1.000       1.010

                         Pu     phi*Pnc     phi*Pnt
                      Force    Capacity    Capacity
    Axial        -15836.647  170610.839  859500.017

                         Mu     phi*Mn      phi*Mn
                     Moment    Capacity      No LTB
    Major Moment -144549.518  197681.442  356224.383
    Minor Moment       0.000  160797.949
```

Figure 3-86. Axial load and bending moment interaction check

Figure 3-87 shows the lifting process wherein the spaceframe resting on the ground is strapped to an engineering spreader bar, and a crane moves the ~10,000-pound total load to the pylons. The motor drive and bearings were pre-installed on the pylons using the crane prior to the collector being raised, and once the collector is lowered the connections from collector to the drive and bearing are made at height. The installed collector is shown in Figure 3-88. Only the receiver mounting remains to complete the collector assembly.

Bar attached to collector on ground

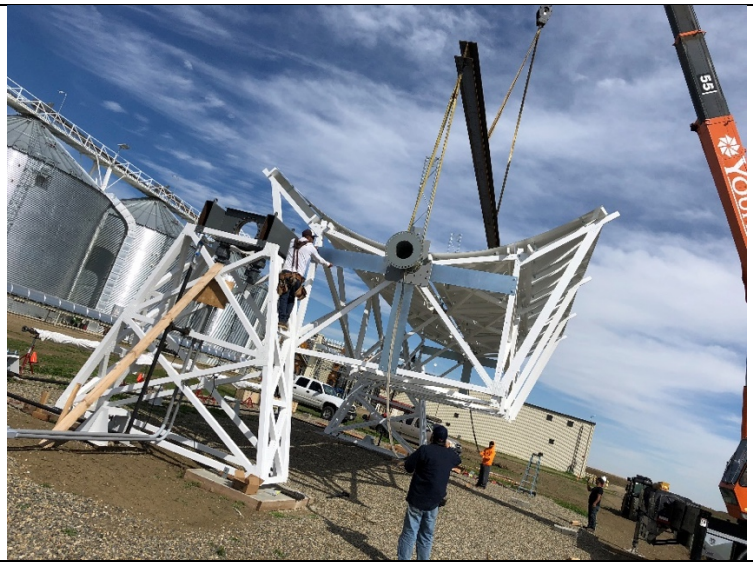

Collector in the process of being lifted

Figure 3-87. Collector lifting process

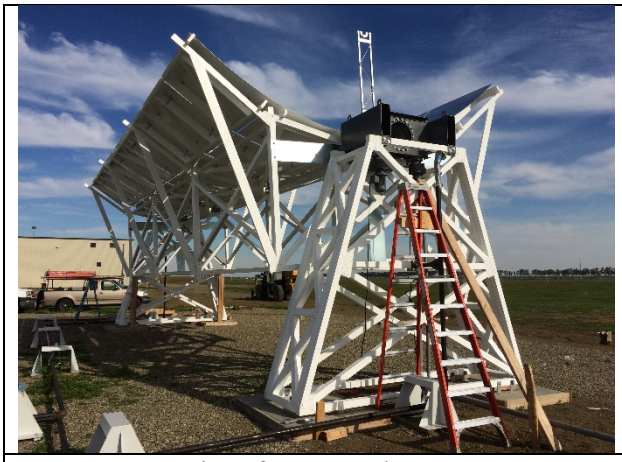

View from Northwest

View from Southeast

Figure 3-88. Lifting complete

3.4.10 Collector tracking control system

3.4.10.1 Control system and panel fabrication

The tracking controls represent part of the Supervisory Control and Data acquisition (SCADA) system developed for the test. The SCADA system has been implemented in a PLC main control panel. A FAT for the main control panel was performed using simulated data for the process. The control panel is accessed through a Human-Machine Interface (HMI). A screenshot of the interface is shown in Figure 3-89. A picture of the inside of the control panel is shown in Figure 3-90. The control panel has been mounted at the site and is ready for electrical integration.

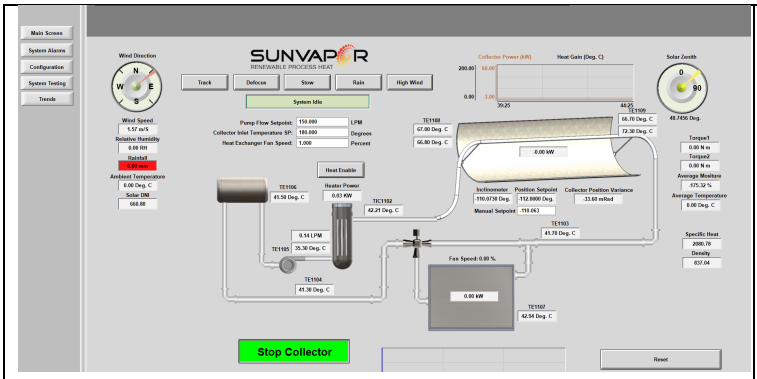

Figure 3-89. Human-Machine Interface

Figure 3-90. Main Control Panel

Tracking is implemented electro-mechanically by two AC motors coupled to a single slewing ring. The motors and slew drive are shown in Figure 3-91.

AC motors

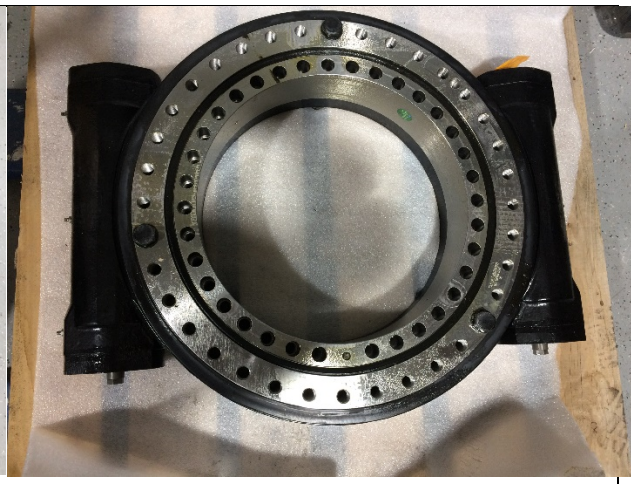

Slewing ring

Figure 3-91. Drive system

3.4.11 Collector rotation test

We performed a first rotation test with the purpose of testing the tracking control system, the collector integrity at different orientations and the functioning of all mechanical components. We monitored motor drive controllers for adequate current and rotation speed. Everything worked as expected. The following is a photograph of the collector pointing towards the south for the first time.

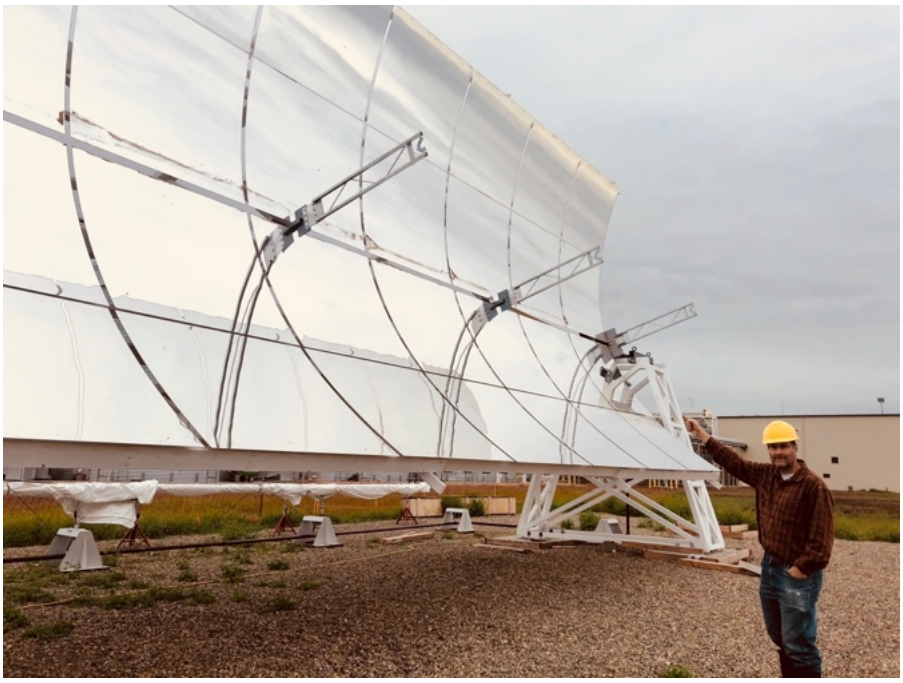

Figure 3-92. Collector first rotation test

3.5 OUTDOOR TESTING

3.5.1 Slope error

3.5.1.1 Method

The shape of the optical surface was measured using a laser tracker. A retroreflector is passed through out the optical surface following a serpentine path, while points are recorded every 10mm. A point cloud is obtained that is then post-processed to estimate the quality of the optical surface. A reference system was defined using sufficiently far apart features of the collector. For the purpose of making acceptable numerical estimation of the slope of the surface at every point, the surface is first discretized by the midpoints of two consecutive measurements in the serpentine path. The derivative at this point is computed using second order central difference approximation.

Since the collector was already installed on pylons and oriented to an arbitrary angle, a self-referencing method for slope error was needed. We adopted a method based on direct raytracing of the measured surface. The method consists of locating the position and orientation of image plane that minimizes the image spot size projected onto the image plane. The optical error at a given location is measured as the angular deviation of the reflected ray relative to the vector connecting the point to the center of the image spot size.

For a given position (characterized by the y-intercept in Figure 3-93) and orientation of the image plane, we are interested in the position of the intersection of reflected light and image plane (i.e. xp1 and yp1 in the figure).

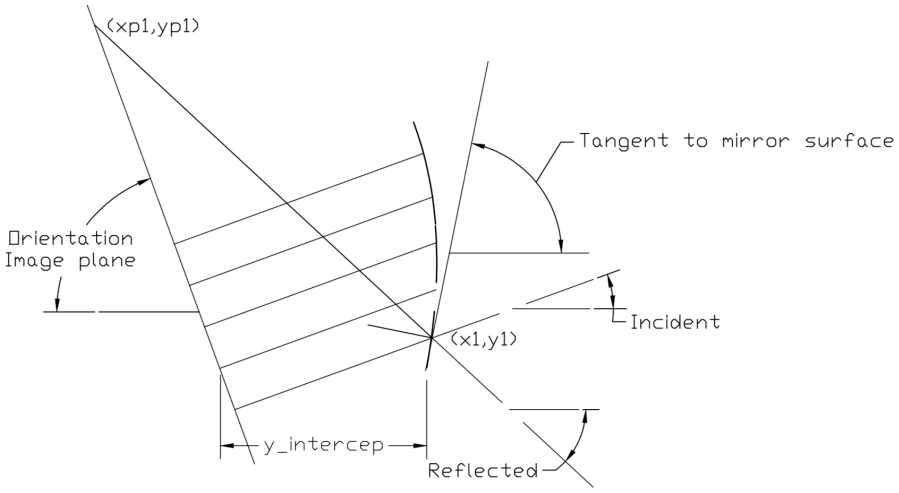

Figure 3-93. Schematics of raytracing problem

For each midpoint, we can characterize the vector of the reflected light and the vector connecting the midpoint and the centroid of all reflected light. Then, the optical error is defined by

$$\phi = \cos^{-1}\left(\frac{v_r \cdot v_c}{|v_r||v_c|}\right) \quad (2)$$

By law of reflection, the surface slope error (θ) is simply

$$\theta = \frac{\phi}{2} \quad (3)$$

Note that since the collector was already installed on pylons, we were unable to scan the whole optical surface in one single orientation. We only scanned the half that we were able to reach while the collector was at stow towards the north (we call this north measurements), then we flipped the collector to the south and scanned the other half (we call this south measurements). The optimal configuration is shown in the following figure.

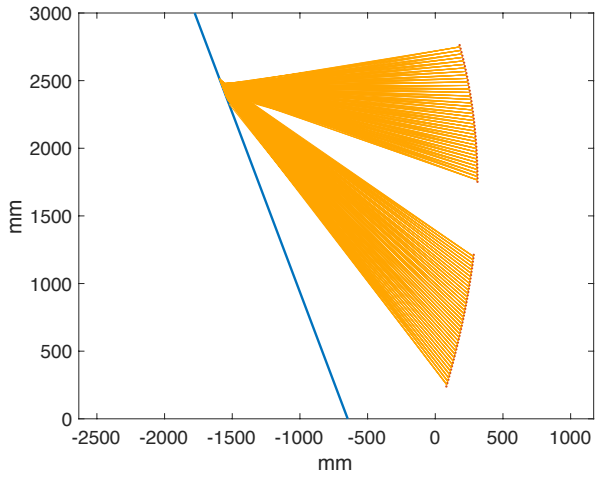

Figure 3-94. Orientation of image plane of 20.653o

3.5.1.2 Results

For the optimal scenario (i.e. y-intercept and image orientation plane that minimize deviation of reflected light), we obtained the relevant quantities shown in the following table

Table 3-7. Slope error results

Data set	Std dev of reflected rays from focus	Slope error
North Inner	12.6mm	4.2mrad
North Outer	12.2mm	2.95mrad
South Inner	14.58	4.9mrad
South Outer	14.11	3.74mrad

3.5.2 Intercept factor

Two methods were used to determine the intercept factor: an indirect thermal method that measures the absolute heat gained in the fluid compared to the solar radiation falling on the collector aperture, and a more direct relative measurement using irradiance targets. The former method has the advantage of integrating over the entire receiver at once but has the significant disadvantages of relying on many inputs with uncertainties, and the accurate measurement of a small temperature rise.

3.5.2.1 Thermal method

- Method description

We circulate a heat transfer oil to cool the collector using a pumping skid and external 2" insulated piping.

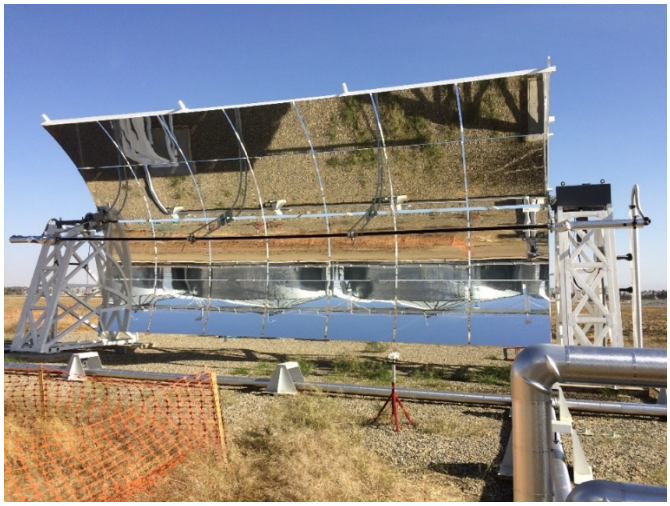

Figure 3-95. Insulated piping and flexible hose connected to collector

The collector tracking was programmed to aim the collector according to the SOLPOS algorithm which predicts the azimuth and elevation of the sun, and an equation that translates position to a rotation about an East-West axis. This collector azimuth was chosen so that the receiver would be fully illuminated by the collector, and this takes place daily at solar noon. The control system is capable of maintaining a constant collector inlet temperature by varying the amount of cooling. We tested the collector efficiency up to 200°C. The process temperature of the fluid at the inlet and outlet of the receiver is measured by immersion RTDs. By measuring the process temperature rise, the fluid flow rate, and the temperature-dependent specific heat, we can determine the heat gain at steady-state. This heat gain is compared with the measured DNI to determine the thermal efficiency of the collector. In the limit of zero heat loss, the thermal and optical efficiencies are the same. For the range of operating temperatures in this testing, the heat losses were shown to be ~ 1% or less.

- Results

The results of the steady-state tests are shown in Figure 3-96 and Figure 3-97 (June 1, 2018) and Figure 3-98 and Figure 3-99 (June 7, 2018)

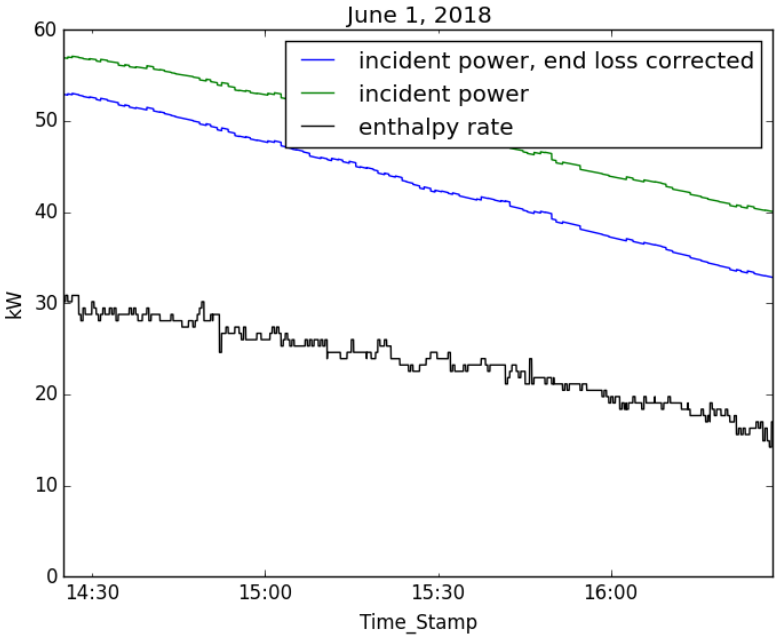

Figure 3-96. Thermal performance (June 1, 2018)

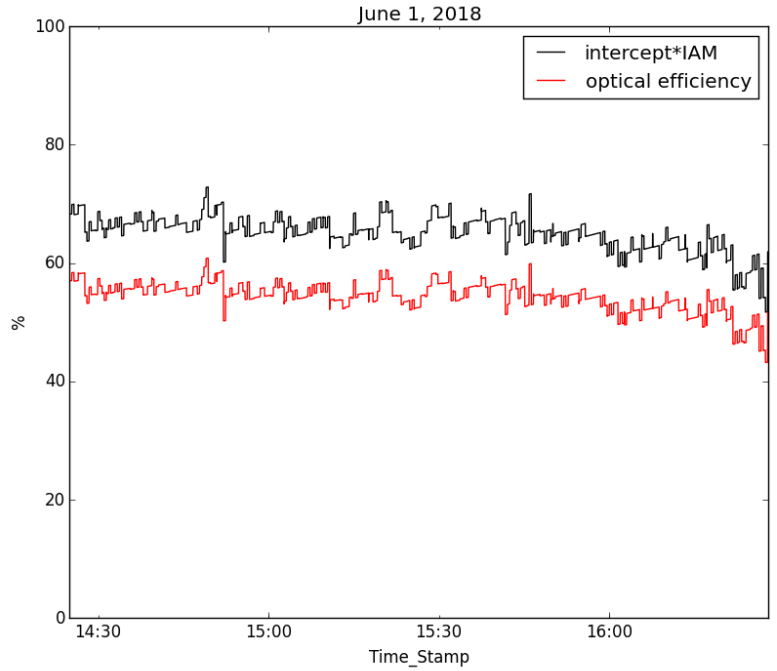

Figure 3-97. Efficiency (June 1, 2018)

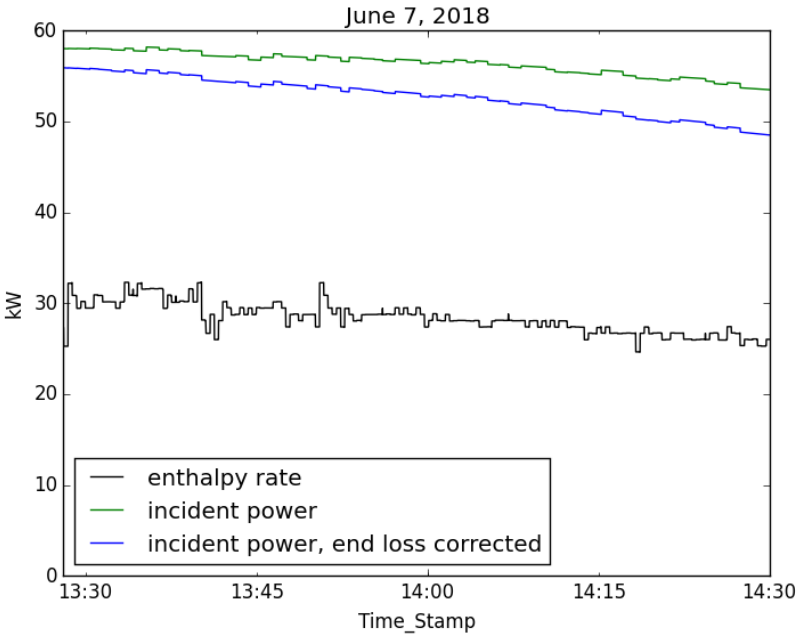

Figure 3-98. Thermal performance (June 7, 2018)

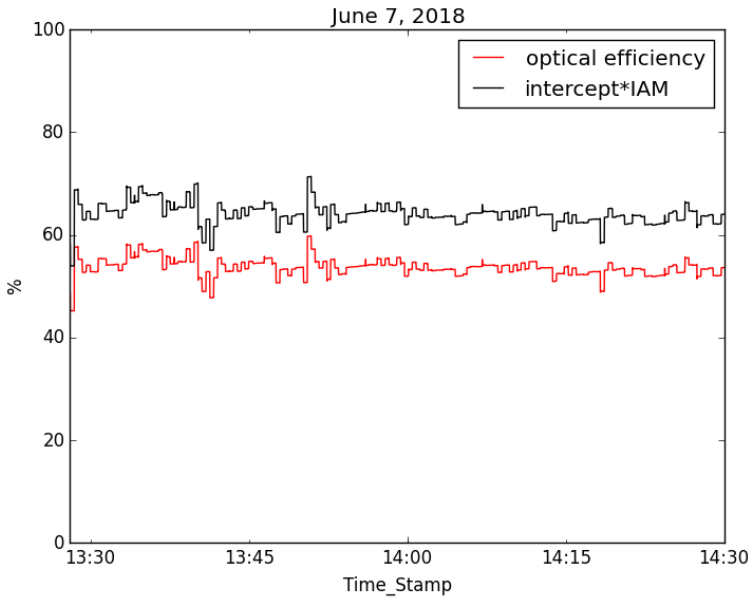

Figure 3-99. Efficiency (June 7, 2018)

At near solar noon we see that the intercept factor uncorrected for soiling or heat loss is ~70% for both days. Using the assumed soiling correction (3% for mirrors, 2% for receiver) we find an intercept factor of 76% for the non-straight tube. Using the 1.09x correction factor for tube straightness we project an intercept of 83% using this thermal method with an uncertainty of 6%.

- Systematic correction due to receiver position and straightness

We detected that due to inadequacy of the design of the lower receiver mount, the receiver moved from its nominal position by up to 40mm. The following photograph shows the misalignment of the receiver.

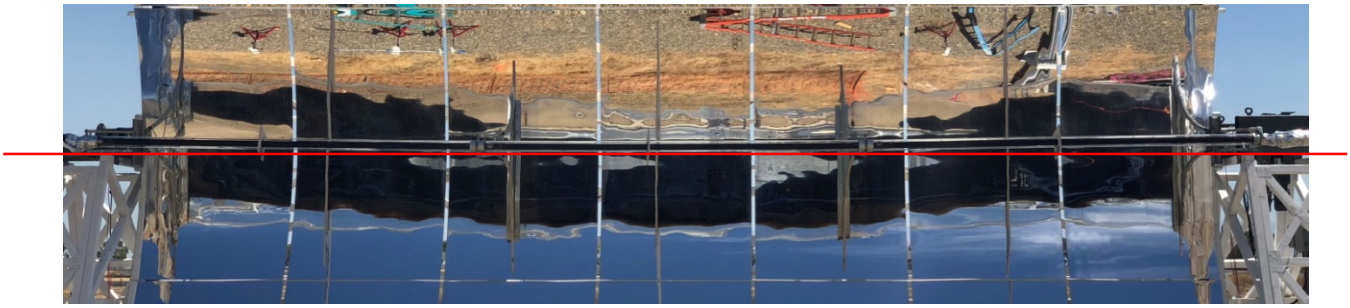

Figure 3-100. Receiver mount misalignment

In addition, the receiver deviates from its nominal position due to a bowing in the focal direction that could be caused by thermal gradient, over-heating and/or excessive lateral restraint of the receiver. The following figure shows simulated deformed shape of a continuous hollow tube steel beam (with properties of receiver tube) subjected to temperature gradients of 300°C/m (which is equivalent to an absolute gradient of 20°C for a 70mm diameter tube).

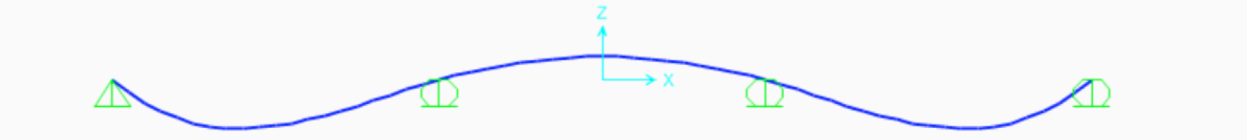

Figure 3-101. Receiver deformed shape when subjected to constant temperature gradient.

A maximum deflection of 3mm is predicted by this model. Based on these two sources, we measured the following profile (red line is nominal profile).

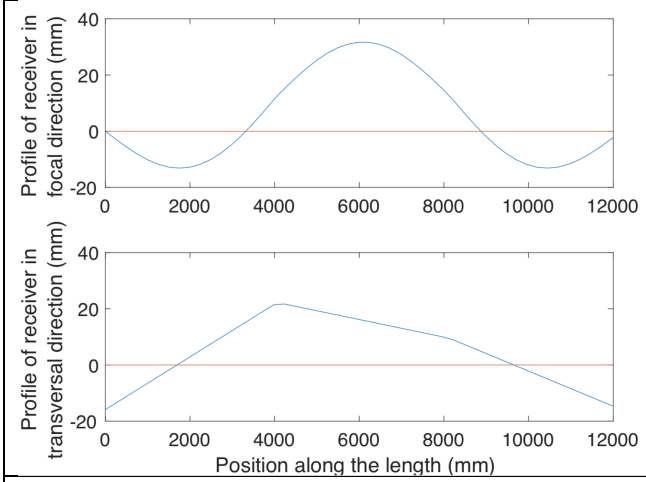

Figure 3-102. Receiver profile

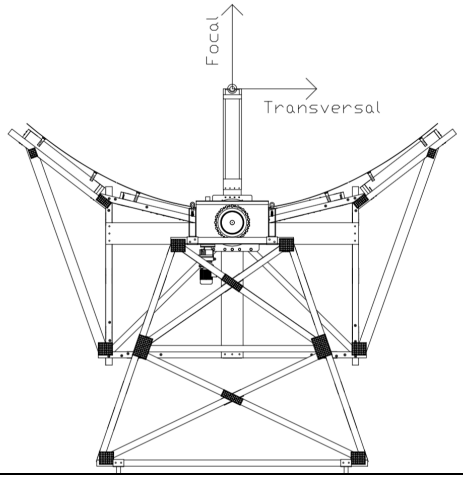

Figure 3-103. Reference system

Where the reference system for receiver position is as shown in Figure 3-103. Intercept factor as a function of receiver position from optical simulation considering perfect optical surface [left] and considering as measured surface [right] is shown in Figure 3-104.

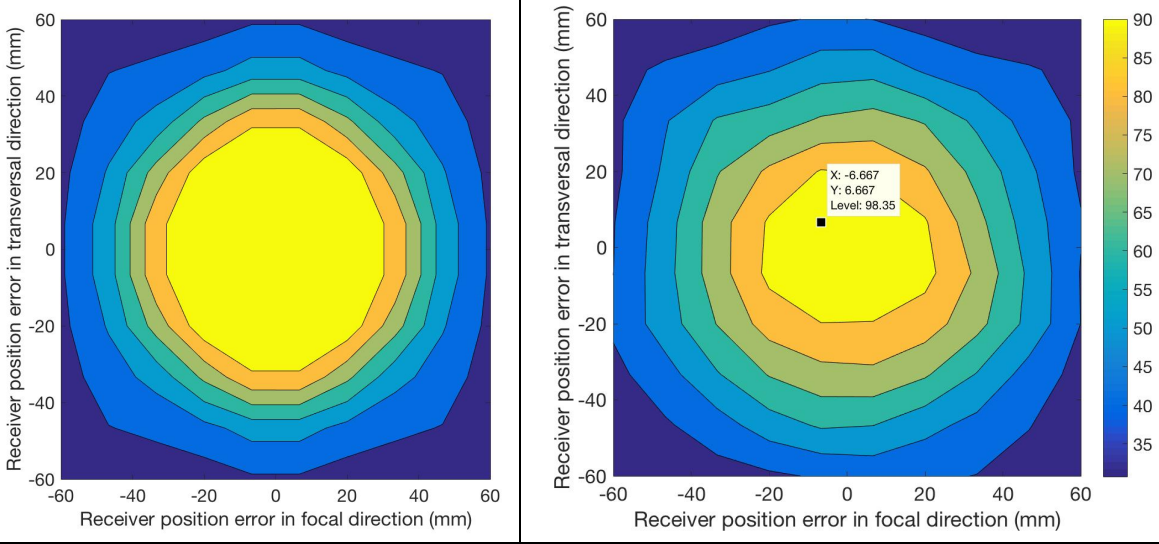

a) Perfect optics

b) Measured optics

Figure 3-104. Intercept factor as a function of receiver position.

It can be seen that intercept factor for perfect receiver position is 98% and very insensitive to receiver position. However, when receiver deviation from nominal is greater than 20mm, intercept factor is greatly affected. An integration of the intercept factor for the profile shown in Figure 3-102 was performed, and an intercept factor of 90.1% was obtained. Then, we define a receiver position correction factor (CF) as

$$CF = \frac{IF_{perfect\ position}}{IF_{Measured\ position}} = \frac{98}{90.1} = 1.088 \quad (4)$$

- -Error analysis

In steady state, the rate of enthalpy in the fluid circulating in the receiver can be expressed as follows:

$$\dot{Q} = DNI\ A \cos(\theta) \eta_O\ IAM(\theta) \eta_{end}(\theta) - \dot{Q}_{loss} \quad (5)$$

Where the first term in the RHS of Equation (5) is the absorbed power. The normal incidence optical efficiency η_O can be expressed in terms of the intercept factor γ:

$$\eta_O = \rho\, \tau_{glass}\, \alpha\, \eta_{bellow}\, \gamma \quad (6)$$

Where the mirror reflectance ρ, the HCE glass transmittance τ_{glass}, and absorber coating absorptance α, and fraction of HCE length comprised by bellows η_{bellow}, are data provided by suppliers. Note that for a mirror in the field, the reflectance will normally be lower than the factory value due to soiling. Soiling also lowers the value of the glass transmittance. We did not independently verify the data provided by the suppliers, nor did we directly measure the impact

of soiling. Instead, we tried various methods of cleaning the mirrors and glass tube. It is reasonable to assume an uncertainty of ρ and τ_{glass} of +0/-3% and +0/-2% respectively. The uncertainties for *clean* ρ, τ_{glass}, and for α are unknown to us, and we do not include them in the analysis.

Returning to Equation (5), we see the DNI on the RHS. The DNI is measured at the site using a Razon+ normal incidence pyrheliometer. The instrument has an uncertainty of 22 W/m2, which, at the levels of DNI we measure, corresponds to ~ 3%. The enthalpy rate is measured according to Equation (7):

$$\dot{Q} = \rho(T_m)\,\dot{V} c_p(T_m)(T_{outlet} - T_{inlet}) \quad (7)$$

Where $\rho(T_m)$ and $c_p(T_m)$ are temperature-dependent density and specific heat, respectively, interpolated at the instantaneous mean fluid temperature from the supplier of the HTF. The uncertainties for the density and specific heat are 1% and 5% respectively. We used a volume flowmeter based on a vortex-shedding principle. This principle has the benefit of being independent of temperature and fluid properties as long as the Reynolds number meets the required condition. For our normal operating flowrate ~ 220 lpm we can expect an uncertainty of flowrate of ~1%. The temperature rise in Equation (7) is measured with a pair of Class A RTDs installed in thermowells, which positions the sensitive element in the center of the 2" pipe on both ends of the receiver. The RTD's have an uncertainty of ± 0.15+ 0.002T, which is ± 0.55°C for each at 200°C. In Equation (7) we are not sensitive to the absolute temperature of the two RTDs, only their difference, and we attempted to remove offset error in the two RTDs in a manner described below. We shield the RTD junction box from concentrated light using a reflective thermal blanket.

From Equations (5)-(7) we see that the intercept factor is a product of independent quantities that have the specified uncertainties and therefore we can apply the propagation of errors formula of Equation (8):

$$\frac{\sigma_\gamma}{\gamma} = \sqrt{\sum_i \left(\frac{\sigma_{X_i}}{X_i}\right)^2} \quad (8)$$

Where each Xi is a variable in the γ product. Inserting the constituent uncertainties $\frac{\sigma_{X_i}}{X_i}$ into Equation (8) yields the uncertainty of the intercept factor, *viz.*, 6%.

Heat loss and temperature offset error

We had originally planned to flow HTF at a rate that would allow a temperature rise of tens of degrees that would allow a very accurate measure of enthalpy given the uncertainty of the RTDs. We found that the bending of the absorber tube became a serious problem that we hypothesized was due to inadequate heat transfer, leading to a significant circumferential temperature gradient for the absorber tube. As a result, we increase the flowrate to levels that reduced the temperature rise to ~4-5°C. Therefore, we pursued a method that would calibrate the offset in temperature *in situ* of the RTDs. In this method, we used electrical heating only and measured $T_{out} - T_{in}$ as a function of T_{in} at steady state. Figure 3-105 shows the different steps in T_{in}, *i.e.*,

{150,155,180,120,60°C}. For these inlet temperatures and a flowrate of 220 lpm, we see very little change (see Figure 3-106) in the ΔT in steady state, with a value ~ -0.45°C. From the supplier test data, we expect the heat loss of the receiver to be 68 W/m at an absorber tube temperature of 250°C. This corresponds to 816 W, which, for a flowrate of 220 lpm leads to a temperature drop of only 0.1°C. As the inlet temperature is <250°C we expect ΔT< 0.1°C, so we take the -0.45°C as an offset error. We measured the temperature of the surface of the absorber tube just outside the glass envelope at the inlet and outlet. It measured within 1° of the fluid temperature. Therefore, we take the an upper bound for the term $\dot{Q}_{loss}$ in Equation (5) to be ~ 1 kW (there will also be some small losses where the receiver is supported). This will be compared with a measurement of the glass temperature below.

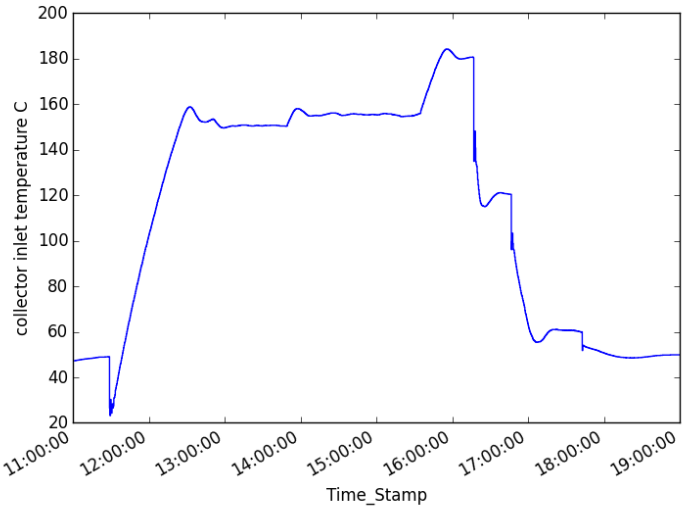

Figure 3-105. Varying the collector inlet temperature on May 24, 2018

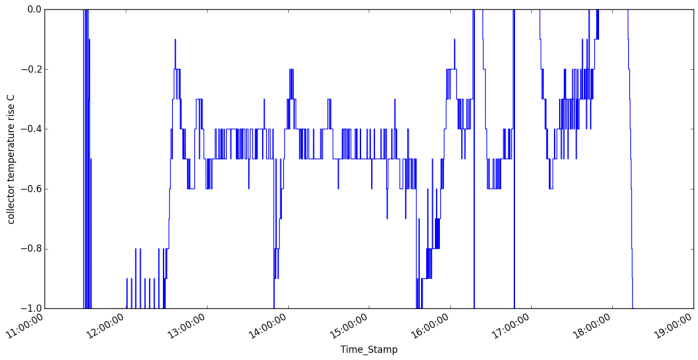

Figure 3-106. Raw difference in RTD readings

DNI and circumsolar

In our predictions of the intercept factor we have used a circumsolar ration (CSR) of 5% which is a typical value for a DNI ~ 900 W/m^2. [16]. If the CSR is higher than this then we would expect a lower intercept factor.

Heat loss verification

We verified the heat loss using a FLIR E60 infrared camera with long focal length lens. The measurement is made with no concentrated sunlight on the receiver. The absorber is heated to 186°C with the fluid which is heated with an electric heater to 190 °C. The ambient temperature was measured to be 24.3°C during the duration of the test. A typical glass measurement of 31.6°C is shown in Figure 3-107 at the location of the reticle. We estimated the heat loss over the receiver from this average temperature using a combination of radiation heat loss and natural convention as there was little wind. For free convention, we use the correlation of Churchill and Chu for a long horizontal cylinder, namely:

$$Nu = \left\{0.6 + \frac{0.387Ra^{1/6}}{\left[1+(0.559/Pr)^{9/16}\right]^{8/27}}\right\}^2 \quad (9)$$

Where Nu is the Nusselt number, Ra is the Rayleigh number, and Pr is the Prandtl number for air. The convection heat transfer coefficient is then:

$$h = \frac{k}{D} Nu \quad (10)$$

where k is the thermal conductivity of air (~2.6e-2 W/mK), D (125 mm) is the outer glass diameter. Therefore, h~ 3.31 W/m2K and the heat loss due to convection over the length of the 12m receiver is 114 W. The heat loss due to radiation from the glass is calculated to be 202 W, for a total heat loss of 316 W with the fluid temperature at 190°C.

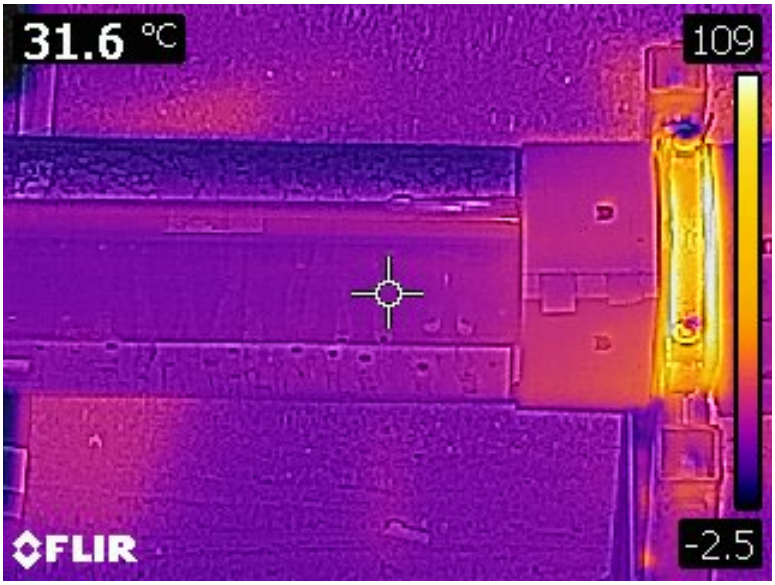

Figure 3-107. Glass temperature reading

3.5.2.2 Optical method

The second method of measuring intercept factor takes the line integral of flux around a target surrounding the absorber tube. This method relies on radiometric image processing, namely background subtraction and linearity, and integration is performed through averaging multiple samples along the length. We use a Canon EOS Rebel SL2 camera with a 24 MP resolution with a 75-300 mm zoom lens. To ensure linearity we store images in RAW RGB format, convert to 16-bit TIFF grayscale, and we perform background subtraction using neighboring pixel values as representative of the background irradiance. An example of the east target with profile (yellow) for integration is shown in Figure 3-108. We fabricated the targets from calcium silicate.

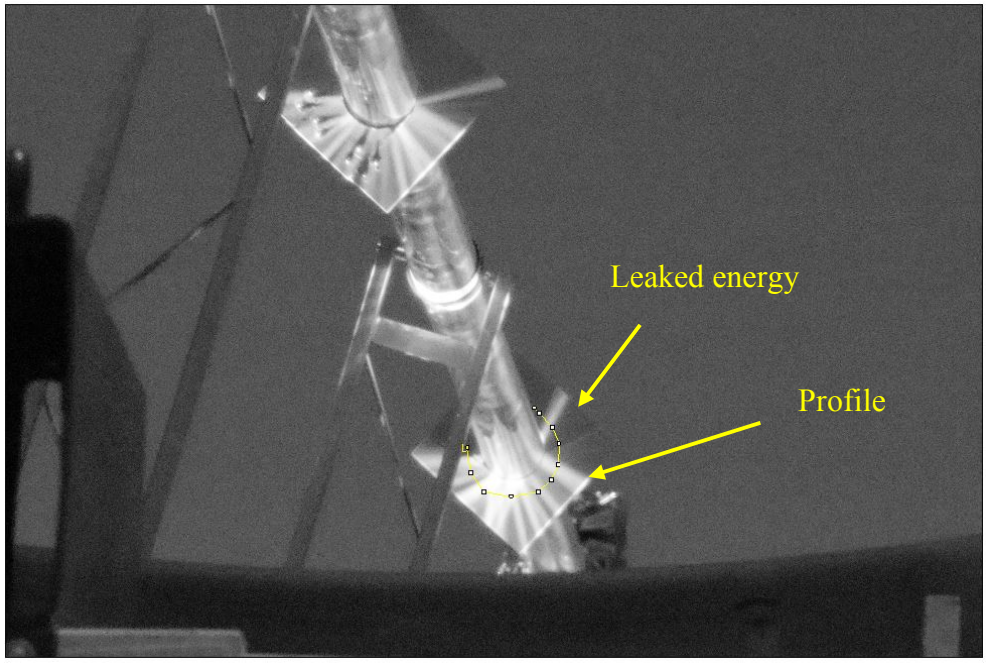

Figure 3-108. Middle and east targets, with profile

Images of three targets located in the center of the west, middle, and east tube were taken through a filtered camera at the same time (see Figure 3-109). Two views of the East target were captured as the complete leakage of light could only be observed from both north and south of the collector axis. From this profile integration method discussed earlier, we find leakage of {5%, 5%, and 23%} for the West, Middle, and East targets respectively, giving an average $\gamma \sim$ 89%. Applying the straightness correction, we project from this method an intercept factor of 97%, which is significantly higher than the 83± 6% value determined from thermal measurements. The camera target method has the advantage over the thermal method of being direct. The thermal method is indirect and involves knowing eleven quantities from measurements, vendor data, or assumptions. Therefore, we have higher confidence in the camera method.

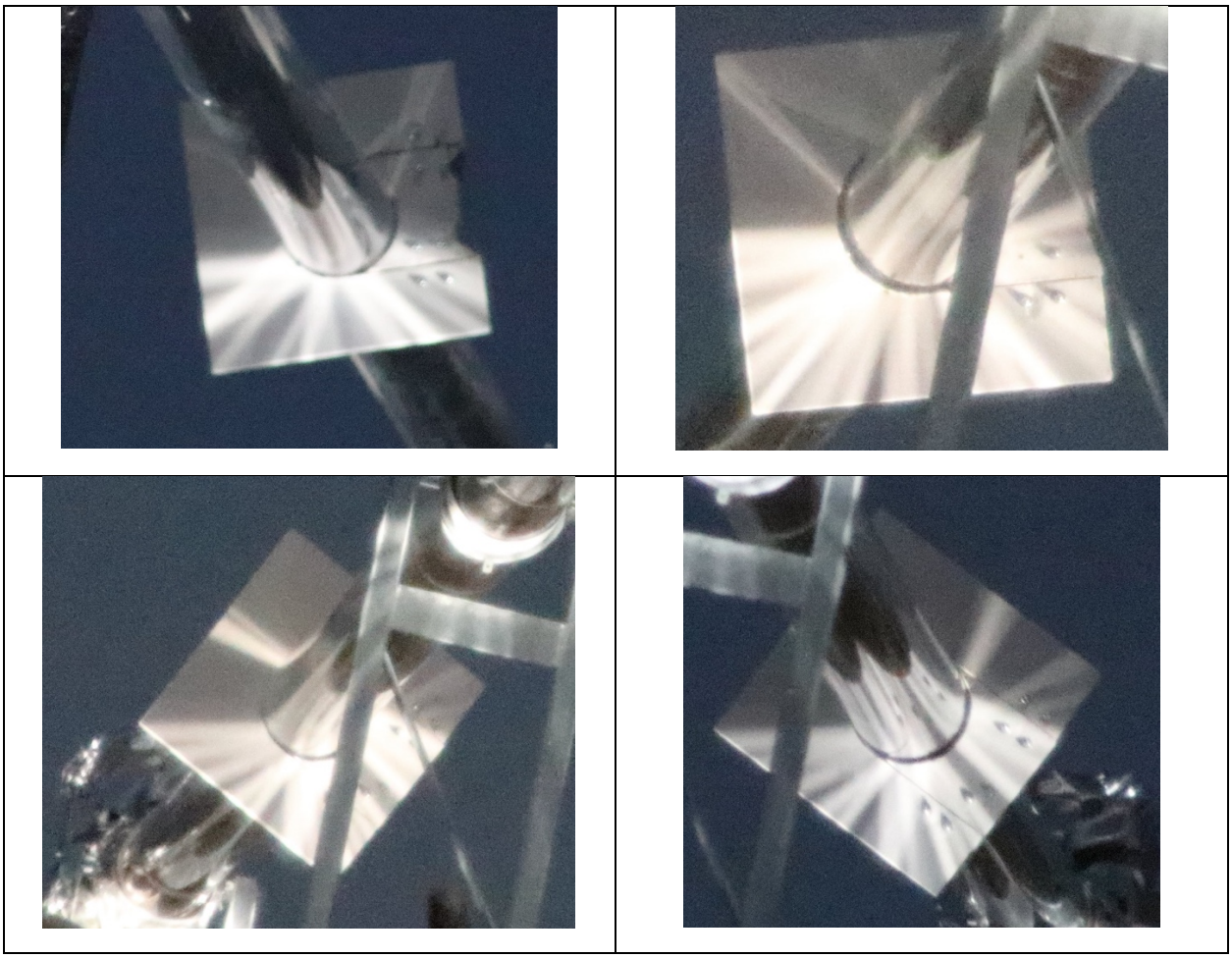

Figure 3-109. Pictures of targets: From upper left, clockwise West, Middle, East from North, East from South

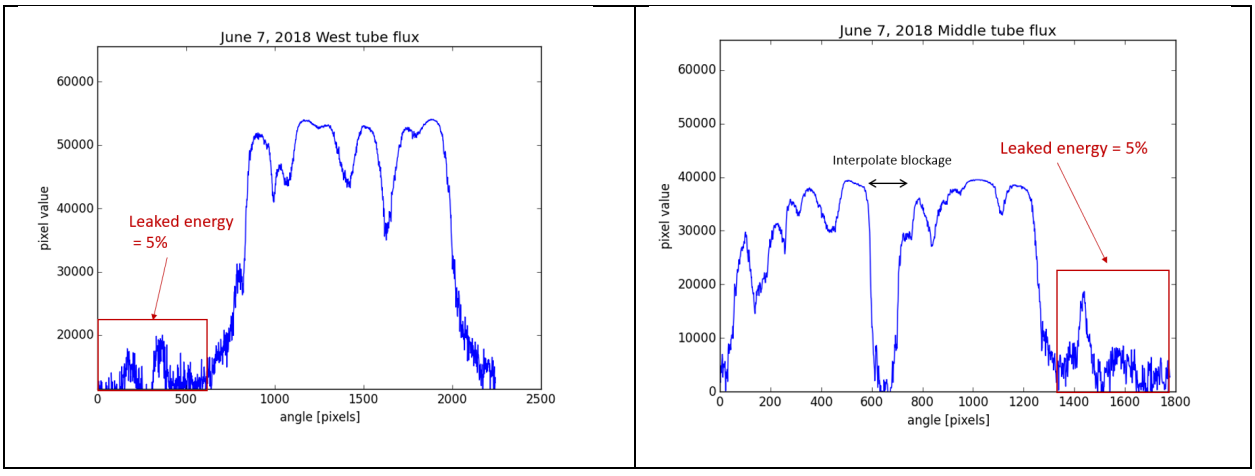

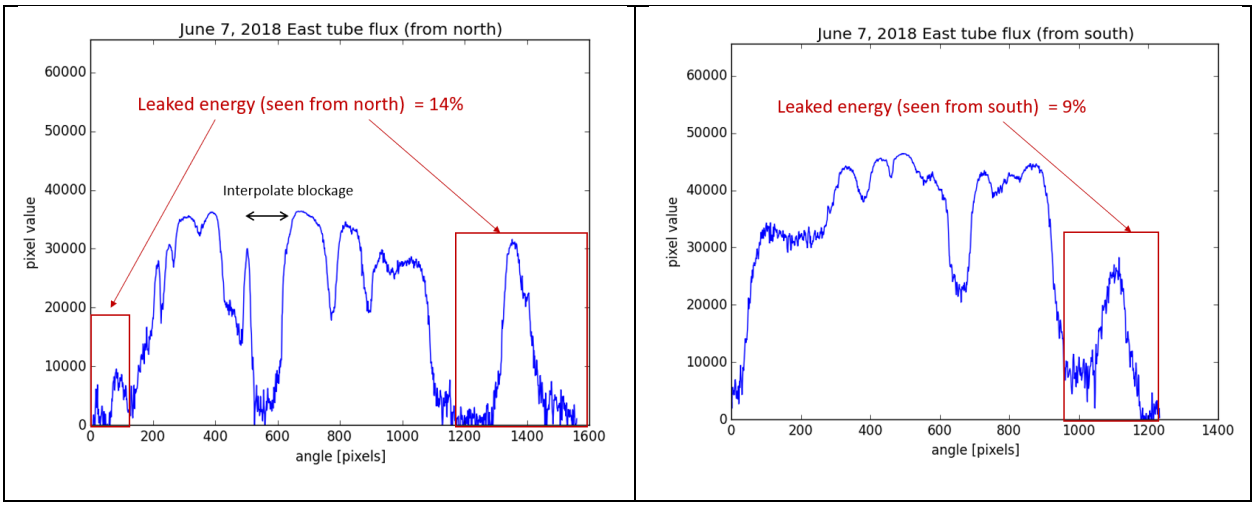

Figure 3-110. Profile data from pictures

3.5.3 Torsional stiffness assessment

3.5.3.1 Background

The solar collector element is one of twelve modules in an array that rotates together to track the position of the sun. Each solar collector element is connected in series forming a long cantilever structure subjected to torque. Note that all other modes of deformation are restrained at each supporting pylon. Since operating wind can induce significant twist to the array, the support structure must be able to provide enough torsional stiffness to maintain adequate optical performance. We measured the torsional stiffness of the as-built collector and used that information to make inferences about the performance of a complete array in high wind.

3.5.3.2 Torque measurement

To characterize the force demand on a collector module, the torsional stiffness, the actuation forces and other relevant quantities, an accurate measurement of the stress resultants at the collector-drive interface is needed. The torque tube connecting the slewing drive to the spaceframe was instrumented using strain gauges. Two rectangular rosettes were used to completely characterize five of the six components of stress resultants (i.e. two shear forces and three moments) and to automatically compensate for temperature. A linear elastic finite element (FE) model of the torque tube was used to obtain the relationships between strain and stress resultants. The FE model was subjected to each stress resultant independently, and the influence on the strain was estimated. Superposition is used to obtain a relationship between strain components and the resultants. Analysis of the strain tensor is done to obtain a direct relationship between stress resultant and the longitudinal strains in the direction of the sensors within the rosette. Then, the relationship is inverted so that we obtain stress resultants as a function of the longitudinal strain from each sensor installed on the torque tube. Given that the longitudinal force in a collector (i.e. the total force along the collector axis) is expected to be small compared

to other components of stress resultants, we don't include it, and instead, we compensate for uniform change in every sensor to isolate the relevant measurements from temperature induced changes in readings.

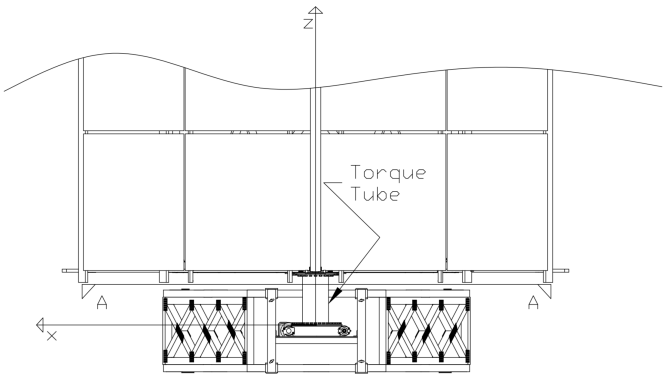

Figure 3-111. Location of Torque tube and definition of reference system

Strain gauges were attached to the torque tube. Three rectangular rosettes were installed in the +y, -x and +x positions. The local orientation of the sensors within the rosettes is shown in Figure 3-113

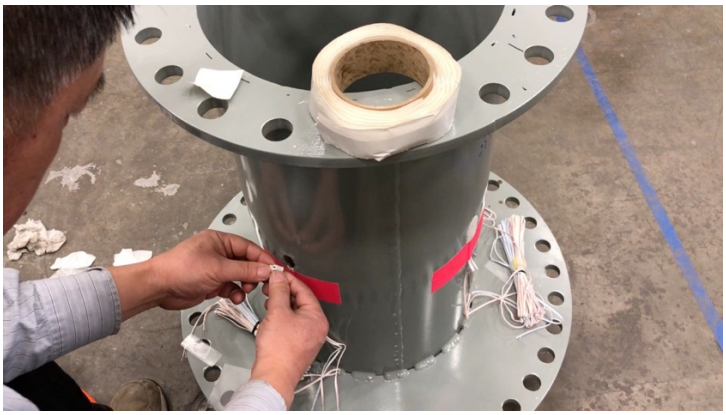

Figure 3-112. Strain gauge installation

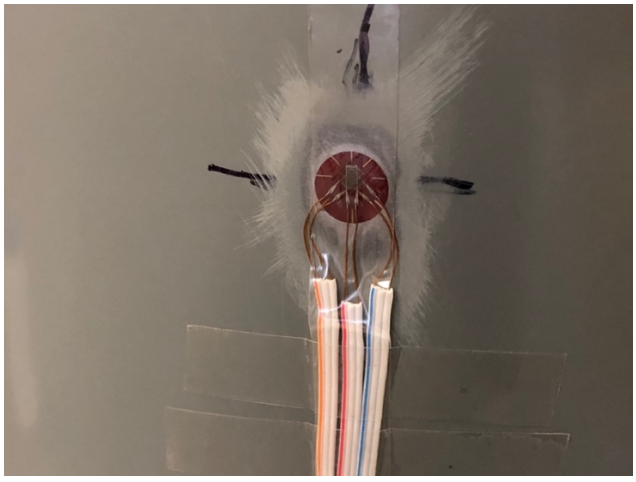

Figure 3-113. Local orientation of sensors within rosette

We identify the local sensor by the color of the wires. Red sensor always acts along the +Z axis. Then, ϵ_{blue}^{-x} is the blue sensor in the rosette located in –x (south) direction when the collector is pointing to zenith.

Finite element simulation of the torque tube

The torque tube was subjected to each of the 6 independent stress resultants (i.e. axial force (P), shear forces in two orthogonal axes along the plane perpendicular to the axial force and moments about three orthogonal axes). The components of the strain were obtained for each of them and shown on a section A-A view (see Figure 3-121) next.

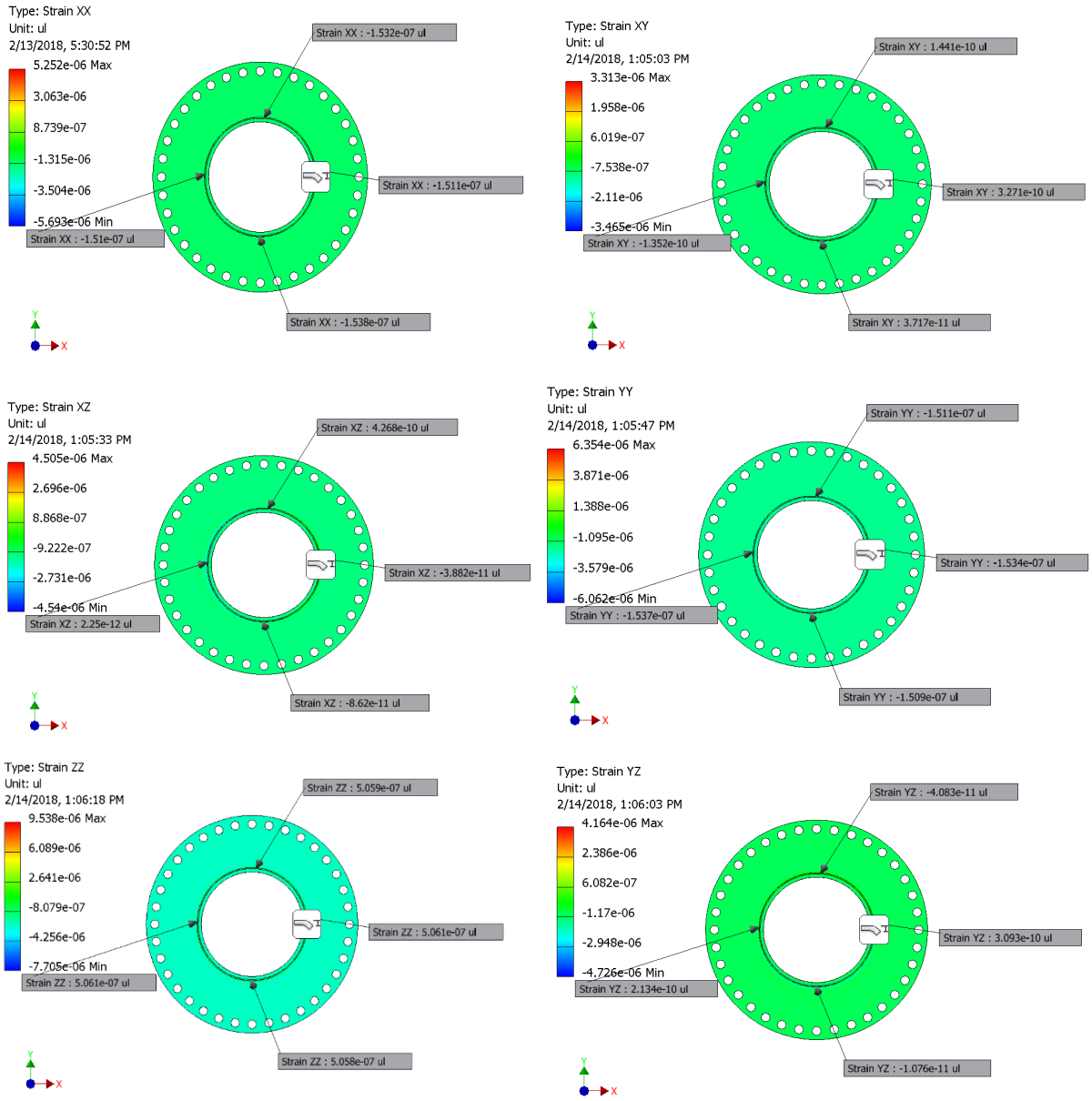

Figure 3-114. Strain contours due to the application of axial load (P) of 1kN

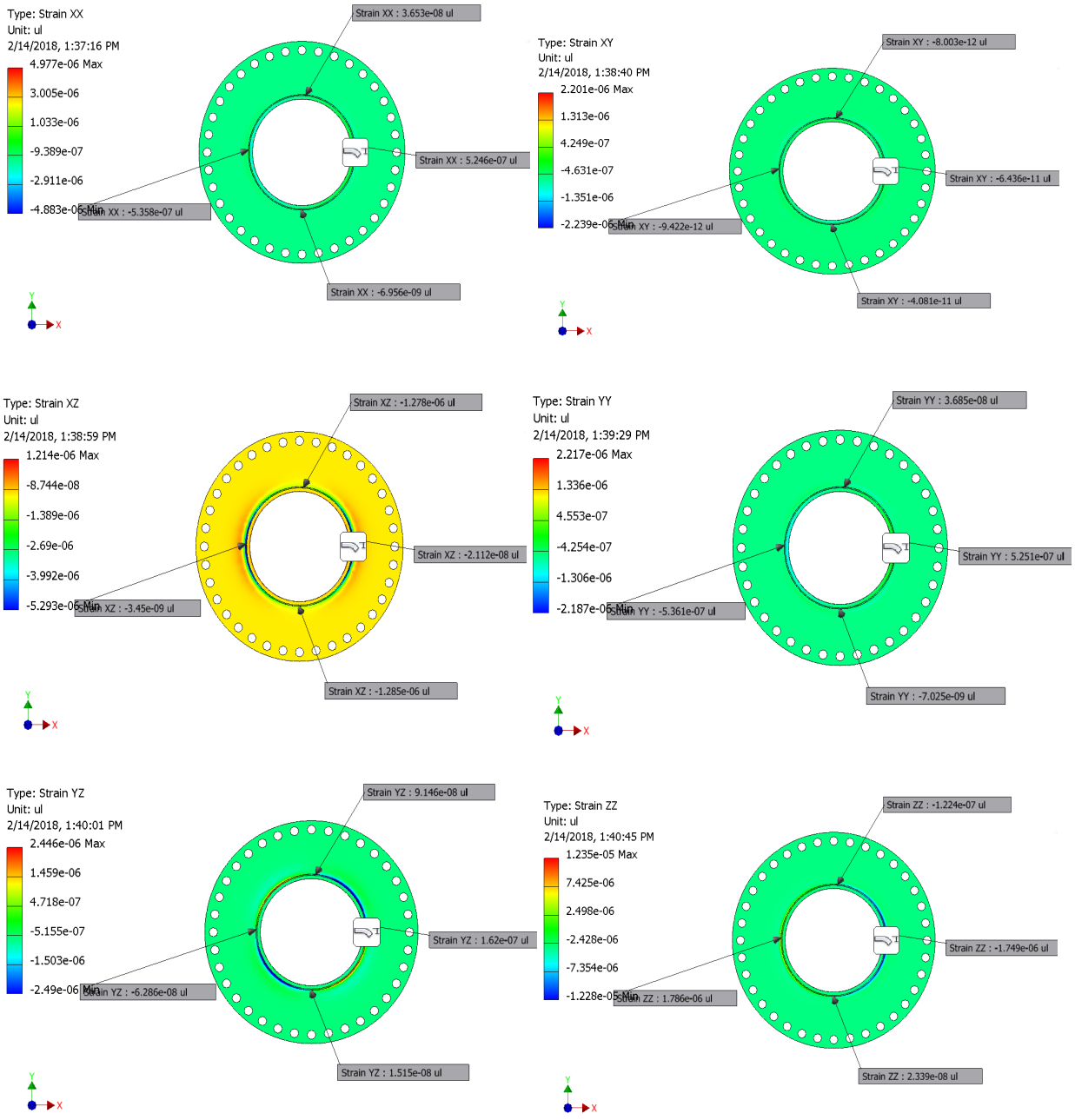

Figure 3-115. Strain contours due to the application of a shear force of 1kN in X-X direction ($\mathbf{S_{xx}}$)

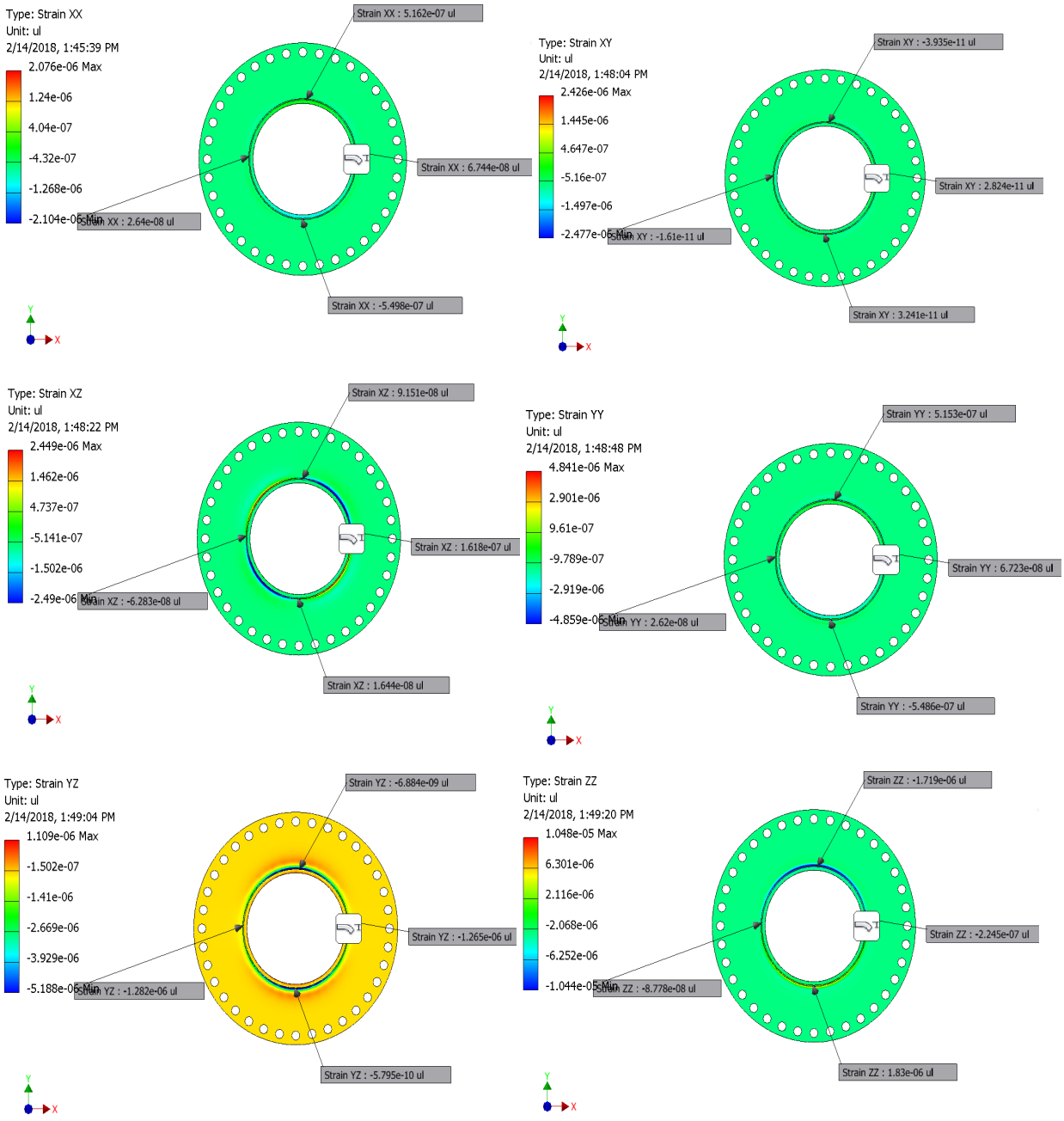

Figure 3-116. Strain contours due to the application of a shear force of 1kN in Y-Y direction ($\mathbf{S_{yy}}$)

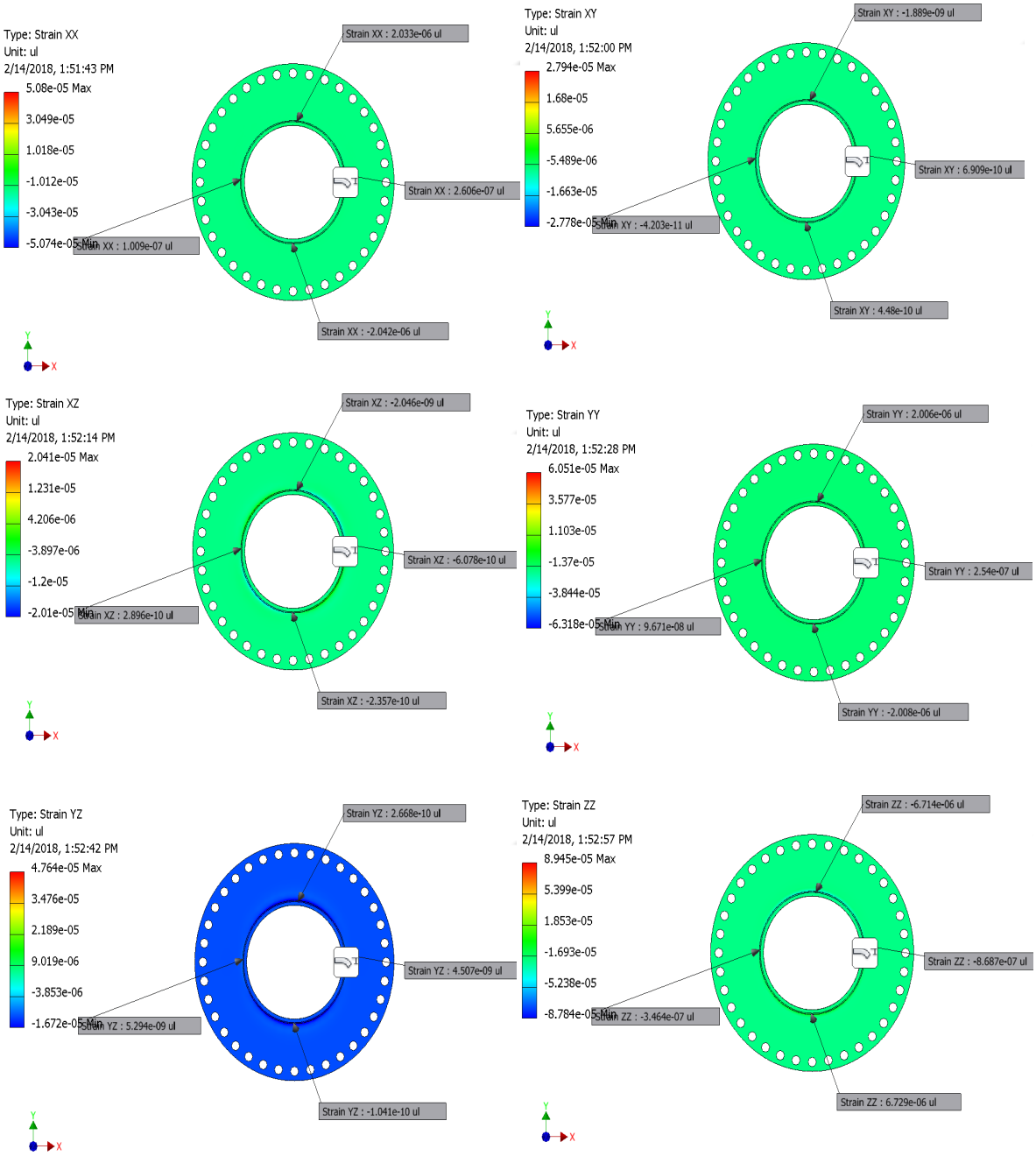

Figure 3-117. Strain contours due to the application of a moment of 1kNm about X-X axis ($\mathbf{M_x}$)

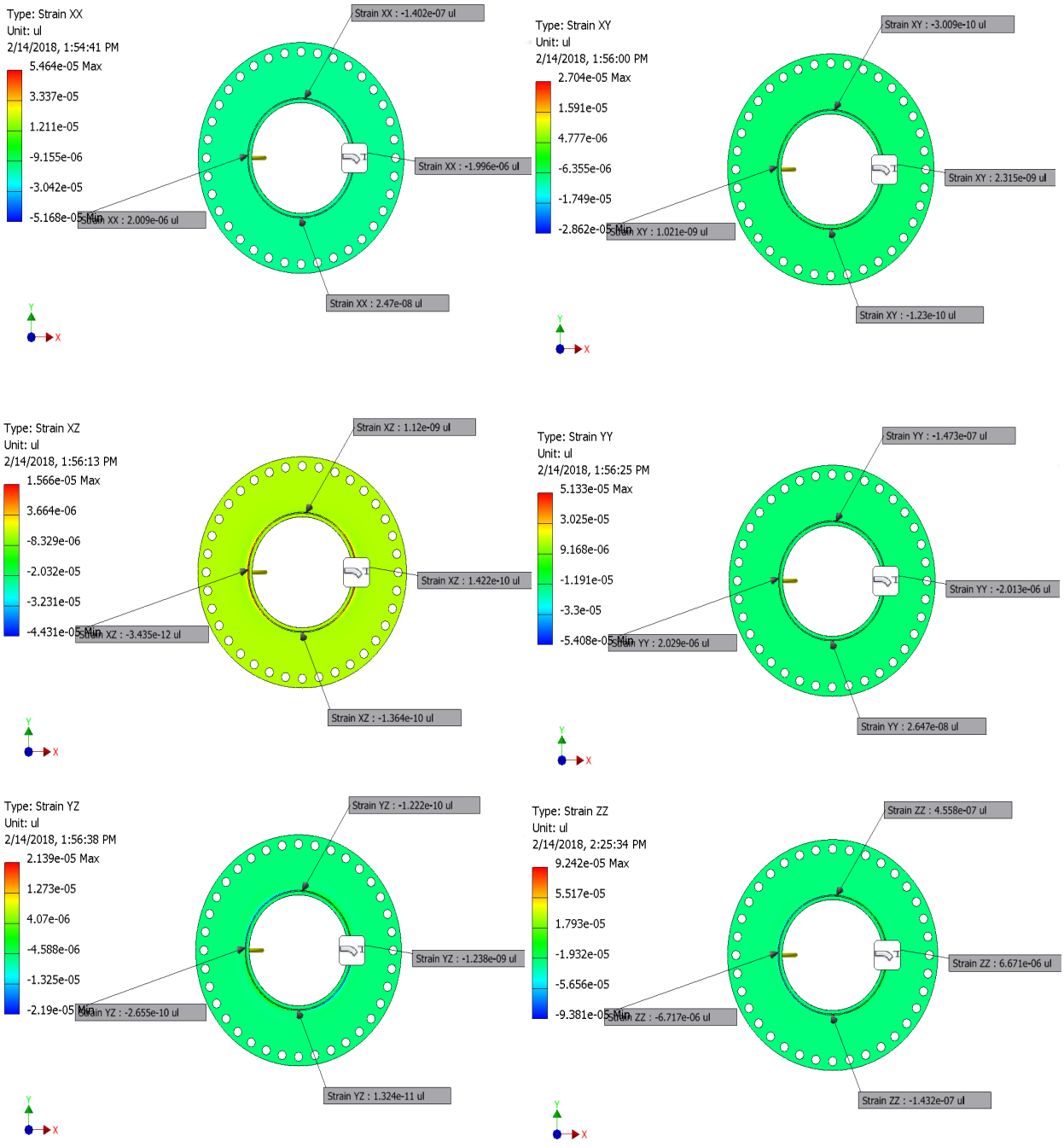

Figure 3-118. Strain contours due to the application of a moment of 1kNm about Y-Y axis ($\mathbf{M_y}$)

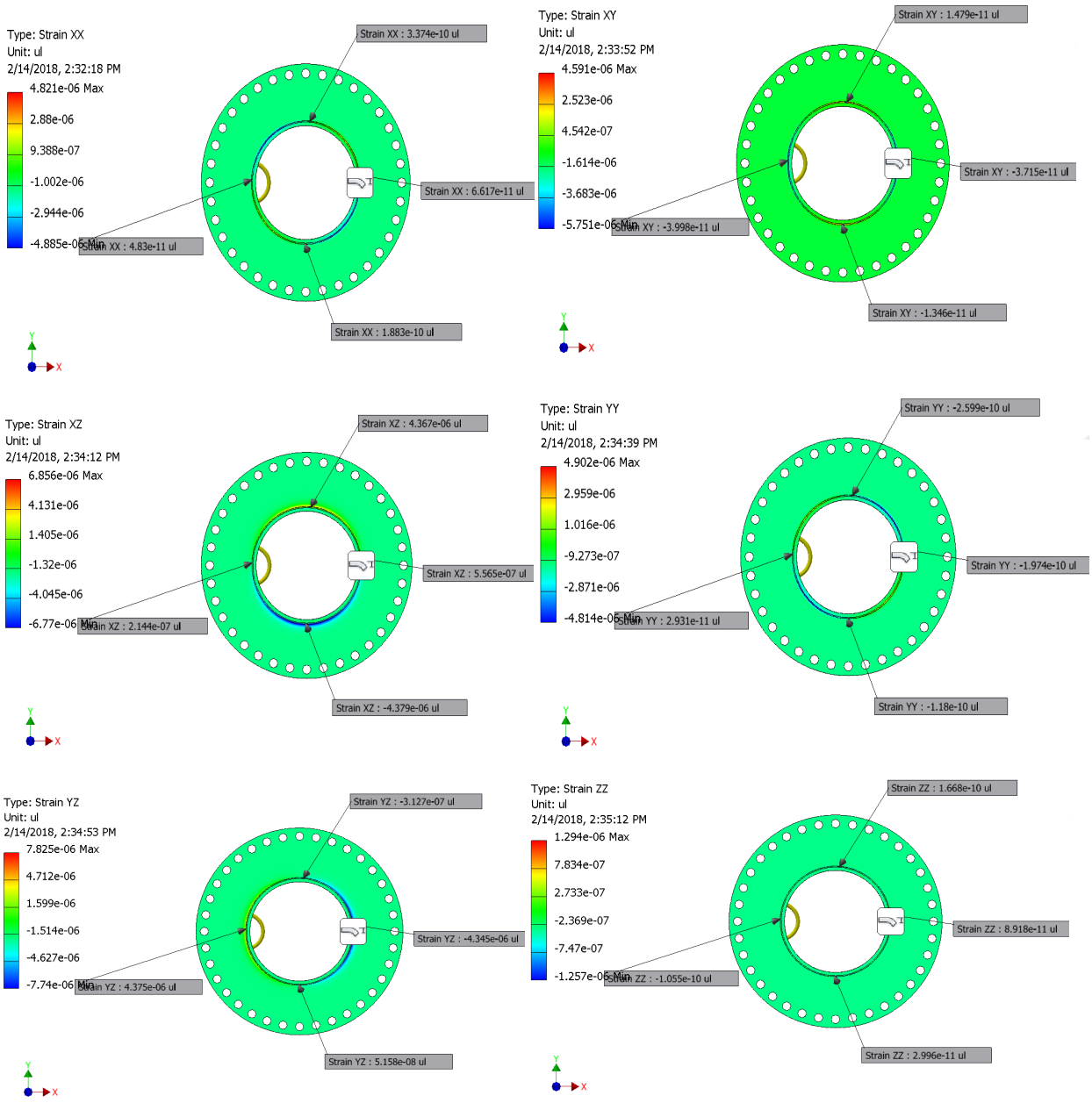

Figure 3-119. Strain contours due to the application of a moment of 1kNm about Z-Z axis ($\mathbf{M_z}$)

Stress resultants equations

The following equations are obtained from superposition of the strain values reported in the previous section. The units are as follow: Strains are expressed in Micro strains. Forces are in kN. Moments are in kNm.

$$\epsilon_{xx}^{+y} = -0.15P + 0.53S_{yy} + 2.03M_x \qquad (11)$$

$$
\begin{aligned}
\epsilon_{zz}^{+y} &= 0.51P - 1.775S_{yy} - 6.72M_x \\
\epsilon_{xz}^{+y} &= -1.28S_{xx} + 0.1S_{yy} + 4.36M_z \\
\epsilon_{zz}^{+x} &= 0.51P - 1.775S_{xx} + 6.72M_y \\
\epsilon_{yy}^{+x} &= -0.15P + 0.53S_{xx} - 2.03M_y \\
\epsilon_{zy}^{+x} &= 0.1S_{xx} - 1.28S_{yy} - 4.36M_z \\
\epsilon_{zz}^{-x} &= 0.51P + 1.775S_{xx} - 6.72M_y \\
\epsilon_{yy}^{-x} &= -0.15P - 0.53S_{xx} + 2.03M_y \\
\epsilon_{zy}^{-x} &= 0.1S_{xx} - 1.28S_{yy} + 4.36M_z
\end{aligned}
$$

or, in matrix form:

$$
\underbrace{\begin{bmatrix} \epsilon_{xx}^{+y} \\ \epsilon_{zz}^{+y} \\ \epsilon_{xz}^{+y} \\ \epsilon_{yy}^{+x} \\ \epsilon_{zz}^{+x} \\ \epsilon_{zy}^{+x} \\ \epsilon_{yy}^{-x} \\ \epsilon_{zz}^{-x} \\ \epsilon_{zy}^{-x} \end{bmatrix}}_{Strains\ in\ cartesian} = \underbrace{\begin{bmatrix} -0.150 & 0.000 & 0.530 & 2.030 & 0.000 & 0.000 \\ 0.510 & 0.000 & -1.775 & -6.720 & 0.000 & 0.000 \\ 0.000 & -1.280 & 0.100 & 0.000 & 0.000 & 4.360 \\ -0.150 & 0.530 & 0.000 & 0.000 & -2.030 & 0.000 \\ 0.510 & -1.775 & 0.000 & 0.000 & 6.720 & 0.000 \\ 0.000 & 0.100 & -1.28 & 0.000 & 0.000 & -4.360 \\ -0.150 & -0.53 & 0.000 & 0.000 & 2.030 & 0.000 \\ 0.510 & 1.775 & 0.000 & 0.000 & -6.720 & 0.000 \\ 0.000 & 0.100 & -1.28 & 0.000 & 0.000 & 4.360 \end{bmatrix}}_{A} \cdot \underbrace{\begin{bmatrix} P \\ S_{xx} \\ S_{yy} \\ M_x \\ M_y \\ M_z \end{bmatrix}}_{Resultants} \tag{12}
$$

We assume that axial forces are negligible and that every point within the torque tube is subjected to uniform normal apparent strain due to temperature changes. In this case, equation (12) is rewritten as:

$$
\underbrace{\begin{bmatrix} \epsilon_{xx}^{+y} \\ \epsilon_{zz}^{+y} \\ \epsilon_{xz}^{+y} \\ \epsilon_{yy}^{+x} \\ \epsilon_{zz}^{+x} \\ \epsilon_{zy}^{+x} \\ \epsilon_{yy}^{-x} \\ \epsilon_{zz}^{-x} \\ \epsilon_{zy}^{-x} \end{bmatrix}}_{Strains\ in\ cartesian} = \underbrace{\begin{bmatrix} 1.000 & 0.000 & 0.530 & 2.030 & 0.000 & 0.000 \\ 1.000 & 0.000 & -1.775 & -6.720 & 0.000 & 0.000 \\ 0.000 & -1.280 & 0.100 & 0.000 & 0.000 & 4.360 \\ 1.000 & 0.530 & 0.000 & 0.000 & -2.030 & 0.000 \\ 1.000 & -1.775 & 0.000 & 0.000 & 6.720 & 0.000 \\ 0.000 & 0.100 & -1.280 & 0.000 & 0.000 & -4.360 \\ 1.000 & -0.530 & 0.000 & 0.000 & 2.030 & 0.000 \\ 1.000 & 1.775 & 0.000 & 0.000 & -6.720 & 0.000 \\ 0.000 & 0.100 & -1.280 & 0.000 & 0.000 & 4.360 \end{bmatrix}}_{A} \cdot \underbrace{\begin{bmatrix} T \\ S_{yy} \\ S_{yy} \\ M_x \\ My \\ M_z \end{bmatrix}}_{\substack{Resultants \\ with\ T \\ compensation}} \tag{13}
$$

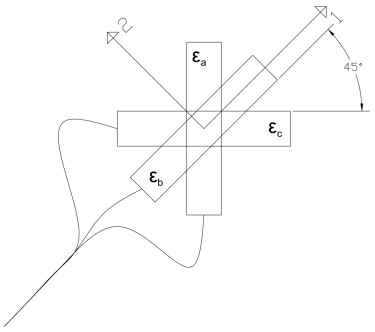

Figure 3-120. Schematics of strain sensors within a rectangular rosette

To avoid confusion, we use the sub-indices 1 and 2 in the components of the strain sensors in the following equations, to represent to the local cartesian coordinate for each rosette. From Figure 3-120, the longitudinal strain in the direction of each sensor is given by the dot product of the unit vector and the strain vector both in the direction of interest i.e.

$$\epsilon_a = n_a^T \cdot \begin{bmatrix} \epsilon_{11} & \epsilon_{12} \\ \epsilon_{21} & \epsilon_{22} \end{bmatrix} n_a \qquad \epsilon_b = n_b^T \cdot \begin{bmatrix} \epsilon_{11} & \epsilon_{12} \\ \epsilon_{21} & \epsilon_{22} \end{bmatrix} n_b \qquad \epsilon_c = n_c^T \cdot \begin{bmatrix} \epsilon_{11} & \epsilon_{12} \\ \epsilon_{21} & \epsilon_{22} \end{bmatrix} n_c \tag{14}$$

where n_a, n_b and n_c are unit vectors in the direction of the sensors. Since we aligned ϵ_b to the longitudinal axis of the collector, the unit vectors are:

$$n_c = n_{orange} = \begin{bmatrix} \sqrt{2}/2 \\ -\sqrt{2}/2 \end{bmatrix} \quad n_b = n_{red} = \begin{bmatrix} 1 \\ 0 \end{bmatrix} \quad n_a = n_{blue} = \begin{bmatrix} \sqrt{2}/2 \\ \sqrt{2}/2 \end{bmatrix} \tag{15}$$

then,

$$\begin{bmatrix} \epsilon_{orange} \\ \epsilon_{red} \\ \epsilon_{blue} \end{bmatrix} = \begin{bmatrix} \begin{bmatrix} \frac{\sqrt{2}}{2} & -\frac{\sqrt{2}}{2} \end{bmatrix} \begin{bmatrix} \epsilon_{11} & \epsilon_{12} \\ \epsilon_{21} & \epsilon_{22} \end{bmatrix} \begin{bmatrix} \frac{\sqrt{2}}{2} \\ -\frac{\sqrt{2}}{2} \end{bmatrix} \\ \begin{bmatrix} 1 & 0 \end{bmatrix} \begin{bmatrix} \epsilon_{11} & \epsilon_{12} \\ \epsilon_{21} & \epsilon_{22} \end{bmatrix} \begin{bmatrix} 1 \\ 0 \end{bmatrix} \\ \begin{bmatrix} \frac{\sqrt{2}}{2} & \frac{\sqrt{2}}{2} \end{bmatrix} \begin{bmatrix} \epsilon_{11} & \epsilon_{12} \\ \epsilon_{21} & \epsilon_{22} \end{bmatrix} \begin{bmatrix} \frac{\sqrt{2}}{2} \\ \frac{\sqrt{2}}{2} \end{bmatrix} \end{bmatrix} = \begin{bmatrix} \frac{\epsilon_{11}}{2} - \epsilon_{12} + \frac{\epsilon_{22}}{2} \\ \epsilon_{11} \\ \frac{\epsilon_{11}}{2} + \epsilon_{12} + \frac{\epsilon_{22}}{2} \end{bmatrix}$$

$$= \begin{bmatrix} 0.5 & 0.5 & -1 \\ 1 & 0 & 0 \\ 0.5 & 0.5 & 1 \end{bmatrix} \cdot \begin{bmatrix} \epsilon_{11} \\ \epsilon_{22} \\ \epsilon_{12} \end{bmatrix} \tag{16}$$

Then, the relationship between stress resultants and strain measured by each sensor in the rosette is given by:

$$\epsilon_{sensors} = Q \cdot A \cdot R \tag{17}$$

where A was defined in Equation (12) and (13), and

$$Q = \begin{bmatrix} 0.5 & 0.5 & -1 & & & & & & \\ 1 & 0 & 0 & & & & Zeros & & \\ 0.5 & 0.5 & 1 & & & & & & \\ & & & 0.5 & 0.5 & -1 & & & \\ & & & 1 & 0 & 0 & & & \\ & & & 0.5 & 0.5 & 1 & & & \\ & & & & & & 0.5 & 0.5 & -1 \\ & Zeros & & & & & 1 & 0 & 0 \\ & & & & & & 0.5 & 0.5 & 1 \end{bmatrix} \quad \text{and} \quad R = \begin{bmatrix} T \\ S_{xx} \\ S_{yy} \\ M_x \\ My \\ M_z \end{bmatrix} \tag{18}$$

Since we need six sensors to solve for all resultants, we use the first equations in Equation (13) to obtain a system of six equations and six unknowns for which we can solve for the resultants:

$$R = [Q \cdot A]^{-1}_{1,2,3,4,5,6} \cdot Sensors_{1,2,3,4,5,6} \tag{19}$$

Where,

$$Sensors_{1,2,3,4,5,6} = \begin{bmatrix} \epsilon^{+y}_{orange} \\ \epsilon^{+y}_{red} \\ \epsilon^{+y}_{blue} \\ \epsilon^{+x}_{orange} \\ \epsilon^{+x}_{red} \\ \epsilon^{+x}_{blue} \end{bmatrix}$$

Then

$$\begin{aligned} T &= 0.1151\left(\epsilon^{+y}_{orange} + \epsilon^{+x}_{blue}\right) + 0.2680\left(\epsilon^{+y}_{red} + \epsilon^{+x}_{red}\right) + 0.1169\left(\epsilon^{+y}_{blue} + \epsilon^{+x}_{orange}\right) \\ S_x &= -24.1744\left(\epsilon^{+y}_{orange} - \epsilon^{+x}_{orange}\right) - 56.3025\left(\epsilon^{+y}_{red} - \epsilon^{+x}_{red}\right) - 24.5651\left(\epsilon^{+y}_{blue} - \epsilon^{+x}_{blue}\right) \\ S_y &= -24.1744\left(\epsilon^{+y}_{blue} - \epsilon^{+x}_{blue}\right) - 56.3025\left(\epsilon^{+y}_{red} - \epsilon^{+x}_{red}\right) - 24.5651\left(\epsilon^{+y}_{orange} - \epsilon^{+x}_{orange}\right) \\ M_x &= 6.3569\epsilon^{+y}_{orange} + 15.0603\epsilon^{+y}_{red} + 6.2540\epsilon^{+y}_{blue} - 6.4711\epsilon^{+x}_{orange} - 14.8317\epsilon^{+x}_{red} - \\ &\quad 6.3682\epsilon^{+x}_{blue} \\ M_y &= -6.3682\epsilon^{+y}_{orange} - 14.8317\epsilon^{+y}_{red} - 6.4711\epsilon^{+y}_{blue} + 6.2540\epsilon^{+x}_{orange} + 15.0603\epsilon^{+x}_{red} \\ &\quad + 6.3569\epsilon^{+x}_{blue} \end{aligned} \tag{20}$$

$$M_z = Torque = -7.2118\left(\epsilon_{orange}^{+y} - \epsilon_{blue}^{+x}\right) - 16.5292\left(\epsilon_{red}^{+y} - \epsilon_{red}^{+x}\right) - 7.0971\left(\epsilon_{blue}^{+y} - \epsilon_{orange}^{+x}\right)$$

3.5.3.3 Procedure for assessing the torsional performance

For a spaceframe cantilever subjected to torsion, the following is the macroscopic behavior in terms of torque and twisting for uniformly distributed torque.

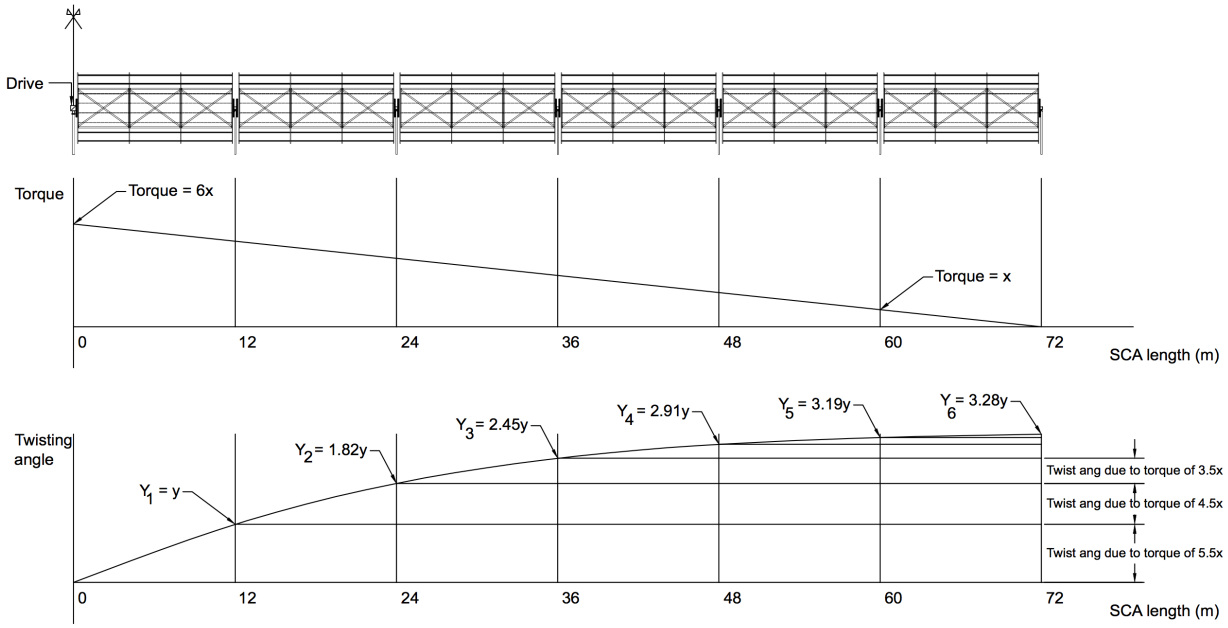

Figure 3-121. Torsional behavior of a collector array

Note that the torque graph in Figure 3-121 is simply an integration of a uniformly induced torque with zero torque at the free end. Assuming each collector will twist proportional to the torque, the resulting shape of twisting angle distribution will come from an integration of a straight line that is proportional to the torque, leading to the parabolic shape shown also in Figure 3-121. We use that information to make extrapolation for the array behavior from measurements we perform on a single collector. Note that the maximum torque in an array is 6 times larger than the maximum torque experienced by a single collector. Also, from the graph, since the twist angle is proportional to the area under torque distribution, it can be observed that the maximum twist in an array is $6 * 6 = 36$ times larger than the maximum twist experienced by a single collector.

Assessment based on torsional stiffness test

In this assessment, we subject the spaceframe to torsion to measure its stiffness. Then, with literature data about wind induced forces, we estimate the resulting deformation induced by wind. We then translate that information into optical performance.

- Wind induced forces:

To assess the performance of the array, we first obtain the torque demand. We make use of available literature data from wind tunnel tests performed by Hosoya et al [12]. We illustrate the procedure for the case of operating wind speed of 56km/hr at a height of 10m.

We find the mean speed at the height of the collector (i.e. at a height of 3 meters)

$$V_{height\ collector} = 56\left(\frac{3}{10}\right)^{\frac{1}{7}} = 46.3km/hr \ \ or\ 12.86m/s \tag{21}$$

The corresponding wind pressure is calculated as

$$q = \frac{1}{2}\rho_{air}V^2_{height\ collector} = \frac{1}{2}(1.225)(12.86)^2 = 101.29pa \tag{22}$$

We use mz coefficient of 0.12 as average value of maximum torque for operating condition. Then, the wind induced torque for one collector is

$$T_{collector} = mz * q * L * w^2 = 4.90kNm \ \ \text{(for one collector)} \tag{23}$$

As shown in Figure 3-121, the maximum torque the array will be subjected to is:

$$T_{array} = 6T_{collector} = 29.4kNm \tag{24}$$

- Torsional stiffness

To estimate how the collector performs against the wind induced torque, we measured its torsional stiffness. We did that by applying a torque at the drive end, and restraining the other end to induce twisting. We measure the torque as discussed in previous section. We measure the twisting angle as the difference of two inclinometers reading (i.e. one at each end of the collector). We rapidly applied torque to isolate the torque measurement from the apparent strain due to temperature changes. The following figures show the time history of relevant quantities few minutes before and after the application of the torque. It can be observed that strain gauges signal is clearly perturbed at the exact moment of time the torque was applied.

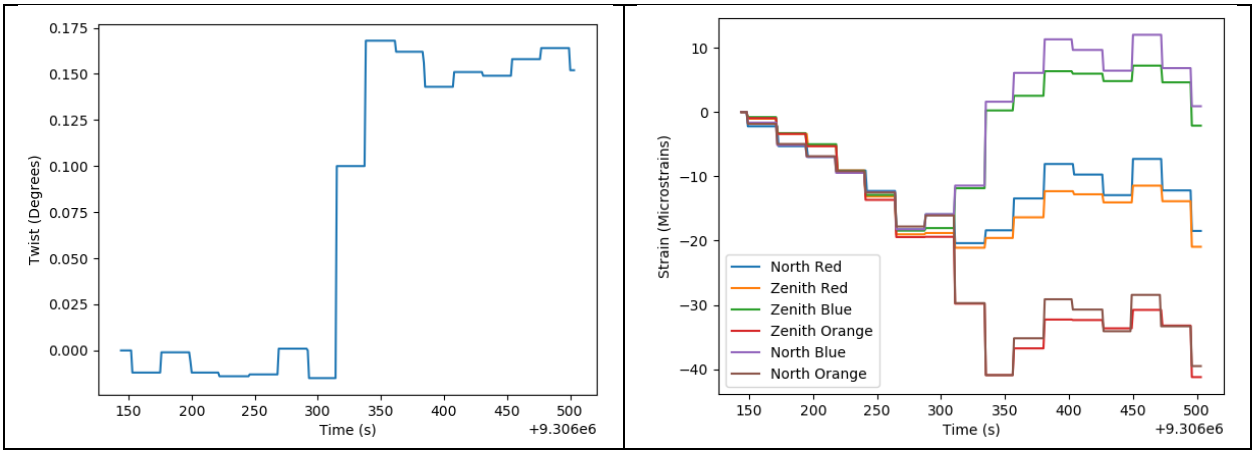

Figure 3-122. Twist time history

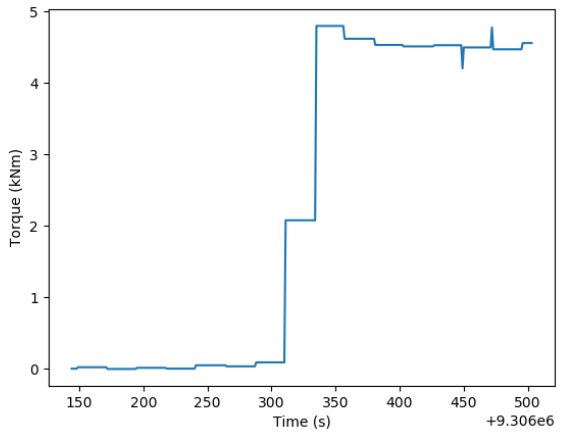

Figure 3-123. Strain Gauges time history

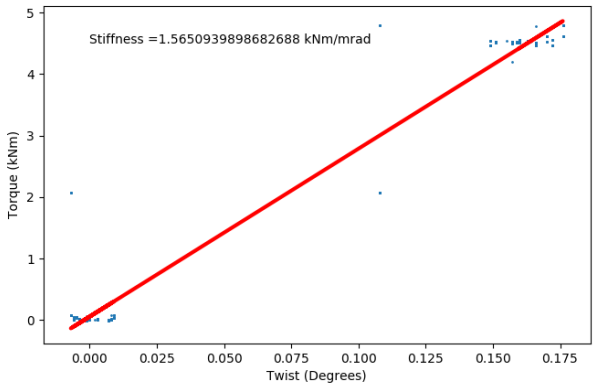

Figure 3-124. Torque time history

Figure 3-125. Torque vs Twist

It can be shown, that when collector is subjected only to torque, all sensors of same color must measure the same value (i.e. north red must measure the same value as zenith red, zenith blue must measure same value as north blue and zenith orange must measure the same value of north orange). The behavior shown in Figure 3-123 is in agreement with the specimen being twisted. The measured torsional stiffness ($K_{collector}$) is the slope of Torque vs Twist relationship as shown in Figure 3-125. Then,

$$K_{collector} = 1.565 kNm/mrad$$

The torsional stiffness of the array is estimated as the effective stiffness of a collection of six collectors in series:

$$K_{array} = \frac{1}{6/K_{collector}} = \frac{K_{collector}}{6} = 0.261 kNm/mrad \quad (25)$$

Note that the stiffness measured $K_{collector}$ is the ratio of a concentrated torque applied at each end of the collector to the rotation difference between the two ends. In the case of a collector array subjected to wind induced torque, the maximum torque calculated in Eq. (24), is distributed along the length of the array. A concentrated torque over that length will produce twice as much twisting than a uniformly distributed torque. Then, we must correct the torsional stiffness (or the maximum torque) to account for that factor, i.e.

$$K_{array}^{corrected} = 2K_{array} = 0.522 kNm/mrad \quad (26)$$

- Array twisting

With the torque demand in Eq. (24) and the corrected stiffness in (26), the expected maximum twist is

$$y_{max} = \frac{29.4kNm}{0.522kNm/mrad} = 56.32mrad \quad (27)$$

The following figure shows the behavior of the array:

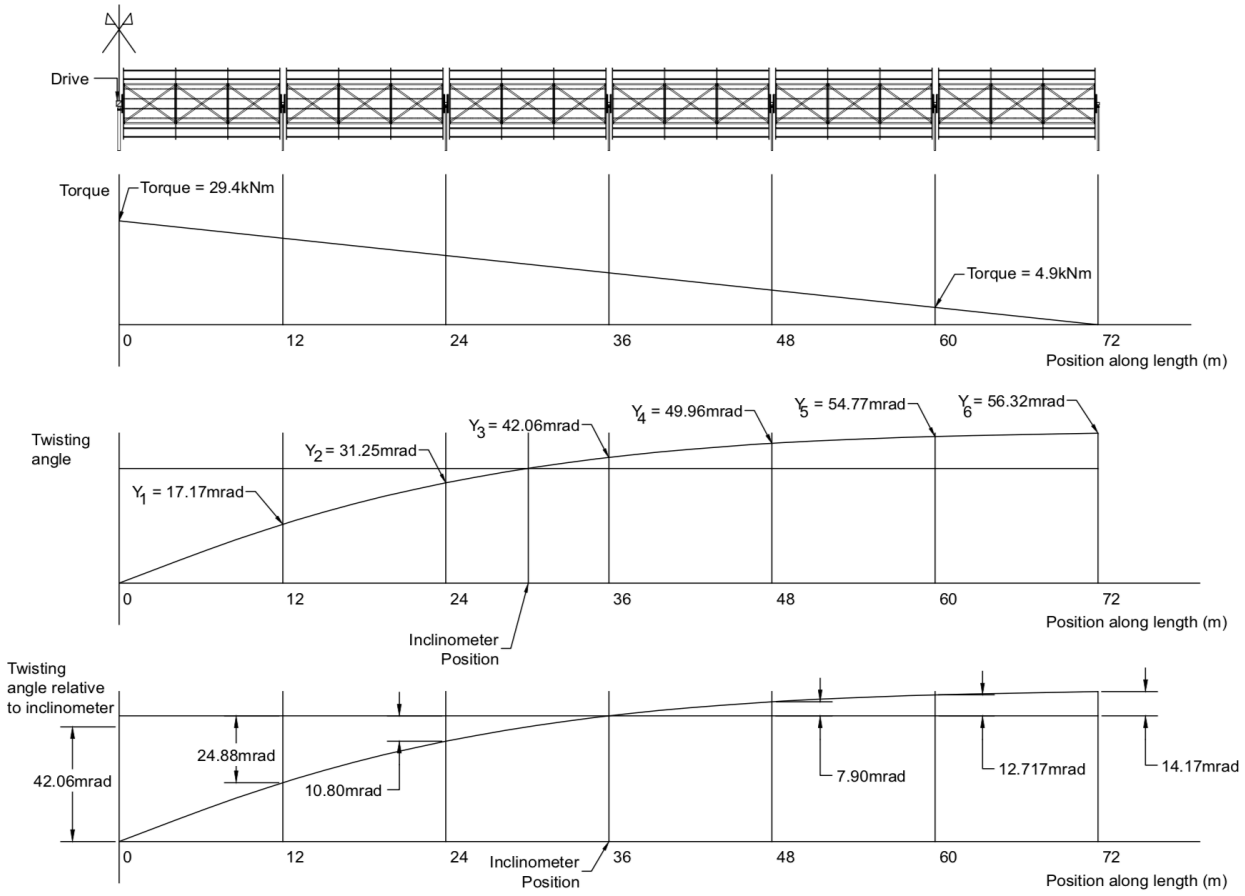

Figure 3-126. Torsional behavior of a collector array subjected to maximum torque

- Intercept factor as a function of a tracking error

Note that the control system is capable of correcting some of the errors induced by array twisting. The remaining part of the error takes the form of an equivalent tracking error. We now obtain a relationship between tracking error and intercept factor

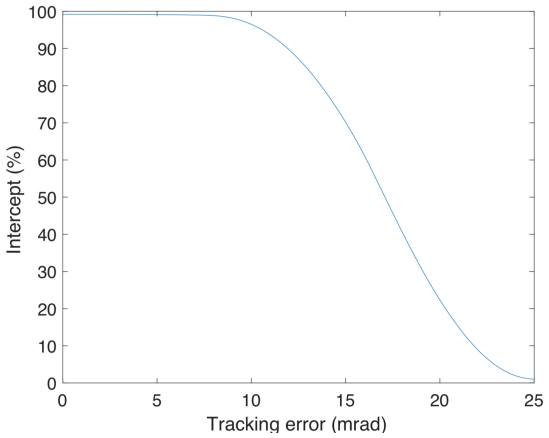

Figure 3-127. Intercept factor vs tracking error

Table 3-8. Simulated Intercept for an array in worst case wind based on measured torsional stiffness

Position along the length	Mean deviation from inclinometer	Intercept factor
0 - 12	34mrad	0
12 - 24	17mrad	60%
24 - 36	5.4mrad	99%
36 - 48	3.95mrad	99%
48 - 60	10.1mrad	97%
60 – 72	13.3mrad	90%

The overall intercept factor is 75%. The following graph shows the relationship between worst case intercept factor and wind speed for GPTC. The graph also shows the simulated results of the frame used in Cameo and Solana/Mojave projects [17].

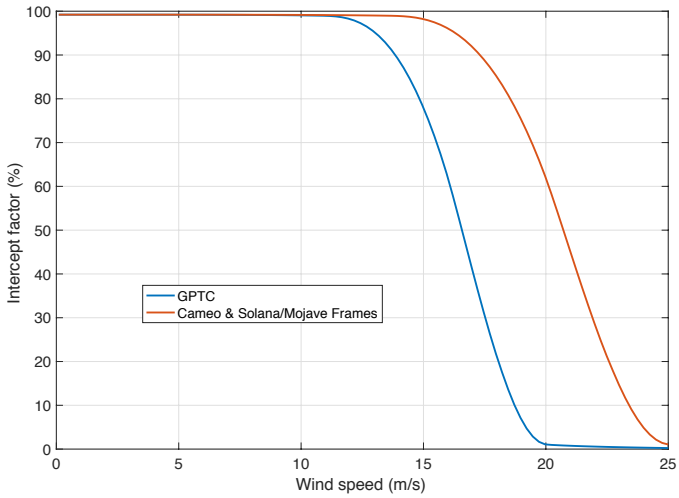

Figure 3-128. Worst case Intercept factor vs wind speed

Note that for wind speed lower than 14m/s (or 50km/hr) we expect intercept factor to be greater than 90%.

Assessment based on ambient induced twisting

The collector is being subjected to ambient wind load, including some strong wind events. The wind speed and direction, the twisting deformation and strain gauge data has been recorded for over four months. This information is now used to assess the performance of the collector. The assessment basically consists of scaling the twisting deformation with a factor that accounts for the deformation of a full array. From all days of testing, we paid closer attention to those with higher wind conditions and considered for study. The following figure shows a time history of the twist of the collector (in blue) and a time history of collector orientation (in red).

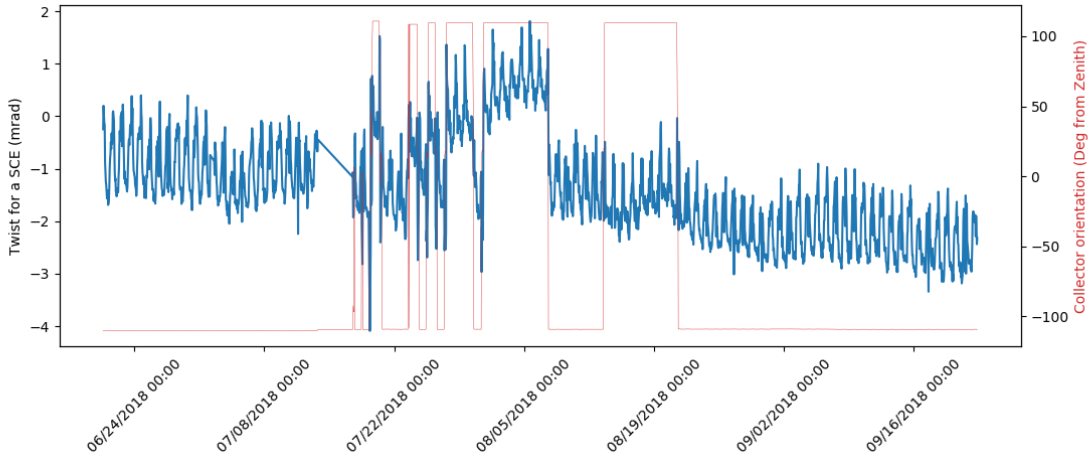

Figure 3-129. Three-month history of collector twist

It can be observed that due to an imbalance of the collector, there is a tendency of it to be twisted towards its orientation. It can also be observed that collector shows a time varying twisting. No degradation is observed for this period, as the amplitude of twisting is pretty much the same. We also show the time history of 5-mins average wind speed and wind direction over the same period.

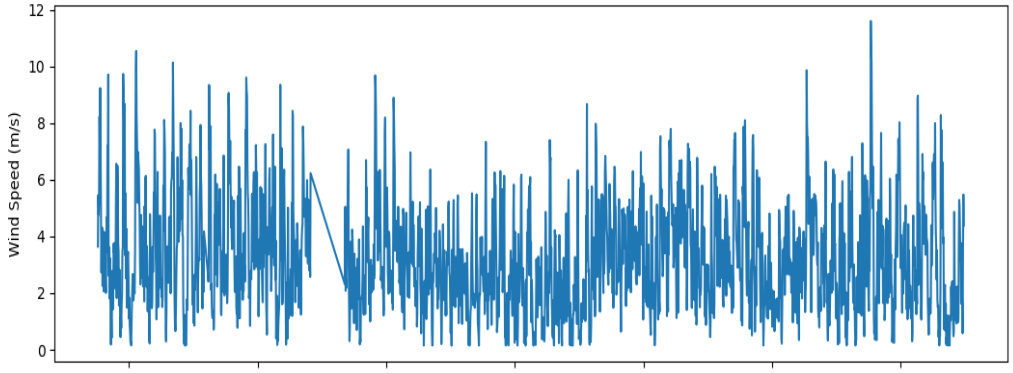

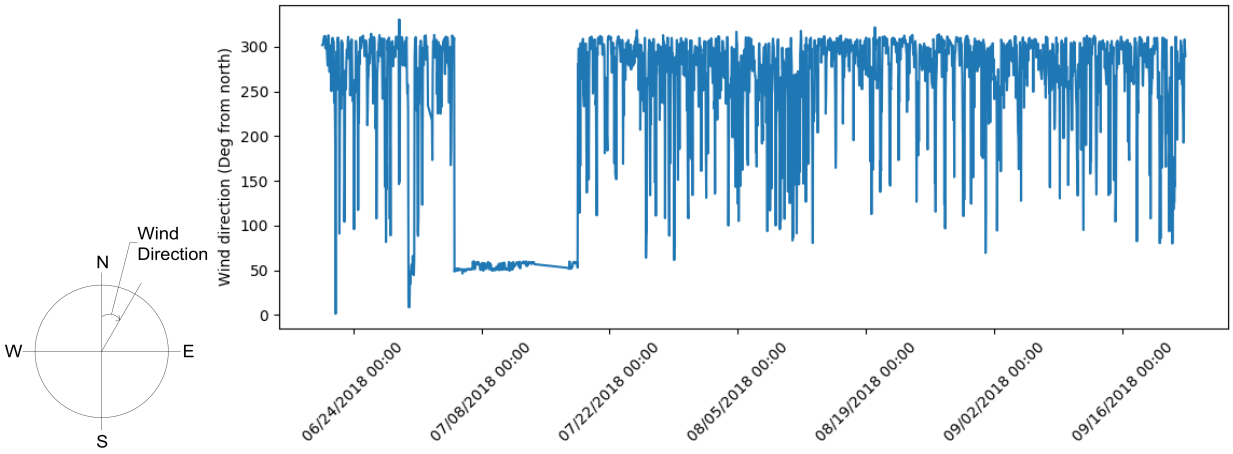

Figure 3-130. Three-month history of 5-mins mean wind speed

Note that most of the time, wind direction was about 305^{o} relative to the north (i.e. N55W). Also, collector was stowed towards the north (-109 ^{o} from zenith).

The following graphs show the time history of wind speed and wind induced twist adjusted for a SCA for one of the most critical wind scenarios (i.e. in terms of wind speed with collector pointing against wind direction).

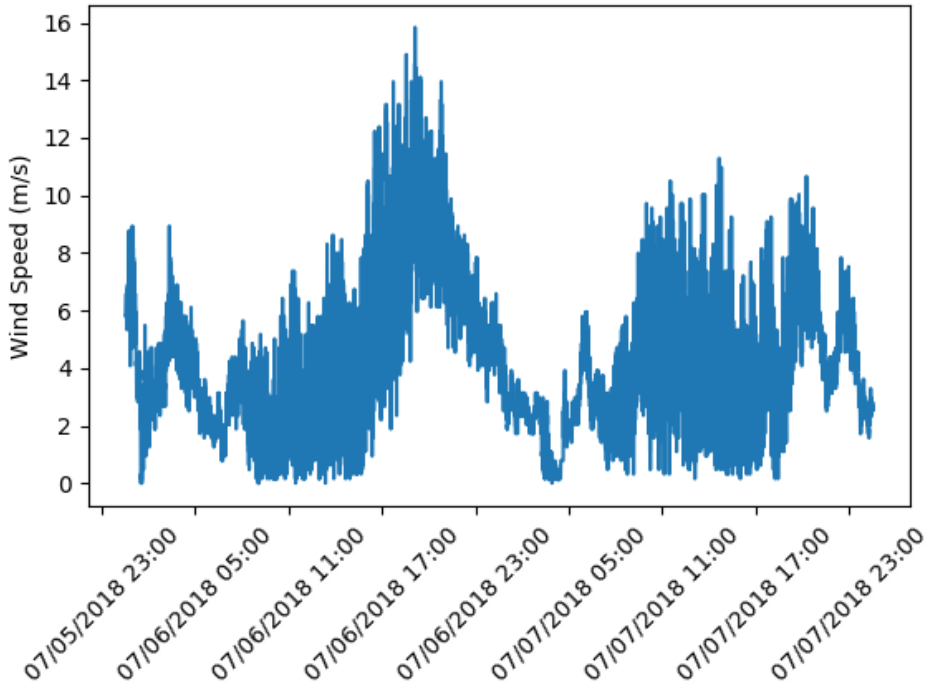

Figure 3-131. Wind speed time history

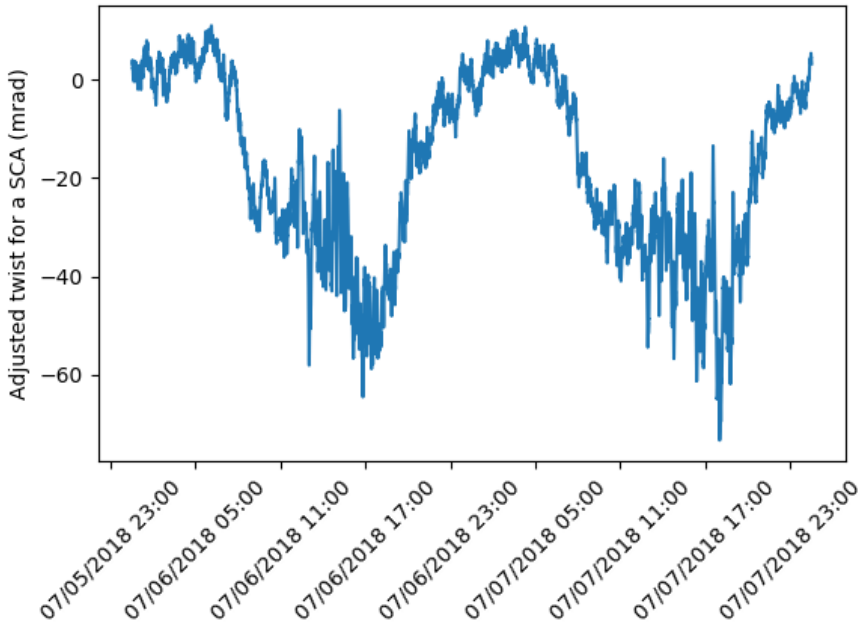

Figure 3-132. Time history of twisting adjusted for SCA. (i.e. measured scaled with a factor of 36)

We see that maximum twist is close but in general lower than what we predicted via torsional stiffness and empirical wind force demand according to Hosoya et al [12]. Also, from history of twist angle, we see that the amplitude of twist remains pretty much constant over the period suggesting that collector has not experienced a degradation that can be sensed by the inclinometers. Thus, based on this data, we conclude that collector has not experienced reduction in optical performance over the six months of testing. This is also supported by seeing no change in the target pictures. We will discuss apparent torsion creep type of behavior in Section 3.6.

3.6 STRUCTURE HEALTH, MAINTENANCE AND REPAIRS

During the testing period, we detected some insufficiencies of the design that affected performance and can also reduce the durability of the collector. This section is intended to describe the findings, identify possible causes and propose improvements for next generation design.

3.6.1 End plates insufficient out-of-plane stiffness

By inspection of the spaceframe assembly before lifting, we observed that the ends of spaceframe lacked the necessary out of plane stiffness to prevent the mode of deformation shown in the following figure

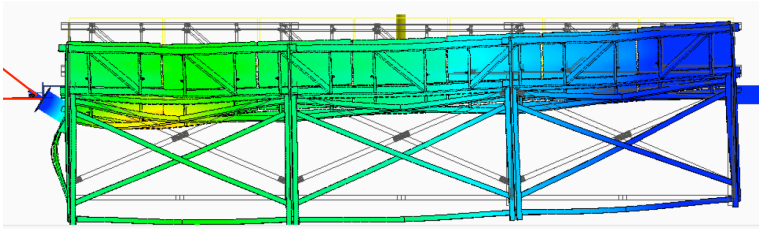

Figure 3-133. Exaggerated deformed shape showing the effect of insufficient out-of-plane stiffness of the ends of spaceframe.

Note this mode did not appear during the collector lifting. This mode of deformation shows up due to the eccentricity of the reaction point shown in Figure 3-137. This eccentricity is not part of the collector design. It was added to the prototype to adopt a stronger pylon for the torque test.

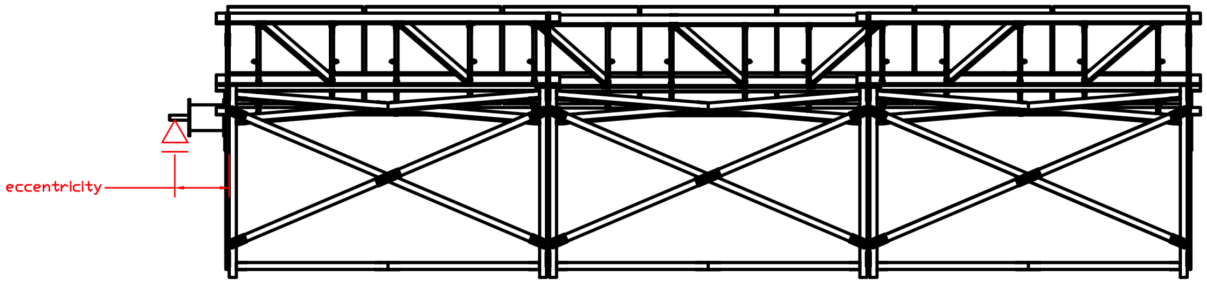

Figure 3-134. Eccentricity of bearing with respect to the spaceframe.

We stiffened the end plates by adding structural steel hollow sections (HSS4x6) as illustrated in Figure 3-135. The need for additional out-of-plane stiffness in the actual design needs investigation. A sophisticated model that account for large deformation is required. There are many strategies for increasing out-of-plane stiffness of the end-plates. Supported by our observations of original design and the stiffening solution, we will determine the best strategy for improving the performance of the end plates.

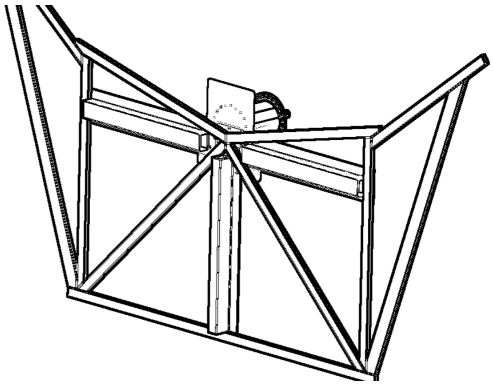

Figure 3-135. Hollow structural sections attached to end plates to provide additional out-of-plane stiffness.

3.6.2 Receiver mount deformation

Receiver mount was found to not properly enforce the position of the receiver. Receiver was observed to sag about $\pm$ 1 inch from its nominal position. We inspected the receiver mounts at the end of the collector and they were significantly stiffer than the intermediate ones. This clearly suggests that there is an insufficiency in the lower receiver mount design. Three hypotheses were considered as indicated in the following figure.

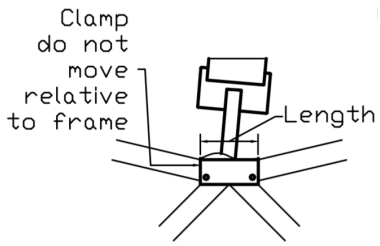	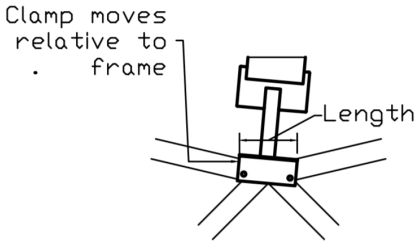	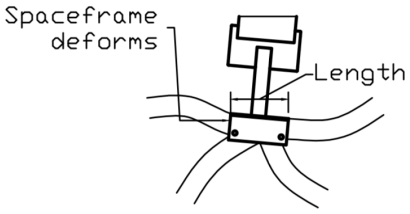
Hypothesis 1: The lower receiver mount consists of a cantilever bar built in to the top plate of a clamp. The top plate may be flexible enough to allow the cantilever arm to rotate by around 12.5 mrads (which will translate into the observed 1" displacement of the top receiver mount).	Hypothesis 2: There is an insufficiency in friction between clamp and spaceframe, and enough play within bolts holes to allow the lower receiver mount to rotate as rigid body by about 12.5 mrads. The play between bolts and holes must be around 1/16" of an inch to allow the lower receiver mount to develop the 12.5 mrad of rotation.	Hypothesis 3: Given that only 1/16" of vertical movement is needed in lower receiver mount to rotate receiver mount to produce 1" displacement, it is also possible that the frame is accommodating that deformation.

Figure 3-136. Possible candidates causing receiver to zag

A combination of the mechanisms shown in Figure 3-136 could be present. A detailed numerical model of the lower receiver mount suggested that Hypothesis 1 was a strong candidate. In an effort to solve the problem, we stiffened the top plate by welding flat plates as shown in Figure 3-137. However, stiffening the top plate of the lower receiver mount did not solve the problem. We concluded that the clamping force induced a bending deformation of the top plate that made it significantly stiffer than what the detailed model predicted, thus we show that hyphotesis 1 alone was not true. In all other cases, increasing the length of the length of the lower receiver mount (length as annotated in Figure 3-136) will increase the stiffness. In fact, the stiffness can increase proportional to up to the cube of the length of the lower receiver mount.

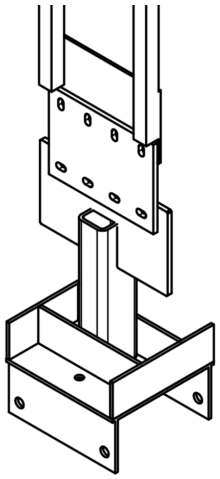

Figure 3-137. Stiffening of lower receiver mount

The impact on the optical performance was discussed in Section 3.5.2.1. This analysis serves as the basis for the design improvements. A closer attention to that problem (by the use of observed performance, validation prototypes and more involved simulation of the spaceframe-lower receiver mount interface) is needed for the next generation design of the spaceframe.

3.6.3 Insufficiency of special detail for out-of-plane load bridging between torque resisting components

The current design relied on splay resisting components (SRC) to bridge forces between adjacent torque resisting components (TRC). To improve the capacity of SRCs, some features were added to the torque resisting components that act as backbone or reinforcement for the SRC. To understand the strategy, we refer to Figure 3-38 (shown below for convenience). In most operating conditions, adjacent TRC members (annotated with numbers 17 and 3 in the figure) will be subjected to forces acting in opposite direction as indicated by the arrows (such as the one annotated with number 18 in the figure). These two forces create an anti-plane moment that need to be resisted by the SRC (annotated with number 2). By extending members such as the one annotated with number 9, we prevent significant gaps that would make the effective stiffness of the zone to be much lower. On the other hand, note that individual members within the SRC are joined by truss nail plates. This means that nail-plates would be responsible of bridging the anti-plane forces not only to maintain stiffness but the integrity of the spaceframe. We saw visible evidences of insufficiency of this strategy.

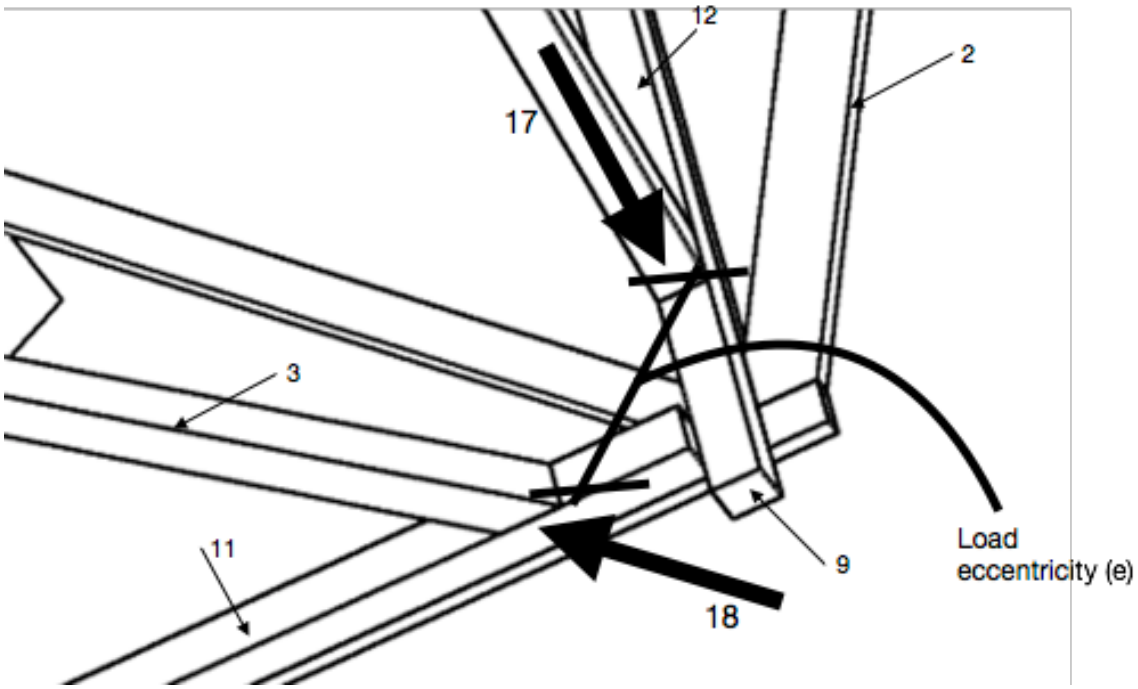

Figure 3-138. Forces acting out of the plane of SRC members (Figure 3-38)

The following figure shows evidence of lack of effectiveness of the strategy.

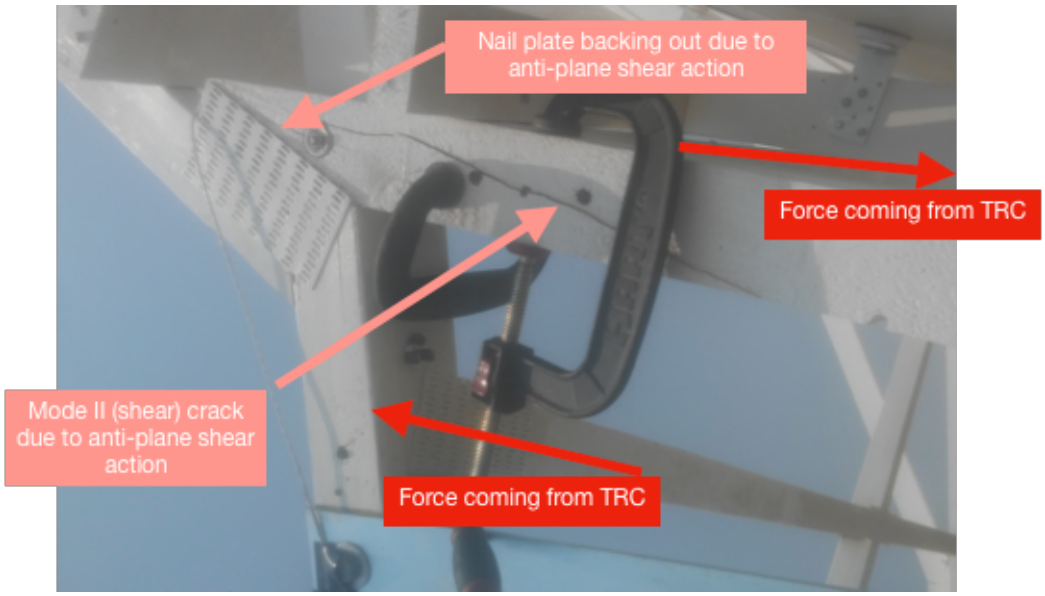

Figure 3-139. Effect of forces leading to out-of-plane failure mode

To prevent this crack from growing further, the adjacent TRC were joined together by a 7 gauge steel plate to directly bridge the loads between them. This did not affect the optical performance of the system.

Figure 3-140. Repair of damage due to insufficiency against antiplane shear forces on SRC

Next generation design will include means of interconnecting adjacents TRC to ensure integrity of the frame so that the structure does not rely on SRC at all.

3.6.4 Time evolving gap on wood to wood assembly joints

Assembly of the spaceframe was done using wood to wood lag screws and throughbolts. They were designed for stiffness and strength. However, none of the spaceframe components were designed for long duration forces. During normal operation, every member of the spaceframe will experience load reversal. However, during long days of non-operation, high stressed members and joints can experience creep. Our first prototype has been subjected to sustained loads due to its self-weight for weeks. We noticed that gaps (as shown in) of approximately ¼" have been growing with time. The following figure shows the state of the gaps as of October 5, 2018.

Figure 3-141. Gaps formed within assembly wood to wood joints

Although we have not seen an impact on the collector's performance due to the formation of these gaps, this is a problem to study and take proper considerations in the design of the next generation of the collector.

Another evidence of creep type behavior can be observed in the time history of the twisting angle of the collector (Figure 3-122). Due to imbalance of the collector (i.e. a deviation between collector's center of mass and axis of rotation), the collector has been subjected to sustained torque while at stow.

3.6.5 Comments on structure health

The spaceframe presented signs of insufficiency at a very localized level. Some of them manifested at the beginning of operation while others only revealed themselves after months of operation. It is well known [15], that in the current state of the art of design of structures, especially those made of natural materials, due to the many sources of variability and modeling uncertainties, analytical and numerical estimates of structural responses without physical testing lack the necessary accuracy for optimized design.

The reader is referred to several blind contests (such as [14]) in which response of very simple structural systems is predicted by several experts, for which components were tested. Then, the system is physically subjected to the mechanical actions considered by the experts. Results show high variability in predictions even for structures that stay within the elastic domain.

Despite the physical, time and economical constraints of physical testing, structural design still benefits from either reduced or full-scale testing, and more recently, hybrid testing (i.e. a portion of the structure is simulated numerically, while others are simulated physically).

This page intentionally left blank

4 PROJECT MILESTONES

The Project Milestones are summarized in Tables 4-1 and 4-2 for the first and second phases of the project, respectively. The techniques used to determine the measured values for each metric were presented in the Project Outcomes section of this report.

Table 4-1 First phase milestones

	Metric Definition	*Success Value*	*Measured Value*	*Assessment Tool (Quality Assurance)*	*Goal Met (Y/N)*
Milestone 1.1	Project IRR Constraints: First year heat price: $7/MMBtu	>10%	17.3%	One-tailed test at a 0.05 level of significance Z > -1.64	Y
Milestone 1.2	Computational simulation of Solar Collector Array (10-12 Solar Collector Elements [SCE]) demonstrates acceptable intercept factor under worst-case operational wind loading.	> 90%	95%	One-tailed test at a 0.05 level of significance T > -$t_{0.95}$	Y
Milestone 1.3	Annual optical efficiency simulation achieves target	> 55%	61.7	One-tailed test at a 0.05 level of significance Z > $Z_{0.95}$	Y
Milestone 1.4	Computational simulation of collector (SCE) demonstrates acceptable internal stress under worst-case survivable wind loading (137 km/hr)	Member stresses < 33.15MPa and joint forces <14.59kN	Member stresses = 2.95MPa and joint forces =10.00kN	One-tailed test at a 0.05 level of significance T < $t_{0.95}$	Y
Milestone 1.5	Slope deviation difference between model and experiment Constraints: estimated model parameters	< 1mrad	0.1mrad	One-tailed test at a 0.05 level of significance Z < 1.64	Y
Milestone 1.6	Total installed collector (TIC) cost Constraints: labor costs are estimates and are not based on having actually performed the assembly or installation	< $50/m^2	$50.3/m^2	One-tailed test at a 0.05 level of significance Z < 1.64	Y
Milestone 1.7	Computational simulation of Solar Collector Array (10-12 SCEs) demonstrates acceptable intercept factor under worst-case operational wind loading (***for aged joints***)	> 90%*	95.8%	One-tailed test at a 0.05 level of significance T > -$t_{0.95}$	Y

Table 4-2 Second phase milestones

	Metric Definition	*Success Value*	*Measured Value*	*Assessment Tool (Quality Assurance)*	*Goal Met (Y/N)*
Milestone 2.1	SCE RMS slope error $\theta_{rms,}$ Constraint: Mirrors θ_{rms}< 1.9 mrad; Elevation: 10° and 90°	< 4 mrad	4 mrad	Multiple measurements of θ_{rms} assessed by one-tailed test at a 0.05 level of significance T < $t_{0.95}$	Y
Milestone 2.2	Mean intercept factor near solar noon over one day; Constraint: C > 50 Wind speed < 4 m/s (14.4 km/hr)	> 95 %	97% (Camera method, adjusted for receiver straightness)	Use population standard deviation σ from propagation of errors and compare Z statistic with $Z_{.95}$	Y
Milestone 2.3	Mean intercept factor, Near solar noon 90 days	> 95%	97%	One-tailed test at a 0.05 level of significance T > -$t_{0.95}$	Y
Milestone 2.4	Annual maintenance cost for a 1.5%/yr decay is consistent with 10% IRR for 10 MWt plant and $5/MMBtu steam price	<$100,000	$36,000	t-test of 0.05 significance	Y
Milestone 2.5	Total installed collector cost	< $50/m2	$49.00	One-tailed test at a 0.05 level of significance Z < 1.64	Y
Milestone 2.6	Annual optical efficiency from simulation incorporating measured mean η_0 and IAM	> 55%	61.7%	One-tailed test at a 0.05 level of significance T > -t0.95	Y
Milestone 2.7	SCA intercept factor in maximum operating wind speed (56 km/hr) using a single SCE-torque transfer unit cell as surrogate	>90%	90%	One-tailed test at a 0.05 level of significance T < t0.95	Y**

This page intentionally left blank

5 CONCLUSIONS AND RECOMMENDATIONS

The built environment in the USA relies heavily on lumber framing. It is an intuitive and appealing idea to consider the use of this sustainable and aesthetically pleasing material to serve as the building blocks for the structure of solar collectors covering large areas of land. The energy industry is conservative and it must be demonstrated to the satisfaction of investors that a collector built from a natural material will provide the required service performance over the life of the plant. The technology provider must also gain confidence about the ability to meet aggressive cost goals. From our performance in this two-year project we have concluded that it is feasible to meet the market requirements with our GPTC but that design improvements, assembly and testing at the array level, and long-term energy production testing is needed to build further confidence for large scale industrial projects with a lifetime of several years. This conclusion is based on measuring the optical and structural performance of the collector over five months. The only structural defect that manifested in performance loss was due to the design of the receiver mount. Inadequate analysis had been performed for this component leading to a compromised performance. Following the observation of this design defect, analysis has led to an improved design that should be validated with a component test. The next steps for a more robust and optimized design of the collector will combine our observations and measurements for the first prototype with more sophisticated simulations of the regions where we detected the need for improvements.

This page intentionally left blank

REFERENCES

[1] DEPARTMENT OF ENERGY (DOE), EERE, CONCENTRATING SOLAR POWER: CONCENTRATING OPTICS FOR LOWER LEVELIZED ENERGY COSTS (COLLECTS) Funding Opportunity Announcement (FOA) Number: DE-FOA-0001268

[2] California's 2017 Climate Change Scoping Plan, California Air Resources Board

[3] K. Chamberlain," CSP parabolic trough report: cost, performance and key trends", 2013

[4] Hammond, G. and Jones, C. (2010). "Inventory of Carbon & Energy (ICE), Version 1.6a." Sustainable Energy Research Team (SERT), Department of Mechanical Engineering, Bath

[5] Clifford K. Ho, Siri S. Khalsa, Gregory J. Kolb, "Methods for probabilistic modeling of concentrating solar power plants," Solar Energy 85 (2011) 669–675

[6] R. Silva, M. Pérez, M. Berenguel, L. Valenzuela, E. Zarza, "Uncertainty and global sensitivity analysis in the design of parabolic-trough direct steam generation plants for process heat applications," Applied Energy 121 (2014) 233–2442

[7] Richard W. Haynes and Roger D. Fight, "Reconsidering Price Projections for Selected Grades of Douglas-Fir, Coast Hem-Fir, Inland Hem-Fir, and Ponderosa Pine Lumber," USDA Research Paper PNW-RP-561, June 2004

[8] Random Lengths data for wood FOB mill prices. http://www.randomlengths.com/

[9] Database from National Oceanic and Atmospheric Administration (NOAA)

[10] ASTM E 1049-85. (Reapproved 2005). "Standard practices for cycle counting in fatigue analysis". ASTM International.

[11] D. Buie, A. Monger, and C. Dey, "Sunshape distributions for terrestrial solar simulations", Solar Energy 74 (2003)

[12] Hosoya, N., J. A. Peterka, R. C. Gee, and D. Kearney. "Wind Tunnel Tests of Parabolic Trough Solar Collectors." (2008)

[13] Peralta, N, P Gleckman and J Raade. "Spaceframe support structure for a solar collector", US Patent App. 15/892, 105

[14] Terzic, V., Schoettler, M. J., Restrepo, J. I. and Mahin S. A. (2015). "Concrete Column Blind Prediction Contest 2010: Outcomes and Observations", PEER Report 2015/01

[15] Peralta, N. (2016) "Computational Strategies for Multi-Scale Modeling of Masonry Components and Structures", UC Berkeley dissertations

[16] P. Blanc *et al.*, “Direct normal irradiance related definitions and applications: The circumsolar issue”, Solar Energy 110 (2014) 561–577

[17] P. Marcotte, private communication.